Alma Mater Studiorum – Università di Bologna

School of Science
Department of Physics and Astronomy
Master Degree Programme in Astrophysics and Cosmology

Microwave cryogenic calibrator for Strip LSPE: design optimization and verification

Graduation Thesis

Presented by:
Francesco Potenza

Supervisor:
Chiar.mo Prof. Leonardo Testi

Co-supervisors:
Dott. Francesco Cuttaia
(INAF-OAS Bologna)

Dott. Luca Terenzi
(INAF-OAS Bologna)

Academic year 2024-2025

Graduation date III

"...we came in?"

Contents

List of Figures

List of Tables

Introduction

The detection of the *B-modes* of the CMB (Cosmic Microwave Background) polarised component is among the most difficult and also compelling tasks of modern observational cosmology. In fact, they are linked with the presence of primordial gravitational waves, that are, indeed, theoretically predicted by inflation. Therefore, their detection could be a direct proof of the validity of the inflationary cosmological model, that is currently one of the most adopted ones.

Studying the *B-modes* of CMB is the primary objective of the LSPE (*Large Scale Polarization Explorer*), which is an international experiment consisting of two instruments: the stratospheric balloon SWIPE and the ground-based telescope Strip. The two instruments are designed to provide complementary observations of the CMB and the background.

In particular, Strip is a microwave instrument, whose core is an array of 55 polarimeters that will observe the sky in two channels, respectively centred at 43 GHz and 95 GHz. Strip is conceived in order to perform observations of the galactic synchrotron emission and to study the local atmosphere, together with its variability, at the observation site (Tenerife, Izaña). In this way it would be possible to remove foregrounds emission and, thus, obtain the resulting clearer signal of the polarised CMB (that is observed by SWIPE).

The Strip instrument is currently undergoing the verification campaign, taking place at the INAF-OAS Cryowaves Laboratory, nevertheless, some subsystems (as the telescope) and infrastructural facilities (the site) are still uder development. The aim of this phase is to characterise the instrument and optimise its performances. In particular, the estimation of the noise properties (expressed in terms of the noise temperature of the system, T_{noise}) is of paramount importance.

In order to characterise the noise of the instrument it is necessary to have a reference signal that is representative of the celestial one, namely with black-body characteristics in the microwave spectrum. For this purpose, in the specific case of Strip's calibration, it has been chosen to use a passive calibrator cooled down to cryogenic temperatures. Thus, a cryostat, to enclose the calibrating units and enabling their cooling down, has been properly designed and built.

In this dissertation, the steps of the verification campaign in which I participated

are presented. I took part to several laboratory activities at the INAF-OAS Cryowaves Laboratory, mainly concerning the assembly and characterisation of the calibrator cryostat, at first stand-alone and then integrated with Strip. In particular, in the stand-alone condition, the characterization proceeded through several *dry runs* in which the calibrator was tested at successive integration levels. These required subsequent cooldowns and warm-ups, as well as the characterization of thermometers, since an accurate knowledge of the temperature of the emissive elements is of crucial importance. Only afterwards, the characterization of the calibrator cryostat was carried out with some of the elements that will form the black body in the integrated MWs, and with the integration with Strip. All of this made it possible to characterize the calibrator while at the same time validating and refining the thermal model.

To do this, I wrote programs aimed at extracting, plotting and analysing temperatures, using Python as the programming language.

The results of these *dry runs*, in terms of minimum temperatures reached and characteristic quantities such as linear and radiative conductances, have been compared to expectations (that had been derived from preliminary thermal models of the cryostat system, that I also developed). In this way it has been possible to enhance the characterisation of the instrument from a thermal point of view.

Part of my work on thermal modelling also consisted in the development of a thermal model of the IR (Infrared) filter, that has been mounted in the calibrator cryostat, and in its verification through a dedicated *dry run*, which allowed to study the correlation between the predicted results and the experimental ones; in such a way, we could evaluate the actual impact of the filter on the internal temperature distribution of the calibrator cryostat's subsystems.

Once implemented the calibrating units in the calibrator cryostat stand-alone, the minimum temperatures reached were tested by a *dry run* performed in different environmental conditions: when looking the laboratory temperature through a vacuum window, and when instead closed by a metal vacuum flange.

Then, the calibrator cryostat was integrated with Strip, to characterise it and its subsystems from a thermal point of view, understanding how the two systems behave when coupled and both cooled down to cryogenic temperatures.

A representative subset of Strip's polarimeters was activated to have a preliminary assessment of the RF compatibility between Strip and the calibrator and to get important indications about the test procedures and data analysis methods, together with improvements in the calibrator architecture and in the test setup. The system noise temperature of the selected polarimeters was measured for the first time advantaging of the integrated system; this preliminary measure, even though performed in conditions far from the nominal setup, indicates that the calibrator, upon implementation of the planned changes, will be able to meet the specified needs.

Chapter 1

CMB, its anisotropies and polarization

1.1 The ΛCDM model

In order to describe the Universe and the physical laws upon which it relies, it is necessary to begin with a theory for gravity, being it the most influent force at large scales. The strongest candidate is the *General Theory of Relativity* [28], formulated by Albert Einstein in 1915. It is mainly based on the relationship that holds between the distribution of matter and the metric (that is a description of the geometry of the space-time). In particular, in this theory the space-time is not necessarily flat, rather, it may well be curved, depending on the mass distribution. Thus, gravity is considered as a manifestation of the curvature of the space-time following the mass distribution. The interval between two events is

$$ds^2 = g_{ij}\, dx^i dx^j \tag{1.1}$$

with g_{ij} metric tensor, in order to take into account the geometry of the space-time. In the context of General Relativity, conservation of energy, mass and momentum laws need to be found (as done for Special Relativity and Newtonian Physics), but in fully covariant form, so as

$$T^k_{\ i;k} = 0 \tag{1.2}$$

being $T^k_{\ i;k}$ the covariant derivative of the energy-momentum tensor T_{ik}. In order to express the aforementioned relationship, Einstein proposed the field equation

$$G_{ik} \equiv R_{ik} - \frac{1}{2} g_{ik} R - \Lambda g_{ik} = \frac{8\pi G}{c^4} T_{ik} \tag{1.3}$$

with G_{ik} the Einstein tensor, so the simplest combination of the Ricci tensor R_{ik} and the Ricci scalar R (both needed to describe the curvature of the space-time) having zero covariant derivative, to be in agreement with the conservation law. The term showing the cosmological constant Λ was a subsequent modification to the original field equations.

The *Cosmological Principle* [5] (the Universe is assumed to be homogeneous and isotropic on sufficiently large scales, so its properties are the same in all locations, homogeneity, and in all directions, isotropy, when averaged over cosmological distances) had been proposed by Einstein and subsequent relativistic cosmologists without any observational justification. Then, quite good observational evidence that the Universe does have these properties has been found in the CMB isotropy (coupled with the assumption of the Copernican Principle). It can be demonstrated that, so as to have the *Cosmological Principle* obeyed, the most general space–time metric must be of the form

$$ds^2 = c^2dt^2 - a(t)^2\left[\frac{dr^2}{1-Kr^2} + r^2\left(d\vartheta^2 + \sin^2\vartheta\, d\varphi^2\right)\right] \tag{1.4}$$

called the Robertson-Walker metric, with the expansion (or scale) factor a and the curvature parameter K (assuming values -1, 0, +1 corresponding respectively to the space of constant negative curvature, the Euclidean space or the hypersphere). The solutions of the Einstein equations, assuming a Robertson-Walker metric, are the Friedmann cosmological equations

$$\ddot{a} = -\frac{4\pi G}{3}\left(\varrho + \frac{3p}{c^2}\right)a + \frac{\Lambda c^2}{3}a; \quad \left(\frac{\dot{a}}{a}\right)^2 + \frac{Kc^2}{a^2} = \frac{8\pi G}{3}\varrho + \frac{\Lambda c^2}{3} \tag{1.5}$$

By using the relation

$$\varrho\, a^{3(1+w)} = \text{const.} \tag{1.6}$$

with w a constant parameter and ϱ the density of the fluid, the second equation of 1.5 can be written as

$$\left(\frac{\dot{a}}{a_0}\right)^2 = H_0^2\left[\Omega_{0m}\left(\frac{a}{a_0}\right) + \Omega_{0r}\left(\frac{a}{a_0}\right)^2 + \Omega_{0\Lambda}\left(\frac{a}{a_0}\right)^{-2} + 1 - \Omega_{0m} - \Omega_{0r} - \Omega_{0\Lambda}\right] \tag{1.7}$$

in the case of a multi-component Universe, with matter, radiation and a cosmological constant (having a crucial role in the acceleration of the expansion rate of the Universe). The density parameters Ω_{0w} computed at $t = t_0$ are defined in the common way as $\Omega_{0w} = \frac{\varrho_{0w}}{\varrho_{0c}}$, with w assuming values equal to 0, $\frac{1}{3}$ or -1 respectively for matter, radiation or cosmological constant-dominated Universe. $H_0 = \frac{\dot{a}_0}{a_0}$ is the value of the Hubble parameter evaluated for the present-day Universe ($H_0 \approx 70\ \text{km}\cdot\text{s}^{-1}\cdot\text{Mpc}^{-1}$ [13]). The model currently chosen in order to explain most of the features observed in our Universe is the ΛCDM, that predicts a flat Universe ($\Omega_{tot} \approx 1$) and its dominant components are

- **Dark Energy**: $\Omega_{0\Lambda} \approx 0.7$
- **Matter** (baryonic and Cold Dark Matter): $\Omega_{0m} \approx 0.3$

1.2 Recombination and Decoupling

The *Standard Hot Big Bang model* (homogeneous, isotropic universe whose evolution is described by the Friedmann equations, with matter and radiation fluids as principal components) predicts that at very high redshift z (so very high temperature T) matter and radiation were held in thermal equilibrium. This was made possible by frequent Thomson scatterings between free electrons and photons $\gamma(p) + e^-(q) \rightarrow \gamma(p') + e^-(q')$, maintaining matter ionised. The Universe was a hot and dense opaque plasma (*Primeval Fireball* [19]). By considering the Saha equation (valid as long as thermal equilibrium holds), it is possible to study the process of *recombination*: protons and electrons combined to form neutral hydrogen atoms, significantly reducing the free electron density (marking the ending of the *plasma epoch*, to let *neutral matter era* begins). In fact, due to the expansion of the Universe, the T of the radiation became too low to let the photons ionise matter. By defining the ionisation fraction [5]

$$x = \frac{n_e}{n_p + n_H} \approx \frac{n_e}{n_{\text{tot}}} \tag{1.8}$$

and by imposing $n_e = n_p$, to have global neutrality, it is possible, from the Saha relation for the hydrogen recombination, to study the behaviour of x as a function of redshift z and temperature of radiation T

$$\frac{x^2}{1-x} = \frac{1}{n_{\text{tot}}} \left(\frac{m_e k_B T}{2\pi\hbar^2} \right)^{3/2} \exp\left(-\frac{B_H}{k_B T} \right) \tag{1.9}$$

It is important to underline that the previous equation can be obtained from the Boltzmann statistics applied to the plasma to get the number densities n_i of the species i (given that at $T \approx 10^4 K$ all the particles are non-relativistic); the neutral hydrogen binding energy appears in the relation as $B_H \approx 13.6\, eV$. The ionisation fraction reduces to 0.5 (almost half of matter is in form of neutral atoms) at $z_{rec} \approx 1000$ ($T_{rec} \approx 4000K$), which is usually considered the beginning of the recombination process.

The process called *decoupling* happened when the expansion of the Universe started to dominate over the collisions, at a time $t = t_d$ (at $z \approx 1100$). Before decoupling, scatterings between matter and radiation were effective in the maintenance of the equilibrium between the two components. After t_d, matter and radiation started to evolve separately from a thermal point of view. In fact, the comparison between the characteristic timescales of collision and of expansion (τ_c and τ_H respectively)

$$\tau_c \propto \varrho_m^{-1} \propto (1+z)^{-3}; \quad \tau_H = \left(\frac{\dot{a}}{a} \right)^{-1} \propto (1+z)^{-3/2} \tag{1.10}$$

tells that τ_c scales more rapidly with z than τ_H (both for matter or radiation-dominated Universe)[1]. The result is that photons stopped to interact significantly with matter and they started to propagate freely from the so called *Last Scattering Surface*. This radiation formed the *Cosmic Microwave Background* (CMB).

[1] To get the previous relations, $a \propto (1+z)^{-1}$, 1.5 with $w = 0, \frac{1}{3}$ and $\frac{\dot{a}}{a} = H_0 (1+z)^{\frac{3(1+w)}{2}}$ are used.

1.3 The Cosmic Microwave Background

At decoupling, each point of the Universe on the Last Scattering Surface acted as a photon emitter. The Last Scattering Surface is modelled as a sphere centred on Earth and of radius

$$c\,(t_{now} - t_{dec}) \tag{1.11}$$

with photons travelling towards us. Given the fact that radiation was held in thermal equilibrium before t_d and afterwards photons propagated freely, CMB intensity[2] is described by the black-body spectrum:

$$I(t_i, \nu) = \frac{4\pi\hbar\nu^3}{c^2}\left[\exp\left(\frac{h\nu}{k_B T_i}\right) - 1\right]^{-1} \tag{1.12}$$

It can easily be shown that the temperature evolution of such radiation is

$$T = T_i\,\frac{a(t_i)}{a(t)} \tag{1.13}$$

In fact, by considering an adiabatic expansion of the Universe, after all processes creating or absorbing photons have become negligible, the number of photons per unit frequency ν and volume V must be conserved. N_ν is described as follows [5]

$$N_\nu = \left[\exp\left(\frac{h\nu}{k_B T}\right) - 1\right]^{-1} \tag{1.14}$$

Due to the fact that the Universe is expanding $\nu \propto a(t)^{-1}$, so, in order to keep N_ν constant as expected, $T \propto a(t)^{-1}$ is needed. The CMB temperature is now known to be 2.726±0.005 K.

In 1965, the CMB was serendipitously discovered by radio engineers Penzias and Wilson during the characterization of the atmospheric noise for the Telstar communication satellite project [20]. That thermal radiation background was then interpreted by Dicke and Peebles as the relic radiation from a primordial phase of the Universe, predicted by Gamow in the 1940s [2]. Subsequent experiments confirmed the presence of a microwave thermal background that almost perfectly fitted a perfect black-body curve, that constitutes one of the main proofs of the Hot Big Bag cosmological model. Particularly important is to acknowledge the contribution of the COBE satellite, that aimed at the measurement of the CMB spectrum. Its main advantage was that, being a satellite, the contamination of atmospheric absorption has been avoided. The CMB spectrum detected by the FIRAS instrument onboard the COBE satellite revealed how close to a perfect black-body the CMB is.

[2]Defined as power received per unit frequency per unit area per steradian.

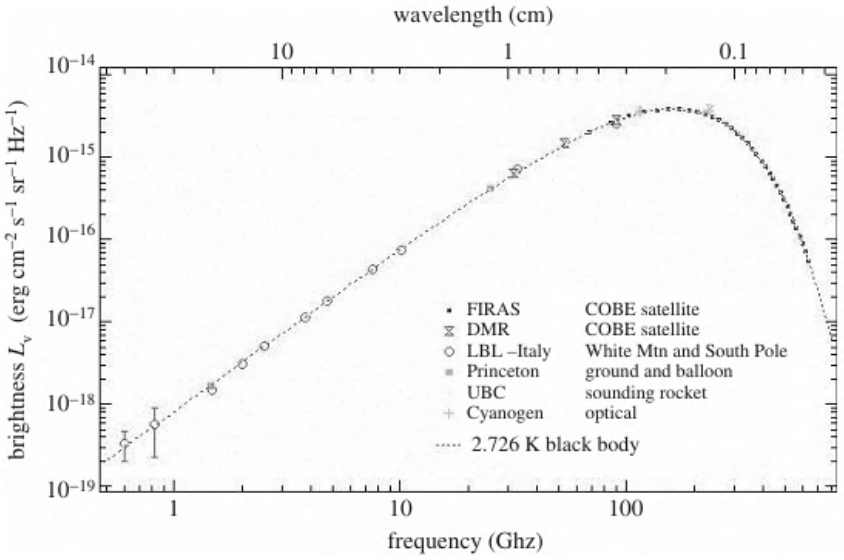

Figure 1.1: Measurements from FIRAS instrument of COBE satellite together with other instruments. The superposed dotted line is a best-fitting black-body spectrum at $T = 2.726 \pm 0.010K$ [5].

1.4 The CMB Anisotropies

In 1992 the COBE team, led by George Smoot, discovered the existence of fluctuations in the temperature distribution of the Cosmic Microwave Background [26]. This detection was of crucial importance, given the fact that such temperature fluctuations have been considered as due to density fluctuations at t_{rec}. This enables us to have unmediated access to the primordial power spectrum of density fluctuations (without the contamination of the subsequent non-linear evolution).

Two kinds of anisotropies can be described: anisotropies in total intensity (so in temperature distribution) and in the linearly polarized component (polarization anisotropies).

At first, let's provide a description of the T fluctuations of the Cosmic Microwave Background (that are of the order of 10^{-5} so approximately 30 μK)

$$\frac{\Delta T}{T}(\theta, \phi) = \frac{T(\theta, \phi) - T_0}{T_0} \tag{1.15}$$

with θ and ϕ being the usual angles of the spherical coordinates, individuating a specific direction in the plane of the sky, and T_0 is the mean temperature. A statistical treatment of the T fluctuation is usually provided in the following form

$$\frac{\Delta T(\theta, \phi)}{T} = \sum_{\ell=0}^{\infty} \sum_{m=-\ell}^{+\ell} a_{\ell m}\, Y_{\ell m}(\theta, \phi) \tag{1.16}$$

ℓ is the multipole index[3] that describes the scales of the fluctuations considered ($\vartheta \approx \frac{60^\circ}{\ell}$) and m is the azimuthal angular momentum.The terms $Y_{\ell m}$ are the orthonormal base of *Laplace spherical armonics* [27]

$$Y_{\ell m} = N_{\ell m}\, e^{im\phi}\, P_{\ell m}(\cos\vartheta) \tag{1.17}$$

with $N_{\ell m}$ a normalization constant and $P_{\ell m}$ is the associated *Legendre polynomial*. The $a_{\ell m}$ are complex coefficients serving as weights in the sum for each spherical armonic. They must satisfy the relation

$$\langle a^*_{\ell' m'}, a_{\ell m}\rangle = C_\ell\, \delta_{\ell\ell'}\, \delta_{mm'} \tag{1.18}$$

where the angular brackets stand for the average on every point of observation of the CMB and time, δ_{ij} is the Kronecker delta and C_ℓ is the angular power spectrum, defined as follows

$$C_\ell \equiv \frac{1}{2\ell+1} \sum_{m=-\ell}^{\ell} \langle a^*_{\ell m}, a_{\ell m}\rangle \tag{1.19}$$

The distribution followed by the a_{lm} coefficients can be statistically described by cosmological models. The variance (so the T fluctuations power spectrum C_ℓ for different ℓ) is studied, given the fact that, by definition for gaussian fluctuation distribution, $\langle \frac{\Delta T(\theta,\phi)}{T}\rangle = 0$, thus

$$\langle a_{\ell m}\rangle = 0 \;\forall\, m \in [-\ell, \ell] \tag{1.20}$$

In particular, the $\ell = 0$ term represents the monopole term, that modifies the average T of a specific observer's sky with respect to the global average.

The $\ell = 1$ term (so large angular scales) is the dipole correction, linked to the motion of the Milky Way with respect to a cosmologically comoving frame in which the CMB is isotropic. The angle ϑ is the angle between the line of sight and the direction of motion of the observer. The effects that have to be considered are: the *Doppler effect* due to the movement of the observer, the fact that the observer will inevitably collect more photons in that direction than an observer at rest and the aberration (the solid angle reduces for a moving observer, so the flux increases). The final T seen by the moving observer is

$$T(\theta) = T_0 \sqrt{1-\beta^2}\,(1 + \beta\cos\theta) \tag{1.21}$$

where also relativistic effects have been taken into account (described by the β term).

At large angular scales ($\ell \geq 2$) it is also possible to study the intrinsic sources of anisotropies of the CMB temperature, produced by effects either at t_{rec} or between t_{rec} and t_0. The main effect that needs to be considered is the *Sachs-Wolfe effect*. It consists

[3] $\ell = 0$ is the monopole term, linked with the average T, $\ell = 1$ describes the monopole, $\ell = 2$ is the quadrupole and so forth.

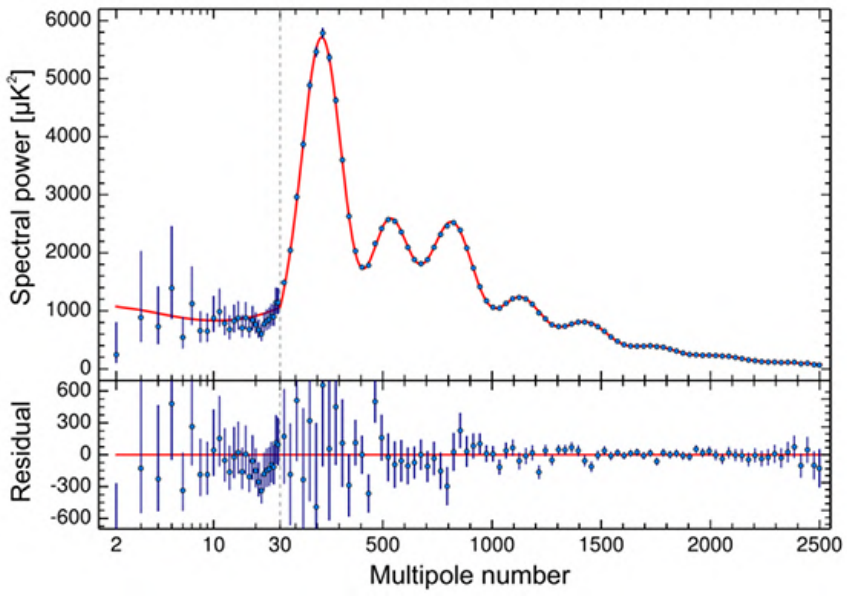

Figure 1.2: *Upper panel*: Planck 2015 satellite measurements of CMB power spectrum (blue dots) superposed to the ΛCDM best fit model (red curve). *Lower panel*: Shows the residuals with respect to the best fit [22].

in a relativistic effect due to the shift in frequency of photons encountering metric perturbations while travelling towards an observer from the Last Scattering Surface. Metric perturbations may be seen as fluctuations in the gravitational potential $\delta\phi$, due to density fluctuations $\delta\varrho$. The impact on the T variation is

$$\frac{\Delta T}{T} = \frac{1}{3}\frac{\delta\phi}{c^2} \tag{1.22}$$

Actually, the *Rees-Sciama effect* should also be taken into account (describing how the depth of a potential well changes when a photon passes through it), so

$$\frac{\Delta T}{T} = 2\int \frac{\dot{\delta\phi}}{c^2}\, dt \tag{1.23}$$

Gravitational waves (tensorial perturbations predicted by inflationary models) are also capable of generating perturbations in the metric (this time not due to density fluctuations) and, consequently, a redshifting of the photons.

1.5 The CMB Polarization

Furthermore, crucial information about the very early Universe, and in particular about inflation, may well be provided by the study of the linearly polarized component

of the Cosmic Microwave Background ([3]), which is expected to be the 10% of the total. A linear polarization of the radiation after Thomson scatterings is expected when the incoming radiation field showed a quadrupolar anisotropy, as shown in Fig. 1.3

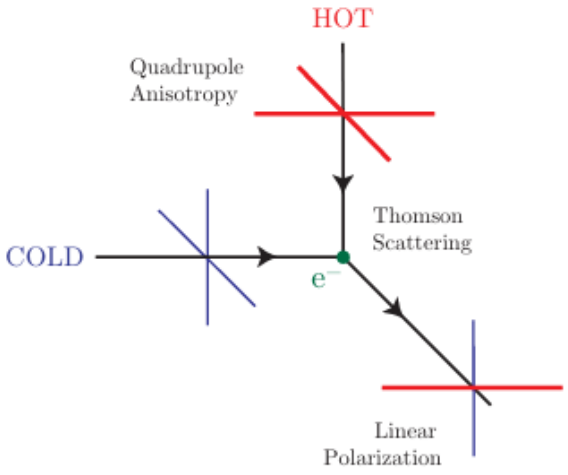

Figure 1.3: Schematic representation of how a radiation field presenting a quadrupolar anisotropy produces a linearly polarized radiation after Thomson scattering with an electron [3].

It is important to investigate how this quadrupolar anisotropy is produced, in fact there are two ways to induce it: density fluctuations in the primordial plasma (scalar fluctuations) or primordial gravitational waves (tensorial fluctuations) at decoupling. Polarization anisotropies are more difficult to be described with respect to temperature anisotropies, due to the fact that the former ones are not a scalar field. In order to proceed, the dimensionless intensity tensor must be introduced (it is usually normalised with respect to the mean intensity [29])

$$I_{ij}(\hat{n}) = \frac{\delta I}{I_0} \tag{1.24}$$

It is a 2×2 tensor whose components are defined with respect to two orthogonal axis (that can be denoted as $\hat{e}_1$ and $\hat{e}_2$, both orthogonal to the line of sight, along $\hat{n}$). The temperature anisotropy (discussed in the previous paragraph) is

$$T = \frac{1}{4}(I_{11} + I_{22}) \tag{1.25}$$

As previously said, given the fact that it is invariant under a rotation around $\hat{n}$, thus, it can be expanded in terms of the usual spherical harmonics (that are scalar quantities, so spin-0). On the other hand, the Stokes parameters Q and U enable to study the linear polarization and they are defined as follows

$$Q = \frac{1}{4}(I_{11} - I_{22}) \tag{1.26}$$

$$U = \frac{1}{2} I_{12} \tag{1.27}$$

The fact that the Stokes parameters rotate of an angle ψ as spin-2 objects needs to be taken into account, so

$$(Q \pm iU)(\hat{n}) \longrightarrow e^{\mp 2i\psi} (Q \pm iU)(\hat{n}) \tag{1.28}$$

For this reason, at odds with what has done for temperature anisotropy, harmonic expansions must be expressed in terms of *tensor spherical harmonics* (spin-2 objects) $Y_{\ell m}(\hat{n})$ as follows

$$(Q \pm iU)(\hat{n}) = \sum_{\ell} \sum_{m=-\ell}^{\ell} a_{\pm 2,\ell m} \, {}_{\pm 2}Y_{\ell m}(\hat{n}) \tag{1.29}$$

Subsequently, let's introduce the quantities

$$a_{E,\ell m} \equiv -\frac{1}{2} \left(a_{2,\ell m} + a_{-2,\ell m} \right); \quad a_{B,\ell m} \equiv -\frac{1}{2i} \left(a_{2,\ell m} - a_{-2,\ell m} \right) \tag{1.30}$$

In this way, it is possible to define and work with

$$E(\hat{n}) = \sum_{\ell,m} a_{E,\ell m} \, Y_{\ell m}(\hat{n}) \tag{1.31}$$

$$B(\hat{n}) = \sum_{\ell,m} a_{B,\ell m} \, Y_{\ell m}(\hat{n}) \tag{1.32}$$

which are two spin-0 fields, both invariant under rotations. Being scalar quantities, they are easier to be managed and enables to thoroughly describe the linear polarization. In particular, E-mode polarization vectors are radial around cold spots and tangential around hotspots on the sky, while B-mode ones have vorticity around any given point on the sky (as represented in Fig. 1.4)

So far, anisotropies in T and in polarization have been described, but, in addition, it is also possible to study how they correlate. While the TB and EB correlations cancel due to simmetries, the TE correlation and the EE, BB and TT autocorrelations are not zero and can be studied with the power spectrum (analogous to 1.19)

$$C_{\ell}^{XY} \equiv \frac{1}{2\ell + 1} \sum_{m=-\ell}^{\ell} \langle a_{X,\ell m}^{*}, a_{Y,\ell m} \rangle \tag{1.33}$$

with $X, Y = T, E, B$. As previously said, the study of CMB polarization is likely to give an unprecedented insight into the primordial Universe, and, in particular, great attention as been given to the study of B-modes. This because they can be originated by tensor perturbations, so by gravitational waves only (while E-modes can be due to both scalar and tensor perturbations). Therefore, the detection of B-modes ($C_{\ell}^{BB} \neq 0$) may be the proof of primordial gravitational waves, predicted by inflation. In addition,

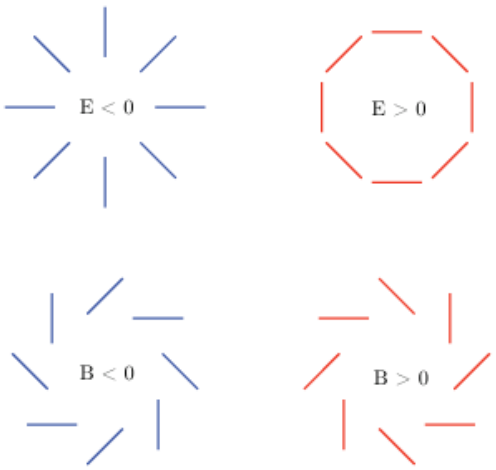

Figure 1.4: Diagram with a visual representation of E and B-modes. It is clear that when reflected with respect to a horizontal line passing from the centre (parity transformation), E-modes and B-modes behave in the opposite way: the latter change sign [3].

this detection would enable the study of physical processes taking place shortly after the Big Bang, at scales near the Planck scale ($\approx 10^{16}$ GeV) [14].The main practical difficulty in the detection is that the power of the signal associated to the B-modes is far lower with respect to that associated to the E-modes.

Chapter 2

LSPE, SWIPE and Strip

2.1 LSPE: the Large Scale Polarization Explorer

The LSPE (*Large Scale Polarization Explorer*) is an Italian-led international experiment, devoted to the study at large angular scale of the B-mode component of CMB polarization.

In particular, it aims at enhancing the knowledge of the current limit on the r (*tensor to scalar ratio*). This parameter describes the intensity associated with the tensor fluctuations with respect to the one of the scalar fluctuations, thus, a higher value of r would be sign of stronger gravitational waves in primordial Universe (generated by cosmic inflation). The current status of the estimates of the r parameter puts an upper limit $r < 0.044$ at 95% confidence level [1]. STRIP is expected to improve this results by putting the new upper limit $r < 0.015$ at 95% or by detecting $r = 0.03$ at 99.7% C.L. [1].

In addition, it will serve many other purposes, such as, among them, providing an advanced characterization of the atmosphere at the Teide Observatory and an improved map of the polarized foreground of the Milky Way.

LSPE will be structured around two instruments: the stratospheric balloon SWIPE and the ground-based telescope Strip.

However, it must be taken into account that, in order to expect to thoroughly study the B-mode component with the LSPE mission, it is of fundamental importance to characterise galactic foregrounds, as explained in the following paragraph.

2.1.1 Diffuse galactic foregrounds

It is particularly important to underline that the expected value of the amplitude of the signal associated to the polarized component of CMB is smaller with respect to that of the polarized galactic foregrounds [9], while, in the case of temperature foregrounds, the signals are almost comparable with that of CMB, as shown in Fig. 2.1

Thus, channels in both SWIPE and Strip specifically devoted to their monitoring

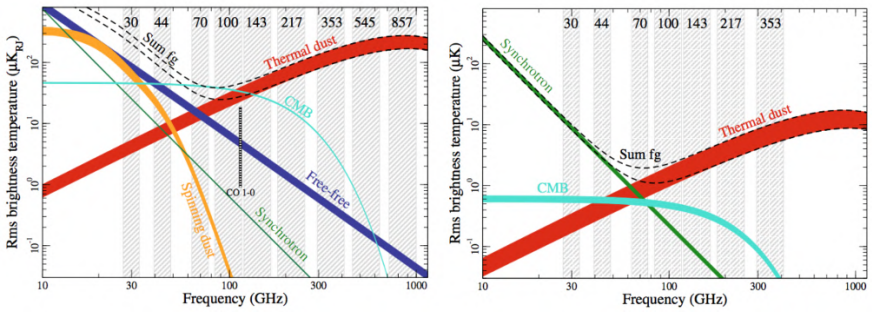

Figure 2.1: *Left panel*: Spectrum of diffuse foregrounds in temperature compared to that of CMB. There are several components, but comparable to the CMB signal. *Right panel*: Spectrum of diffuse foregrounds in polarization. There are less contributions, but the signal of CMB is way lower with respect to that of foreground. Derived from *Planck* data [23].

are of crucial importance, so as to subtract them and eventually isolate only the signal of the polarized CMB. At frequencies lower than 70 GHz, the synchrotron emission due to cosmic rays electrons accelerated by the Milky Way magnetic field is dominant, therefore, it will be monitored by the ground-based telescope Strip (being the atmosphere mostly transparent at those frequencies). At higher frequencies, the dust thermal emission must be studied by the SWIPE balloon, to avoid atmospheric absorption. Dust emits as a modified black-body with $T_d \approx 20$ K (see [10]) and a fraction of the emission can be polarized because grains are often aligned with the magnetic field of the Milky Way and they emit preferentially along their shortest axis.

2.2 LSPE-SWIPE: Short Wavelength Instrument for the Polarization Explorer

The SWIPE instrument is a telescope onboard a stratospheric baloon that was expected to be launched from Longyearbyen (Svalbard Islands), but, due to the ongoing conflict in Ukraine, the launch must be rescheduled. The instrument will fly at 35 km above sea level (in order to avoid the contamination due to the emission from the Earth's atmosphere). It will pursue two scientific measurements:

- **Intensity of the CMB peak**: will be studied by the channel at 145 GHz
- **Instensity of the emission of interstellar dust**: using channels at 210 GHz and 240 GHz.

The detection principle for the polarized component of the CMB is that the polarisation of the incoming radiation is rotated by a rotating cryogenic half-wave plate by a certain angle with respect to the incoming polarization axis. Then there is a polarising

grid. Only the component orthogonally polarized with respect to the wires of the grid passes, going towards the detectors, that are then able to study the polarization along a precisely selected direction.

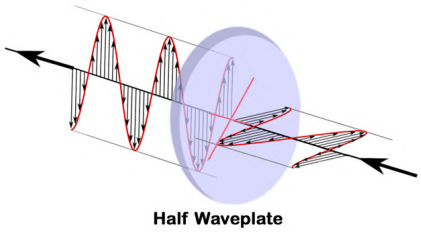

Figure 2.2: Schematic representation of the resulting rotation of the polarisation after passing through a half power plate.

The receivers consist in 326 TES (*Transition Edge Sensors*) bolometers populating a focal plane and cooled down to 0.3 K. For what concerns the observations, according to the original baseline plan, 38% of the boreal sky should be covered. However this number could change if the scanning strategy will be modified. The current scanning strategy is based on: (i) a continuous rotation of the telescope around the vertical axis passing from the gondola (azimuthal rotation), (ii) a zenithal rotation and all combined with (iii) the Earth's rotation. The observation will last almost two weeks during the Arctic winter, in order to improve the thermal stability of the bolometers (by avoiding Sun radiation).

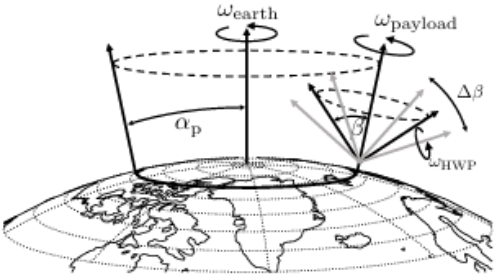

Figure 2.3: Sketch of the trajectory followed by LSPE-SWIPE. Its payload spin axis precesses (with angle α_p) around the North Pole. The telescope rotates around the local zenith at an angle β which can vary, as said. ω_{HWP} is the spinning frequency of the half-wave plate [1].

2.3 LSPE-Strip

LSPE-Strip is a microwaves instrument, scheduled to be installed at the Teide Observatory on Mount Teide (Tenerife). The core of the instrument is an array of 55 coherent polarimeters, that will study the sky with channels centred in two different frequencies: Q-band (43 GHz) and W-band (95 GHz). In particular, it will focus on the observation of:

- **Galactic synchrotron emission**: will be studied by the channel at 43 GHz
- **Local atmospheric emission and variability**: using channel at 95 GHz.

Specifically, the synchrotron emission is studied by 49 Q-band (centred at 43 GHz) polarimeters organized in 7 modules (each containing 7 polarimeters and named after the initial letter of the colours of the iris: O, R, V, Y, I, G and B). Then, there are the 6 W-band (centred at 95 GHz) polarimeters, named as W followed by a number from 1 to 6, that will be dedicated to the study of the atmospheric fluctuations at the Teide Observatory, mostly due to water vapours.

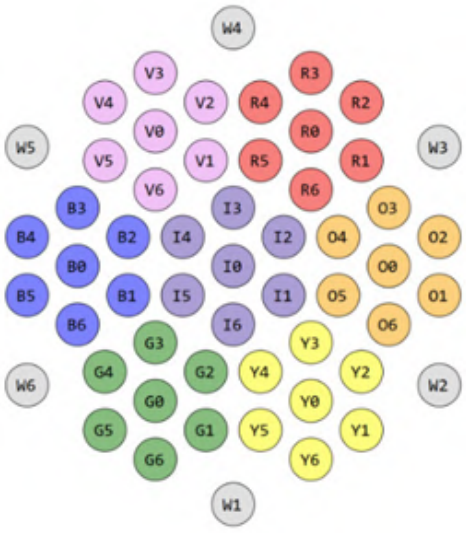

Figure 2.4: Scheme of the arrangement of the Q and W-band polarimeters in the focal plane, projected onto the sky.

2.3.1 Architecture and Subsystems

The two reflectors are among Strip's telescope main components, with a parabolic primary mirror (with a projected diameter of 1.5 m) and a hyperbolic secondary mirror, organised in a Dragonian cross-fed design. A co-moving baffle (made of aluminum

plates covered by a millimetre-wave absorber) encloses the telescope, in order to reduce the leakage of spurious radiation. In terms of resolution, $\approx 20'$ and $\approx 10'$ wil be reached in Q-band and W-band respectively.

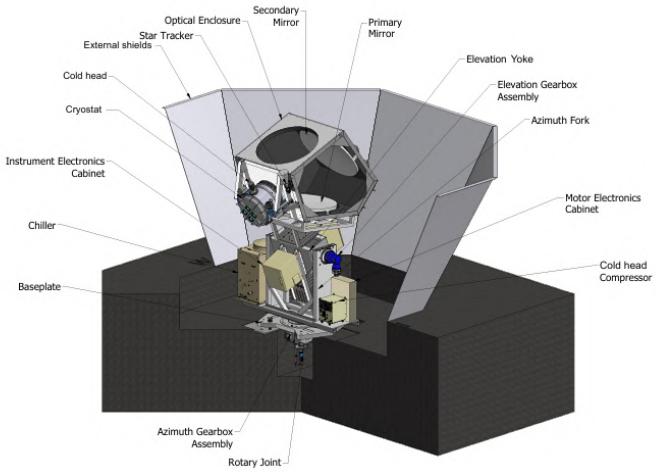

Figure 2.5: Model of Strip's telescope structure [1].

The subsequent description of the instrument will follow the path of the electromagnetic wave towards the detectors, and then explain how the data are acquired.

All the polarimeters of the focal plane must be cooled down to cryogenic temperature and maintained under vacuum condition. For this reason they are enclosed in a cylindrical cryostat.

The polarimeters in the focal plane observe the sky through a UHMWPE (*Ultra-High Molecular Weight PolyEthylene*) window, having a diameter of 586 mm and 56.34 mm thick. It is mostly transparent at frequencies in bands Q and W, so as to let the radiation pass, and its large thickness is necessary in order to bear even large pressure gradients without bending too much or, even, breaking. It is important to underline that there is a several orders of magnitude difference between the internal pressure and the external one (such as $P_{int} \approx 10^{-7}$ mbar in nominal conditions and $P_{out} \approx 10^{3}$ mbar). The window has crossed grooves on the front and on the back, to preserve the polarization of the incoming radiation as it passes through it. The window is in thermal contact with the external walls of the cryostat at ambient room temperature 300K or less (depending on the environmental conditions).

Then, there are 13 PTFE (*Polytetrafluoroethylene*) infrared filters, necessary so as to stop the spurious radiation coming from the environment at 300 K. They present grooves orthogonally oriented on the two sides of the filters, in order to avoid the introduction of spurious polarization. They are mounted on the radiative shield of the cryostat by a circular mounting structure (filters holder wheel) enhancing their

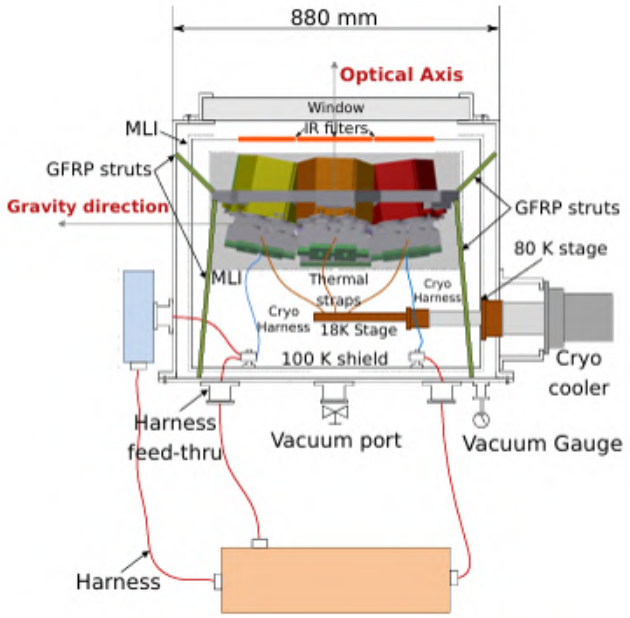

Figure 2.6: Cross-sectional schematic representation of the Strip's cryostat and subsystems [1]. Some components have been modified, with respect to the scheme, during the optimisation process, such as the GFRP struts.

thermalisation at temperature close to that of the shield, that is thermalised with the first stage (reaching ≈ 80 K) of a Gifford-McMahon Helium cryocooler. Thus the filters re-emit the hot radiation from the exterior towards the interior, but at 100 K. There is one filter for each board of polarimeters at 43 GHz and one for each horn at 95 GHz, as shown in Fig. 2.7.

In particular, the external surface of the radiative shield is covered with MLI (*Multi-Layer Insulation*) to shield radiatively, in order to reduce the radiative heat load from the external walls onto the most internal components.

Copper thermal straps are used to connect the cryocooler second stage (the colder one, at ≈ 18 K) to the focal plane, so as to cool the array of polarimeters down to ≈ 20 K.

The focal plane presents 55 aluminum corrugated feedhorns, each connected to a coherent polarimeter, by a polarizer and a OMT (*Orthomode Transducer*), at 43 GHz, or a septum polarizer, for the ones at 95 GHz. Their aim is to convert the orthogonal components of the electric field of the incoming radiation (E_x, E_y), with the radiation propagating along $\hat{z}$, into circular polarization components $\left(\frac{E_x+iE_y}{\sqrt{2}}, \quad \frac{E_x-iE_y}{\sqrt{2}}\right)$, and make this two different polarization components follow separate paths along the two legs of the subsequent module (the polarimeter).

For what concerns the polarimeter, an overview of the main components will be

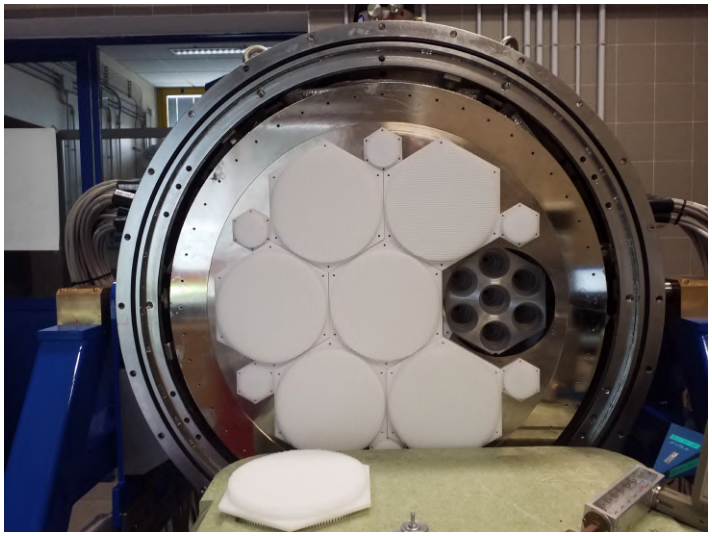

Figure 2.7: Photograph showing 12 of the 13 PTFE IR filters of Strip mounted, taken at the INAF-OAS cryogenic laboratory.

provided.

Each polarimeter has two legs, each presenting three cascaded LNA (*Low Noise Amplifiers*) based on HEMT (*High Electron Mobility Transistor*), named as indicated in Fig. 2.9. They are necessary in order to amplify the very weak signal without increasing too much the noise, thus, they increase the S/N (*signal to noise ratio*). In particular, the incoming signal is amplified by almost 50 dB (which is a factor 100.000, given the fact that the dB scale is logarithmic).

Then, each leg has a Phase Switch made of two PIN diodes. There is a $\frac{\lambda}{2}$ difference in microstrip path lengths built into the circuit, so, depending on which diode is forward-biased, a 0° or 180° phase shift is introduced. The Phase Switches can operate in *steady* (PIN diodes in a fixed configuration) or *switching*, with a frequency of 4 kHz on leg A and of 100 Hz on leg B, as schematically represented in Fig. 2.10

The result is a shift in the sign of Q (or U) measured in the respective detector diodes. Thus, they are able to transform the signal, to then distinguish the Stokes parameters Q and U from I and make the $\frac{1}{\nu}$ noise smaller, thanks to a double demodulation process (described later).

Then a 180° hybrid is present, to mix the signals from the two legs, followed by a power splitter to separate the signals in different paths: one part of the signal is going towards a bandpass filter and then through the first two detector diodes (named Q1 and Q2). The other part of the signal is at first passing through a 90° hybrid and then towards the other two detectors (called U1 and U2), by two bandpass filters.

The aim of the detector diodes is to transform the incoming RF signal into a voltage, to be subsequently digitized (ADC conversion) and processed (integration

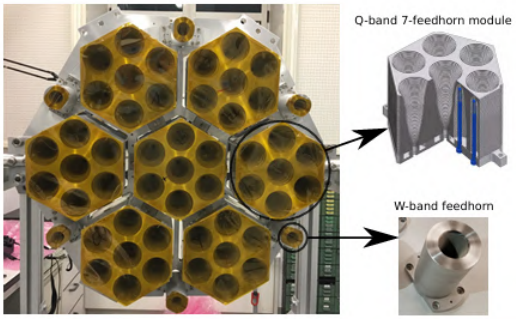

Figure 2.8: The 55 feedhorns of Strip's polarimeters in its focal plane. The Q-bands polarimeters are organised in the hexagonal boards, while the 6 W-bands ones are at the midpoints of the sides of the focal plane. Cutaways of the polarimeters are also shown [1].

and demodulation) in back end electronics. Then obtain information on the Stokes parameters and on the intensity I.

The instrument can be controlled by the EGSE (*Electronic Ground Support Equipment*), that is a workstation with a dedicated software. It is able to send instructions to the polarimeters through the electronic boards. In particular, there are 7 pairs of electronic boards, each connected to Q-board and a W-band polarimeter. Each pair consists of:

- **BIAS board**: their main scope is to set and acquire several *housekeeping* quantities of the LNAs, such as tensions and currents, or to set the status of the Phase Switches
- **DAQ (*Data AcQuisition*) board**: they acquire the proper scientific data (output of the polarimeters) and are responsible for its sum, demodulation and storage in the EGSE in HDF5 files.

And there is also the

- **Master Clock board**: Connected to the GPS antenna of the instrument distributes the time syncronizing the DAQ and BIAS boards, necessary in order to associate to each data its own acquisition time stamp.

The connection between the electronics and the polarimeters is provided by the electric harness, consisting of: at first copper cables, connecting the electronics to the cryostat of Strip (by the *feedthrough*), and secondly, in the interior, the *feedthroughs* are connected to the polarimeters by cables of copper and manganine. Obviously, the main aim is to provide good electric conductance (to reduce signal loss), while limiting the heat load coming from the exterior (limiting thermal conductance).

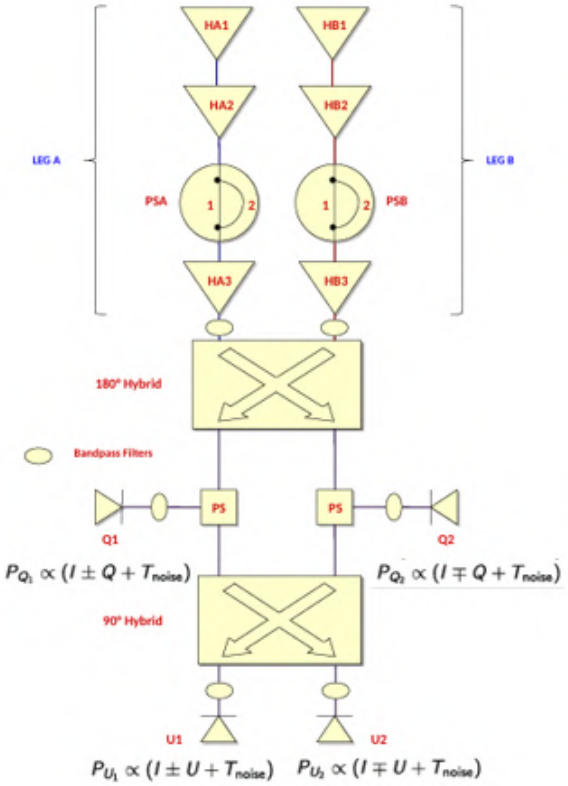

Figure 2.9: In the figure the sketch of the Strip's polarimeter structure is represented. In addition, the power outputs of the diodes and how they are related to the Stokes parameter and the system noise temperature are reported [1] [15].

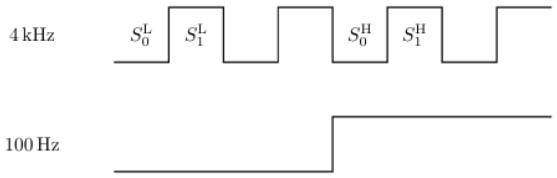

Figure 2.10: Visual sketch of the different signals S that could be detected by the diodes. Due to the switching of the PIN diodes (at two different frequencies), 4 different signals can be detected and then will undergo further processing.

Finally, from the *feedthroughs* an analogic signal exits and it is then converted into a digital one through an ADC converter in the electronics. The electronics, DAQ boards in particular, manipulates the signals from the detectors, so as to get the modulated signals PWR and DEM at 100 Hz (first demodulation, important to reduce the $\frac{1}{\nu}$ noise, mostly caused by the gain fluctuations of the amplifiers). It involves performing the

sum of the sum (or of the difference) of 40 consecutive 4 kHz samples. Obviously, this must be done for both the "high" and "low" state of the slow Phase Switch. The results are, for any of the four detector diodes:

$$\begin{aligned} \mathrm{PWR}^L &= \sum_{t=1}^{20} S_1^L + S_0^L, \qquad & \mathrm{DEM}^L &= \sum_{t=1}^{20} S_1^L - S_0^L, \\ \mathrm{PWR}^H &= \sum_{t=1}^{20} S_1^H + S_0^H, \qquad & \mathrm{DEM}^H &= \sum_{t=1}^{20} S_1^H - S_0^H \end{aligned} \tag{2.1}$$

resulting, in terms of dependancies, in:

$$\begin{aligned} \mathrm{PWR}_X^L &\propto I + O(\varepsilon \tilde{X}), \qquad & \mathrm{PWR}_X^H &\propto I + O(\varepsilon \tilde{X}), \\ \mathrm{DEM}_X^L &\propto \pm\tilde{X} + O(\varepsilon I), \qquad & \mathrm{DEM}_X^H &\propto \mp\tilde{X} + O(\varepsilon I) \end{aligned} \tag{2.2}$$

where each PWR and DEM signal can be associated to each of the four detectors (Q1, Q2, U1, U2). The second demodulation takes place afterwards, during the data analysis, and is performed by a software in the data post-processing. In particular, the following computations are performed, involving consecutive pairs of PWR and DEM data

$$\begin{aligned} \mathrm{I}_X &= \mathrm{PWR}_X^H + \mathrm{PWR}_X^L, \\ X &= \left|\mathrm{DEM}_X^H - \mathrm{DEM}_X^L\right| \end{aligned} \tag{2.3}$$

The result is a data stream sampled at 50 Hz, and where X can be again any of Q1, Q2, U1 and U2. Eventually, the values of the Stokes parameters are obtained as

$$\begin{aligned} I &\propto I_{Q_1} + I_{Q_2} + I_{U_1} + I_{U_2}, \\ Q &\propto Q_1 + Q_2, \\ U &\propto U_1 + U_2 \end{aligned} \tag{2.4}$$

Chapter 3

The Strip Calibrator

In the following sections of the chapter, the Strip calibrator will be the main focus. At first, the aim and importance of the verification phase during the development of the Strip instrument is highlighted. Thus, the need for the calibrator is introduced. Then, details will be provided regarding the properties that the calibrator should have in order to fulfil the requirements of the instrument and how this can be practically obtained. In the last section, there will be the description of the final implementation of the aforementioned needs into the current calibrator system.

3.1 Strip verification campaign

The main aim of the verification phase is to accurately characterise Strip and to optimise its performances in the laboratory before moving it to the observation site (Tenerife, Izaña). Although the calibration will be performed and periodically repeated at the site by observing known celestial sources, it is nevertheless appropriate and necessary to characterise Strip in the laboratory under the most favourable setup conditions.

Several aspects are dealt within the verification campaign phase, such as the evaluation of the system noise, the verification of the linearity of the signal, the band-pass response and the response of the instrument to polarized signals.

In particular, it is of crucial importance to estimate the noise properties (in terms of noise temperature T_{noise}, added to the signal measured by an ideal radiometer, and noise spectrum) and the responsivity of the instrument.

In this way, it could be possible to find the configuration with the best sensitivity by reducing as much as possible the estimated noise temperature, through a dedicated procedure commonly called LNAs bias tuning [8], and to study the spectral characteristics of the system noise.

In particular, the system noise power spectrum associated to the signal measured by Strip is made of two components: a white noise component (thermal noise) and a low-frequency component (called flicker, related to fluctuations in the intrinsic noise).

In particular, the relation describing the noise power spectrum is the following

$$P(\nu) = \sigma^2 \left[1 + \left(\frac{\nu_{\text{knee}}}{\nu}\right)^{\alpha}\right] \tag{3.1}$$

where ν_{knee}, the knee frequency, is the frequency when the two components of the noise give the same contribution.

For what concerns the **white noise**, it shows a constant behaviour with the frequency and is described as follows:

$$\sigma = \frac{T_{\text{load}} + T_{\text{noise}}}{\sqrt{\Delta\nu\,\tau}} \tag{3.2}$$

with τ being the integration time and $\Delta\nu$ the bandpass.

The **flicker noise** is mainly due to gain fluctuations of the Low Noise Amplifiers (LNAs). However, it is important to underline that the aforementioned Strip's double demodulation is aimed at the reduction of the effect of the gain fluctuations (see [17]).

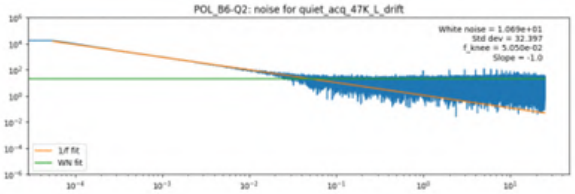

Figure 3.1: Graph showing the noise spectrum from the polarimeter B6-Q2 at 47 K. It is possible to see the flicker noise up to ($\nu \approx 10^{-2}$ Hz), that is ν_{knee}, then the white noise becomes dominant.

The noise temperature T_{noise} can be estimated through the Y-factor method. It consists in making the polarimeters observe two known different reference signals (with known associated temperatures). Then, by obtaining also the measured values of the voltage output (indicated as S in the plot below), the following graph can be built (provided that the receiver is in a linear regime, which can be verified by acquiring 3 or more points corresponding to as many different temperatures. In this way, two fundamental parameters can be obtained: T_{noise} (the temperature axis intercept, thus obtained for $S = 0$) and the responsivity α (that is the slope of the line).

From a mathematical point of view, the noise temperature T_{noise} can be obtained directly from data as

$$T_{noise} = \frac{T_{warm} - yT_{cold}}{y - 1} \tag{3.3}$$

where T_{warm} and T_{cold} are the temperatures associated to the two known reference signals and $y = \frac{S_{warm}}{S_{cold}}$.

The responsivity α of the instrument is the angular coefficient of the line represented in the plot and, therefore, is described by the following relation

$$\alpha = \frac{\Delta S}{\Delta T} \tag{3.4}$$

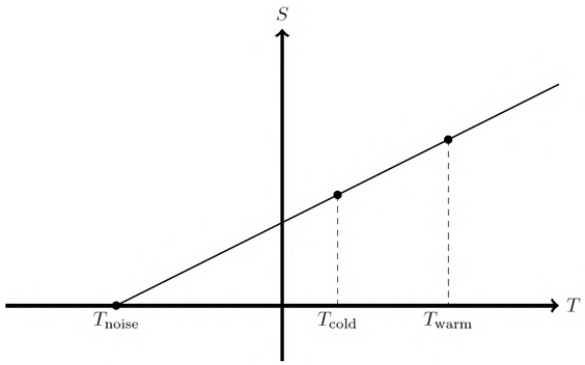

Figure 3.2: Plot showing how the noise temperature is estimated through the Y-factor. The two points obtained are plotted, with the line connecting them. The negative intercept on the x-axis is correspondent to the value of the noise temperature.

3.2 Strip calibrator needs

In order to fulfil the requirements for the calibration of Strip, outlined in the previous paragraph, the calibrator is the source of the known signals that is used to measure the system noise and the receivers responsivity.

Therefore, the calibrator must present several properties, both from the RF (Radio Frequency) and thermal points of view

For what concerns the **RF needs**, the most important ones are the following:

- Emissivity $\varepsilon \approx 1$
- The emitted signal intensity must be close to that of the CMB, because calibration must take place in a range near the one of the observation campaign, to ensure that the receivers operate within a similar response range

While the main **thermal needs** are:

- The operative temperature should be as technically close as possible to that of the CMB ($T \approx 2.725$ K)
- Possibility to vary the calibrator temperature still near 20 K (for example, to obtain both the T_{warm} and T_{cold} needed to apply the Y-factor method)

- Thermal stability (over a certain time, depending on the experiment)
- Thermal homogeneity throughout the calibrator itself

Therefore, it is necessary to identify calibrating units having the just mentioned properties. In particular, ideal Black Bodies are among the best choices when there is the need to calibrate an instrument, given the fact that, from a theoretical point of view they satisfy both RF and thermal requirements (while, on the practical side, RF and thermal requirements are often in contrast).

RF requirements

The intensity of the radiation emitted can be described in terms of the brightness temperature T_B (the temperature that a perfect Black Body should have in order to emit the same amount of radiation of a source at T) through the Planck law

$$I(\nu, T_B) = \frac{2h\nu^3}{c^2} \cdot \frac{1}{e^{\frac{h\nu}{k_B T_B}} - 1} \tag{3.5}$$

which, in Rayleigh-Jeans regime (for $h\nu << k_b T_B$) becomes

$$I(\nu, T_B) \approx \frac{2\nu^2 k_B T_B}{c^2} \tag{3.6}$$

In addition, Black Bodies are by definition perfect absorbers (absorptivity is indicated as α), meaning that they have reflectivity $r = 0$. Therefore, by using Kirchhoff's law for a material with negligible trasmittivity (condition that can be ensured through a reflective metallic layer placed behind the BB) and at equilibrium ($\varepsilon = \alpha$, see [7])

$$\varepsilon = 1 - r = 1 \tag{3.7}$$

In our case, the requirement is an emissivity of $\varepsilon > 0.999$, achieved through the combined effect of the form factor and the material, ensuring near-blackbody behavior.

But if the emissivity of a body is equal to one, then its physical temperature perfectly corresponds to its brightness temperature, given

$$T_{phys} = \varepsilon T_B = T_B \tag{3.8}$$

The choice of Black Bodies as calibrators is then convenient, because, through a measurement of their physical temperature, the intensity of the signal emitted can be derived by using eq. 3.8 into eq. 3.6, and in this way the first RF requirements is fulfilled. Thus, by determining their physical temperature, using thermometers distributed in them, radiometric receivers are calibrated by observing the emitted radiation under the assumption that the physical temperature equals the brightness temperature.

An important requirement regards the dimension of the blackbody, that must fully subtend the solid angle of the radiometer array's field of view. In particular, the BB must fill the beam of each feedhorn, within a defined power level. In our case, -20 dB is the level (meaning that only a fraction of the beam $< 1\%$ is illuminated by sources other than the BB. This fraction is named "spillover").

Thermal requirements

An ideal Black Body is thermally homogeneous throughout its volume (there are no spatial temperature gradients).

Blackbodies are thermally stable over time (there are no temperature time gradients).

These two properties can be derived by the fact that a Black Body is defined as a body in thermal equilibrium.

Their temperature can be varied, typically by enclosing them in cryogenic system and cooling them down or by heating them. Thus, they are flexible from a thermal point of view and a proper choice when it comes to calibrate an instrument and more than one reference signal is needed, as is the Y-factor method.

However, since real targets do not have perfect emissivity or uniform temperature, the goal in designing calibrating units is to make them resemble ideal Black Bodies at a level within the required specification.

3.3 Strip calibrator design

Given what said in the previous paragraph, a careful and proper choice in the design of the calibrator must be considered to implement the outlined needs.

Again, a distinction between radio frequency (RF) needs and thermal ones can be done, yet it must be highlighted that they must be fulfilled together in the final design of the calibrating units.

Starting from the **implementation of the RF needs**, a passive calibrator (does not contain Microwave or Radio active sources) has been chosen. In order to obtain this feature, the design of the calibrator must be optimised, especially in terms of an appropriate choice of the microwave absorbing material (materials intrinsically characterised by high emissivity in the STRIP operational frequency range), and also its geometry. In fact, by recalling the relation between emissivity ε and reflectivity r reported in eq. 3.7, it is clear that, so as to have a calibrator with high emissivity, it is necessary to reduce as much as possible its reflectivity. The result is that calibrating units must be built with a geometry that enables to absorb almost all of the incident radiation. In order to do so, a commonly used solution is that of an array of square-based pyramids, due to the fact that this geometry perfectly fits the required high performances of low reflectivity. In fact, the fraction of power reflected at a boundary between two media

with different impedences is given by the reflectivity r

$$r = \left| \frac{Z_2 - Z_1}{Z_2 + Z_1} \right|^2 \tag{3.9}$$

where Z_1 is the impedance of free space (377 Ω) and Z_2 is the impedance of the absorbing material [6]. A large impedence discontinuity results in high reflectivity and low absorption, while a gradual impedance change reduces r and allows more energy to be absorbed. The pyramidal geometry creates a gradual impedence transition between free space and the absorbing material. At the tip of the pyramid, the wave initially encounters only a small cross-section of the absorber, where the effective impedance is close to that of free space. As the wave penetrates deeper into the pyramid, it progressively interacts with larger sections of the absorber, causing the perceived impedance to change slowly rather than abruptly. This gradual impedence variation reduces reflections because the wave encounters no sudden discontinuities. Instead of being partially reflected at a sharp boundary, the RF energy is gradually coupled into the absorber and efficiently dissipated, increasing the absorptance, as required.

Furthermore, the periodic array of pyramids enhances also the multiple scattering of any residual reflected radiation among the pyramid walls. This process increases the effective absorption, as the energy is either absorbed directly or after multiple reflections. The absorber's efficiency is further optimized by carefully choosing the slant angle, the pyramid height, and the spacing, which together determine the opening angle, distance, and overall effectiveness of the structure.

For what concerns the choice of the materials, those with intrinsically high emissivity (so high absorption capabilities) are usually adopted. Common choices are carbon - or ferrite-loaded polymer foams, epoxy resins and carbon-loaded plastics. These inclusions cause the electric and magnetic fields of incident microwave radiation to generate currents and magnetic responses that are partially dissipated as heat, reducing reflection and efficiently absorbing the energy. In particular, the Eccosorb materials of the CR/MF-series [1] are widely used in astrophysics (more details on the Eccosorb materials are reported in Chapter 4).

For the **implementation of the thermal requirement** of temperature homogeneity, conductive materials should be selected, such as the metals, which are highly reflective. Therefore, this is in contrast with what suggested by the RF requirements. In addition, the pyramidal geometry, meeting the main RF requirements, favours the development of an undesired thermal gradient along the direction of the height of the pyramid.

Therefore, the aim is to reconcile cryogenic thermal requirements and RF requirements. The usual strategies are: to use a thin absorber (having large emissivity) coated on a metal core with a tapered geometry (pyramid), to get a satisfactory absorption of the incident wave while preventing the development of a temperature gradient, or to

[1] https://www.laird.com/products/absorbers/structural-absorbers/castable-liquid-absorber/eccosorb-cr

obtain a cavity effect (to prevent the absorber to be exposed to a large radiative heat load).

In our case, it is not possible to choose the latter strategy, due to the necessity to illuminate a wide focal plane. The choice made is to use available panels of pyramids made only of absorbing material (there is no metallic core). The temperature gradient created along the height of the pyramids is expected to be characterised, in order to recover the overall load brightness.

Moreover, for what concerns the availability of two reference temperatures, in the calibrator there are two different arrays of pyramids, characterised by two different known temperatures. They are mounted and assembled in order to let the Strip's polarimeters study both the arrays. In this way it would be possible to have the two desired references at T_{warm} and at T_{cold}, which can be displayed alternately by periodically rotating the device in front of the receivers, without the need to wait for a single array to be cooled down or heated up. The way in which the two arrays will be 'alternated' in front of each of the polarimeters will be described in the next paragraph.

3.4 Final implementation design

In order to fulfil all the previously outlined requirements, a specific architecture for the calibrator system has been adopted.

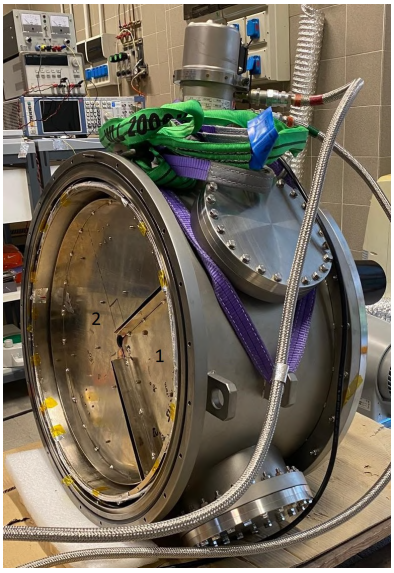

Figure 3.3: Photograph showing the external walls of the calibrator cryostat and the $\frac{1}{4}$ and $\frac{3}{4}$ slices, labelled respectively as 1 and 2.

Cooling the calibrating units down is necessary in order to reach the required temperature of $T \approx 20$ K, as one of the main thermal requirement. Thus, the arrays of pyramids have been enclosed in a cryostat to keep them under thermal vacuum.

The aim is to reach and maintain such cryogenic temperatures. A cylindrical vacuum vessel has been adopted, with properly sealed joints used to maintain the internal parts insulated from the exterior.

Vacuum pumping is of crucial importance to deal with one of the major issues: limiting convection heat load. Specifically, two types of vacuum pumps are used: a Scroll pump (dry-oil free vacuum pump), in order to obtain a pre-vacuum, and, after having reached $P \approx 10^{-2}$ mbar, a turbomolecular pump is turned on, bringing the internal pressure of the cryostat to $P \leq 10^{-4}$ mbar. Lower values of pressure are reached thanks to the subsequent action of the cryocooler. The pressure inside the vacuum vessel is monitored through a pressure sensor.

In the nominal condition, the calibrator cryostat is mounted in front of Strip's focal plane. As shown, Strip is equipped with a vacuum **UHMW-PE window** that allows the passage of microwave radiation while maintaining the vacuum. The vacuum window also serves as interface between Strip and the calibrator when the latter is integrated in front. Two O-rings are required for this coupling to preserve the vacuum.

A second mounting scheme is also possible, in which the calibrator is integrated in front of Strip without the vacuum window. This architecture, which will be used in system tests, has both pros and cons. The positive aspect is that it allows the calibrator to reach lower temperatures (as it is not affected by the IR emission of the window). The negative one is that the window would not be considered in the characterization of Strip's noise properties.

Starting the description of the calibrator's internal subsystems, there is a **PTFE Infrared filter** used to block IR thermal radiation coming from the external environment (see Fig. 3.4).

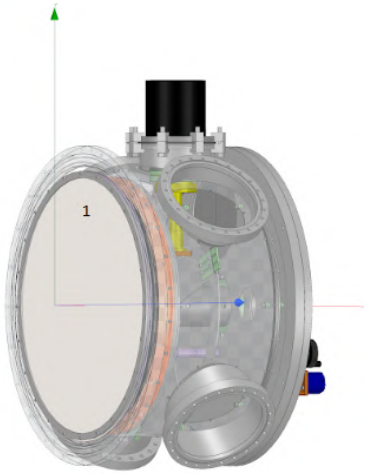

Figure 3.4: CAD image showing the calibrator cryostat with the IR filter mounted (1).

In fact, to reach the thermal requirements, the radiative heat load onto the calibrating units must be reduced as much as possible. The filter has external diameter and height of 590 and 3 mm respectively, internal diameter and height of 568 and 6 mm respectively.

The filter is thermalised with the **radiative shield** of the cryostat. The shield is covered by MLI (Multi Layer Insulation) that, as for Strip, reduces the radiative heat load coming from the external walls of the cryostat (having a physical temperature of $\approx$ 300 K). Therefore, the radiative shield acts as a thermal shield for the innermost subsystems.

The radiative shield is in thermal contact with the first stage of a **two-stages Gifford McMahon mechanical cryocooler**. The presence of the first stage is important in order to let the second stage of the cold head reach cryogenic temperatures of the order of $\approx$ 18 K. In fact, the first stage absorbs most of the parasitic heat from the environment and mechanical connections, reducing the load on the second stage. This allows the second stage to reach the required much lower temperatures without being overloaded.

The **arrays of pyramids** (the actual blackbody) are located in the innermost part of the cryostat. They are divided and hosted in two different sectors, occupying respectively $\frac{1}{4}$ and $\frac{3}{4}$ of the total circular surface, parallel to the filter (see Fig. 3.5). This solution enables to have simultaneously two sectors (pyramidal arrays) possibly at two different reference temperatures (T_{warm} and T_{cold}), which was one of the main requirements.

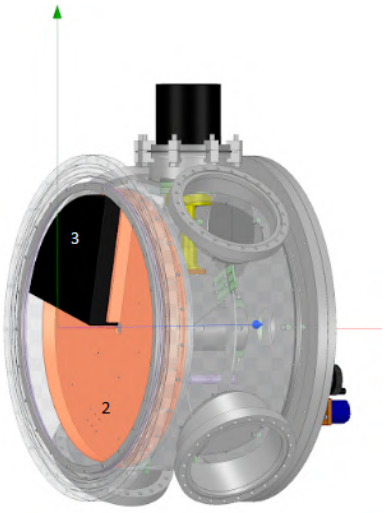

Figure 3.5: CAD image showing the calibrator cryostat with the $\frac{1}{4}$ and $\frac{3}{4}$ slices(2 and 3). The $\frac{1}{4}$ slice is hosting its blackbody (3).

To cooldown the two arrays to the required temperatures, they are separately connected to the second stage of the cryocooler. Copper thermal straps are used to establish this thermal link (as shown in Fig. 3.6).

Figure 3.6: Second stage of the cold head of the cryocooler, with thermal straps.

The slices are connected to a rotating support (**wheel**) via fiberglass spacers, limiting conductive exchanges between the slices and the rotating wheel. When the support is rotated by 180°, the individual polarimeter can alternatively observe both the temperature references (so both sectors $\frac{1}{4}$ and $\frac{3}{4}$). In particular, the rotating wheel is mechanically coupled to a shaft and a drive system, enabling its rotation either manually, by using a hand crank mounted on the rear exterior of the cryostat, or automatically through a motorized control (see Fig. 3.7)

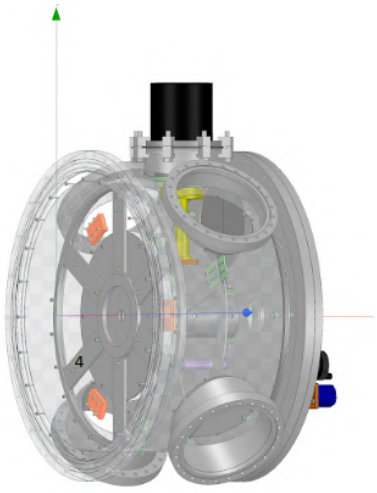

Figure 3.7: CAD image showing the calibrator cryostat with the rotating wheel (4).

Such rotating shaft is supported by a structure mounted onto the external walls of the cryostat through **fixed rays** (Fig. 3.8)

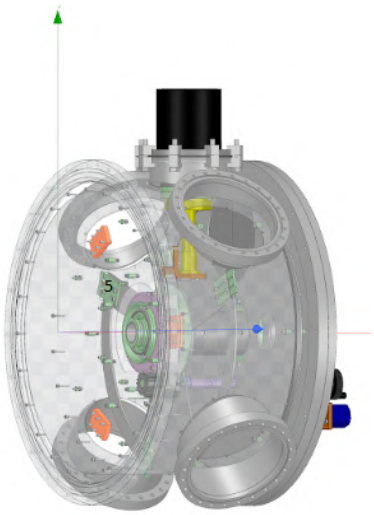

Figure 3.8: CAD image showing the calibrator cryostat with the fixed rays structure (green, 5).

The temperatures inside the calibrator cryostat are monitored through thermometers (Silicon diodes and Cernox resistors) deployed in several subsystems. In particular, the thermometers are attached to:

- Cold Head II stage
- Cold Head I stage (Radiative Shield base)
- Thermal strap, near the Cold Head
- Thermal strap, near the slice
- Slice $\frac{1}{4}$
- Slice $\frac{3}{4}$
- Rotating wheel
- Central Back disk
- IR filter
- Pyramids (one for each array)

Their temperature is acquired by an external monitor, connected through flat cables.

Chapter 4

Calibrator Thermal Verification

Upon delivery of the calibrator cryostat (described in the previous chapter) to the INAF OAS Cryowaves Laboratory, several acceptance tests have been performed. In fact, it is necessary to test both the thermal-vacuum performances of the calibrator cryostat stand-alone and when mounted in front of Strip. These tests will be called *Dry Runs* because they do not imply the nominal condition of the system and are intended to provide a better understanding of the operation under simpler usage conditions. Therefore, they are performed to verify the pressures and temperatures that can be reached and maintained by the subsystems, in order to have a characterization of the calibrator cryostat from a thermal point of view and verify the heat exchanges between its subsystems, comparing them to the estimations.

Actually, a simple thermal model of the calibrator has been implemented, in order to support design activities and estimate the system performances; the ThermXL modelling software [1] has been used also to estimate the impact of the IR filter implementation inside the cryostat.

The overall test flow of the verification campaign of the calibrator cryostat is the following:

- **Step 1**:Functional verification test of the stand-alone calibrator cryostat, without the array of pyramids. This first step aims to test whether the temperatures inside the cryostat are compliant with this project design need. If they are within the expectations, then proceed with the next step. Otherwise, a failure analysis and subsequent recovery actions are run before repeating the test.

- **Step 2**: It consists in the integration of the calibrator cryostat (still without the arrays of pyramids) in front of Strip's focal plane. A cooldown of the whole system is run in order to verify that the two systems are properly working when integrated in this setup. If the results of the test are successful, then move to Step 3.

[1] https://www.esatan-tms.com/products/catdescription.php?ID=9

- **Step 3**: Cooldown cycle of the calibrator cryostat stand-alone, with the nominal blackbody (array of pyramids) integrated inside. This step is aimed at verifying that the temperature distribution is kept within expectation with the additional heat load absorbed by the pyramid array.
- **Step 4**: It consists in the verification of the nominal configuration: the complete calibrator integrated in front of Strip. Both systems are cooled and in nominal operating conditions.

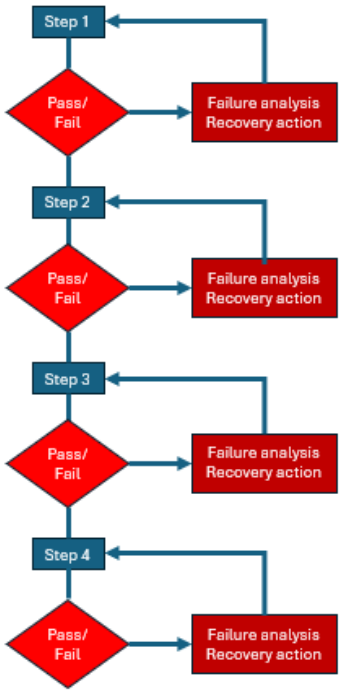

Figure 4.1: Diagram showing a visual representation of the verification flow outlined in the paragraph.

In my activity I took part in the calibrator verification campaign, starting from Step 2 and finishing with the preliminary verification of the complete system (Strip with calibrator integrated).

4.1 Thermal model of the system and performance estimation

When designing a system from a thermal point of view, dedicated software and tools are used to model the system. The process consists in detailing more and more

the model as the overall design evolves and involves different iterations of making predictions on the expected results and correlating them to experimental results.

4.1.1 Thermal modelling basic principles

In order to build the thermal model of a system, it is convenient to represent it as a discrete network of small 3D volumes. Each of them containing only one nodal point, specifically at the centre of the volume ("Lumped Parameter" method). The heat transfer is considered to happen only between nodal points belonging to different volumes. They store all the thermal energy of that small volume and are imagined as connected by fictitious rods, acting as conductors/resistors for the heat flow [21].

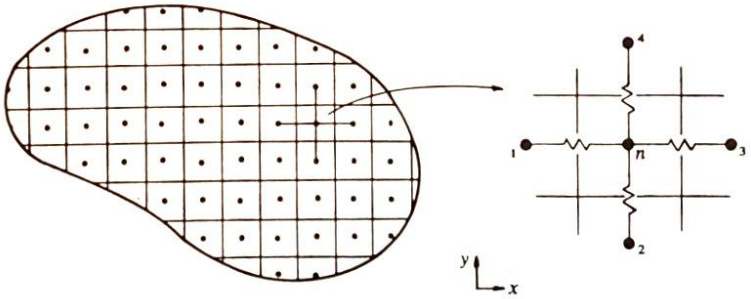

Figure 4.2: Scheme representing a generic volume V that can be modelled as an ensemble of small volumes, each containing a single nodal point at its centre (from [21]).

The reason why this approach is convenient lies in the possibility to solve a system of algebraic equations (describing the thermal balance between different nodes) instead of a non-trivial differential equation. The latter one describes the continuous temperature distribution of the system in both space and time, while the system of algebraic equations gives results only at specific points in space and at specific times. However, the system involves a finite number of variables and equations that can be solved by means of standard numerical methods, by hand or by dedicated software, depending on the complexity of the system under examination [12].

By considering a system seen as a network of n nodes denoted as N_i with $i = 1, ..., n$, each would be characterised by its own temperature T_i, heat capacity C_i and internal heat source Q_i. The thermal balance equation between node i and node j is

$$C_i \frac{dT_i}{dt} = \sum_{\substack{i=1 \\ i \neq j}}^{n} K_{ij}(T_j - T_i) + \sum_{\substack{i=1 \\ i \neq j}}^{n} R_{ij}(T_j^4 - T_i^4) + Q_i \tag{4.1}$$

where the linear conductance between i and j is described by K_{ij} and R_{ij} is the radiative exchange constant.

When studying the heat exchanges at equilibrium, $\frac{dT_i}{dt} = 0$, therefore the previous equation becomes

$$\sum_{\substack{i=1 \\ i \neq j}}^{n} K_{ij}(T_j - T_i) + \sum_{\substack{i=1 \\ i \neq j}}^{n} R_{ij}(T_j^4 - T_i^4) + Q_i = 0 \tag{4.2}$$

The set of these equations constitutes the system of algebraic equation to be solved numerically, in order to derive the parameters describing the linear and radiative conductances and the input power Q.

In particular, the heat load must be counteracted by the cooling power of an active stage of a cryostat, when a system has to be set to low temperatures. For this reason, the main task when designing and modelling a cryogenic system is to estimate the amount of heat load coming from the environment down to the inner stages of the cryostat, so as to make a proper choice in terms of the used cryocooler, optimise the system from a thermal point of view and, thus, reach the desired temperatures.

4.1.2 Heat Transfer

This paragraph provides an insight on the possible heat exchanges taking place between different nodes that must be considered when building a thermal model.

Specifically, the heat exchanges that are considered in the thermal model of a cryostat are radiative and conductive, due to the fact that convection heat transfer must be effectively limited through a proper vacuum pumping over the cryostat chamber.

Conduction heat transfer taking place from node i to node j is described by the Fourier law

$$Q_{ij} = K_{ij}\Delta T \tag{4.3}$$

K_{ij} is the *linear conductance* [16] of the mean of the thermal exchange and its explicit expression depends on the geometry of the discretised system.

In particular, the relation

$$Q_{ij} = \frac{k(T)A_{ij}}{\Delta x}\Delta T \tag{4.4}$$

holds in the case of one-dimensional heat conduction through a slab of surface A_{ij} (orthogonal with respect to the heat flux) and length Δx, with $\Delta T = T_i - T_j$ and $k(T)$ thermal conductivity (representing the amount of heat that passes per unit time through a unit area with a unit temperature gradient). The value of the linear conductance K_{ij} can be estimated through the lumped parameters method.

Radiative heat transfer between two nodes i and j is described by the following law:

$$Q_{ij} = \sigma A_i \frac{T_i^4 - T_j^4}{\frac{1-\varepsilon_i}{\varepsilon_i} + \frac{1}{F_{ij}} + \frac{1-\varepsilon_j}{\varepsilon_j}\frac{A_i}{A_j}} \tag{4.5}$$

where σ is the Stefan-Boltzmann constant, the ε and the A are, respectively, the emissivities and the areas of the nodes i and j involved in the heat exchange. F_{ij} is the *view factor* of the system made of the two nodes [25]. The law could be written in an analogous way as

$$Q_{ij} = \sigma A_i F_{ij} F_e \left(T_i^4 - T_j^4\right) \tag{4.6}$$

with

$$F_e = \left(\frac{1-\varepsilon_i}{\varepsilon_i} \cdot F_{ij} + 1 + \frac{1-\varepsilon_j}{\varepsilon_j} \cdot \frac{A_i}{A_j} \cdot F_{ij}\right)^{-1} \tag{4.7}$$

This leads to

$$Q_{ij} = R_{ij} \left(T_i^4 - T_j^4\right) \tag{4.8}$$

by introducing the term

$$R_{ij} = \sigma A_i F_{ij} F_e \tag{4.9}$$

that is the *radiative conductance*, which, for complex systems, is typically evaluated by dedicated modules of thermal modelling software.

4.1.3 Thermal model of Strip's calibrator cryostat

In the case of Strip's calibrator cryostat, the main heat exchanges (radiative and conductive) between the different subsystems, considered to build a preliminary simple thermal model, are represented in Fig. 4.3.

The description of the heat exchanges starts from the more external shells of the calibrator cryostat and continues with the inner ones.

The external surface of the cryostat exchanges heat with the external environment, thus, the walls have physical temperature $T \approx 300$ K.

On the window aperture side of the cryostat, the radiative heat load is exchanged with an IR filter, if present (1). On the other sides of the calibrator, heat is exchanged radiatively between the walls at ambient temperature and the radiative shield (2). By means of the reflective MLI covering the shield, the radiative heat load towards the inner subsystems of the cryostat is limited. The shield is in thermal contact with the cryocooler I stage (3).

In the innermost part or the system, the thermal radiation coming from the IR filter reaches the arrays of pyramids (4). In order to let the arrays reach the required

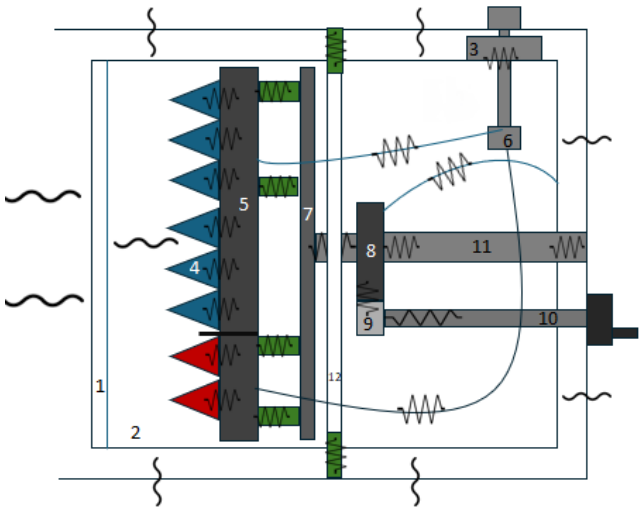

Figure 4.3: Visual sketch of the radiative and conductive heat exchanges concerning the calibrator cryostat and its subsystems.

temperature range an efficient thermal link is set between the pyramids and the cryocooler second stage (that is the colder one). So, the pyramids are in good thermal contact with the $\frac{1}{4}$ and $\frac{3}{4}$ slices (5) through Aluminium plates, that are then connected to the II stage of the cryocooler (6) through Cu thermal straps.

The two slices are allowed to rotate by connecting them to the rotating wheel (7) through fibreglass spacers (thermally insulating).

The wheel can rotate through the connection with the central back gear (8), that is connected to a smaller gear (9), mounted on a rotating shaft (10). Conductive heat exchange between these subsystems is limited by a proper choice of materials and by reducing the contact surfaces. All this structure is carried on by a mechanical connection with the cryostat walls (11) and by fixed rays (12).

A thermal strap has also been added connecting the central back gear with the radiative shield (thermalised with the cryocooler I stage) in order to reduce the temperature of the gear by using the I stage as heat sink.

Preliminary conductor values were estimated for all the thermal exchanges and power balance was evaluted. This allowed to have a prediction on the temperature distribution expected in the different cryostat configurations. The equilibrium temperature of the rotating wheel was determined by considering the balance between the heat load from the exterior and the heat exchanged with the cold head second stage, resulting in $T \approx 65$ K. This was used as reference for the equilibrium temperatures of the slices. They must have temperature lower with respect to that of the rotating wheel (through proper insulation), and as close as possible to that of the cold head second stage (through thermal straps). For this reason, the linear conductance with the cold head must be dominant with respect to that with respect to the external environment.

Given the complexity of the structure of the calibrator cryostat, uncertainties in the model results have to be progressively reduced by correlating them to experimental test data.

4.2 Calibrator cryostat dry runs (I phase)

In the runs described in this section the setup is as described in the previous chapter, with the exception of the IR filter, still not integrated in the cryostat in the early phases.

Table 4.1: Dry runs performed.

Dry run	**Setup**
First	Stand-alone calibrator cryostat + Al plate
Second	Strip (cooled) + calibrator cryostat
Third	Strip (T_{amb}) + calibrator cryostat (cooled)
Fourth	Stand-alone calibrator cryostat + window

In each run the same vacuum bench was used: a dry (oil-free) Scroll vacuum pump and a turbomolecular vacuum pump.

The mechanical cryocooler used is a Leybold CoolPower 5/100 (lifting 5 W at 20 K II stage and 100W at 80 K I stage), based on a Gifford McMahon thermodynamic cycle.

4.2.1 The 1st dry run (January 2025)

The first run took place in January 2025.

The experimental setup consisted of the stand-alone calibrator cryostat, with an Aluminium plate mounted in front of its window aperture.

In order to monitor the internal pressure of the calibrator cryostat, a pressure sensor is mounted at the top of the cryostat and connected to the monitor of the turbomolecular vacuum pump. While, to monitor the temperatures, eight thermometers are positioned on different subsystems, listed in Table 4.2, and connected to a Lakeshore monitor. Then, the measured temperatures are acquired through the GPIB interface, making it possible to communicate in real time and record the data in the acquisition system.

The procedure followed to put the system under thermal-vacuum condition is described in A.

The curves describing the cool-down, obtained thanks to the temperature sensors, are reported in Fig. 4.5

The values of the temperatures of the different subsystems, when the stationary condition (T constant in time) was reached, are reported in Table 4.2.

The performances of the calibrator cryostat, both in terms of P and T (especially for the slices, that will be in contact with the calibrating units), met the requirements.

Figure 4.4: *Left panel*: Photograph taken at the Cryowaves Laboratory, showing the experimental setup of the first run. The Al plate in front of the calibrator cryostat is visible. The termometers deployed in the cryostat are connected to the monitor by the flat cables on the left. The flex lines are visible on the right, connecting the cryocooler cold head to its compressor. *Right panel*: Rear view of the cryostat, with the Scroll vacuum pump connected to the instrument through a Tombac line, by the valve of the turbo molecular pump, visible in the photograph too.

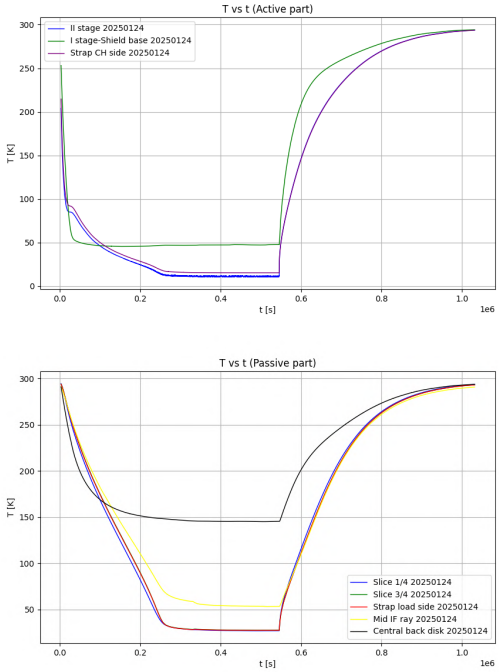

Figure 4.5: *Upper panel*: Plot of the T as a function of t for the active parts of the calibrator cryostat. *Lower panel*: Analogous plot but for the passive components.

For this reason, the values obtained in this first dry run will often be used as reference for the subsequent dry runs.

Table 4.2: T at equilibrium measured by the different thermometers.

Component	**Temperature [K]**
CH II stage	11.46
CH I stage-Shield Base	47.61
Strap CH side	15.38
Slice 1/4	26.83
Slice 3/4	27.50
Strap load side	27.26
Mid IF ray	53.13
Central back disk	145.34

4.2.2 The 2nd dry run (February 2025)

Once verified that the calibrator stand alone achieved the expected thermal-vacuum performance, the nominal configuration of the global system had to be tested.

Therefore, the calibrator cryostat has been mounted in front of Strip's focal plane.

In order to attach the calibrator in front of Strip, it has been necessary to demount the Al plate.

Thus, the procedure to open a cryostat in A has been followed.

Then, the calibrator has been attached in front of Strip's UHMWPE window. The window was dried from possible moisture to avoid damaging the scroll pump. It must be underlined that Strip was already in cryogenic condition. The experimental setup is shown in Fig. 4.6

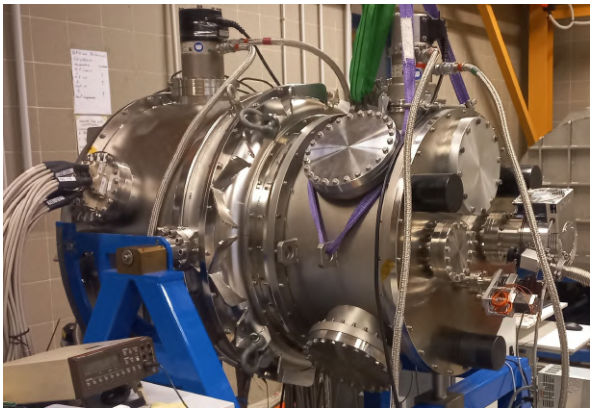

Figure 4.6: Photograph showing the calibrator cryostat (on the right) mounted in front of Strip (on the left) at the Cryowaves laboratory at INAF-OAS.

Subsequently, the vacuum pumping procedure took place. In this run the decrease of the pressure due to the action of the Scroll pump was slower with respect to the one expected.

On the other hand, the pressure of Strip was still the nominal one, meaning that the two system are mutually insulated, as wanted.

The most obvious explanation was that the presence of an air leak in the connection between the two instruments prevented the pressure inside the calibrator cryostat from reaching the desired vacuum level.

Nevertheless, the calibrator cryostat has been cooled down, to estimate how much a higher pressure could affect the temperature distribution. The results of the cool down are showed in Fig. 4.7, while the temperatures reached at the stationary condition are reported in Table 4.3

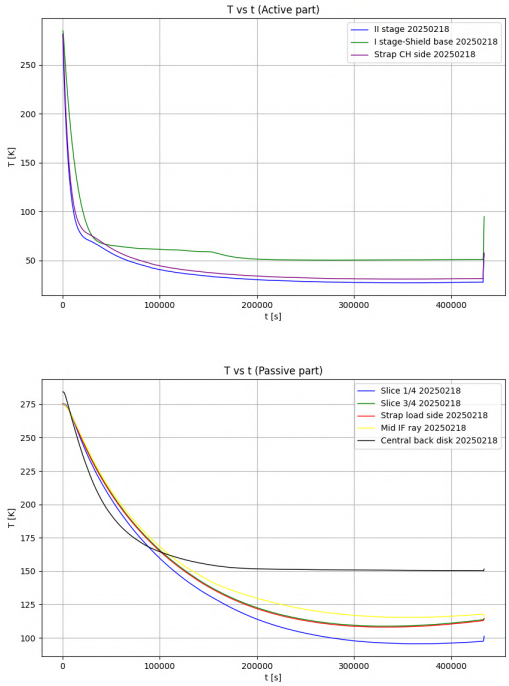

Figure 4.7: *Upper panel*: Plot of the T as a function of t for the active parts of the calibrator cryostat in dry run 2. *Lower panel*: Analogous plot but for the passive components.

Table 4.3: T at equilibrium measured by the different thermometers.

Component	**Temperature [K]**
CH II stage	27.7
CH I stage-Shield Base	50.79
Strap CH side	31.44
Slice 1/4	97.38
Slice 3/4	113.6
Strap load side	112.86
Mid IF ray	117.73
Central back disk	150.4

By comparing the temperatures after the establishment of the stationarity, it can be seen that the T of the second dry run are systematically higher with respect to those of the first dry run. This effect is particularly noticeable in the temperatures of the two slices, that were the subsystems specifically targeted for cooling (being the hosting structure of the calibrating units).

The air leak has been searched in the flanges near the connection between Strip and its calibrator. A particularly cold area had been found and, subsequently, interpreted as due to a leakage of cold air. Investigating the possible causes from a design perspective, it was realised that the mounting used worked in the case of the flange (plate) employed during the first dry run, but could not function when coupled to Strip, requiring a second O-ring, as foreseen in the design phase, to ensure a proper sealing of the calibrator from the external environment. The following sketch sums up the situation, with the position of the O-rings and a possible path for the air, connecting the interior and the exterior and, thus, preventing the desired vacuum condition from being achieved.

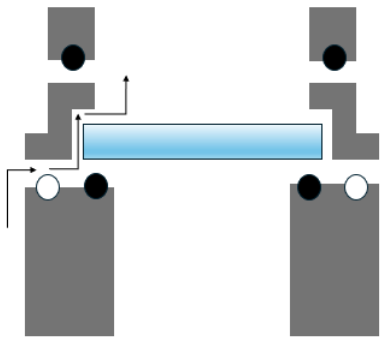

Figure 4.8: Sketch representing the connection between Strip (bottom) and the calibrator (top) with Strip's window between them. The missing O-ring (the external one, white) and the one present (the internal one, black) are represented with the dots. A possible air leakage path is represented with arrows.

The calibrator cryostat had been detached from Strip, in order to add the missing internal O-ring.

4.2.3 The 3rd dry run (March 2025)

After having de-integrated the calibrator from Strip, it was confirmed that the external O-ring was actually missing (as can be seen from Fig. 4.9).

The internal O-ring had been removed, in order to clean it, and then a thin layer of high-vacuum grease was applied to ensure a better sealing.

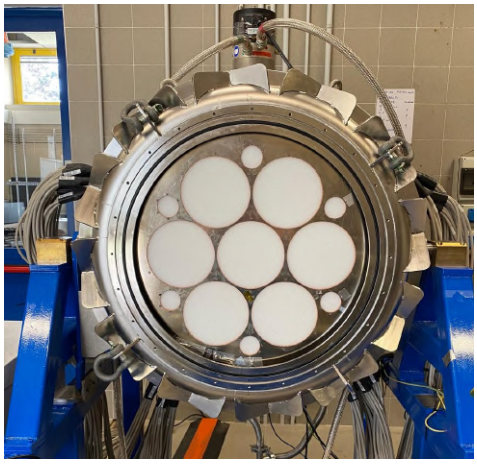

Figure 4.9: Photograph showing Strip, with its IR filters holder Aluminium plate and, in the flange, the internal O-ring and the empty external O-ring groove.

The same treatment was applied to the new external O-ring. Before putting in place both the O-rings, the two respective grooves in the flange of Strip had been cleaned with isopropyl alcohol.

Then, Strip and its calibrator were integrated, to test if, now that the O-ring thought to be insulating the calibrator from the exterior has been added, the P inside the calibrator could reach the satisfactory values.

At first, we did not pump over Strip to test the insulation of the two instrument, both from the outside and from the other one, by only pumping over the calibrator.

Due to the fact that it was already planned to replace the cold head with a new one: the total time needed for cooling-down and warming-up would therefore not have been in line with the project timeline.

In the third run the calibrator cryostat (and especially the slices) are facing the interior of Strip at $\approx$ 300 K. This is going to introduce a much large radiative heat load onto the slices of the calibrator than in the previous runs, thus, this third dry run can be considered as a test of the calibrator cryostat performances in almost the worst operating condition.

In particular, the actual worst condition is the one with the calibrating units mounted and facing 300 K, because (as said in the previous chapter) they behave as perfect absorbers, and their expected temperature is higher than that of the slices, due to the radiative coupling and the contact resistance with the slices. This time, after the usual vacuum pumping process over the calibrator, the result is $P \approx 4 \cdot 10^{-6}$ mbar while inside Strip $P \approx P_{amb}$. Thus, it can be concluded that the air leakage was really due to the missing O-ring (so, now, the calibrator is insulated from the exterior too) and that the calibrator cryostat is actually insulated from Strip (as wanted).

Then, the calibrator cryostat has been cooled down.

The plots showing the behaviour of the temperatures during the cooldown are reported in Fig. 4.10

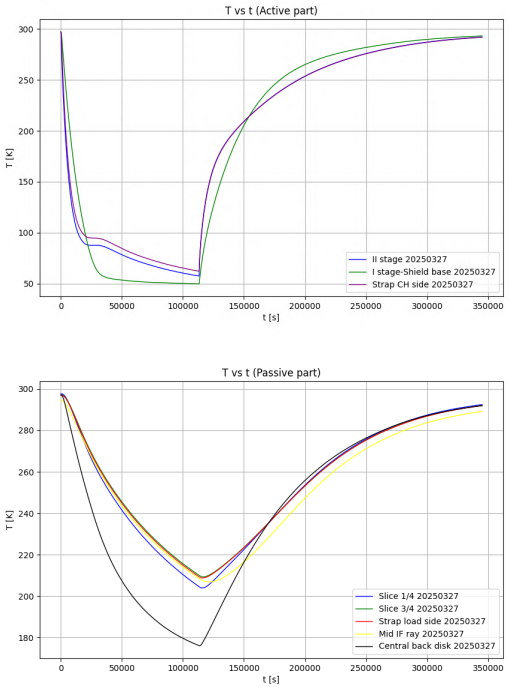

Figure 4.10: *Upper panel*: Plot of the T as a function of t for the active parts of the calibrator cryostat in dry run 3. *Lower panel*: Analogous plot but for the passive components.

The cooldown was interrupted before reaching the thermal plateau (stationary condition), to replace the cold head of Strip with the new one. For this reason, in the following table the values reported are the minimum temperatures, just reached by the different components of the calibrator cryostat.

Table 4.4: Minimum T measured by the different thermometers.

Component	**Temperature [K]**
CH II stage	57.42
CH I stage-Shield Base	49.8
Strap CH side	62.15
Slice 1/4	204.61
Slice 3/4	210.12
Strap load side	209.4
Mid IF ray	208.61
Central back disk	176.18

It is interesting to make a comparison of the T behaviours between the second run (that of February) and the third one (March) 4.11.

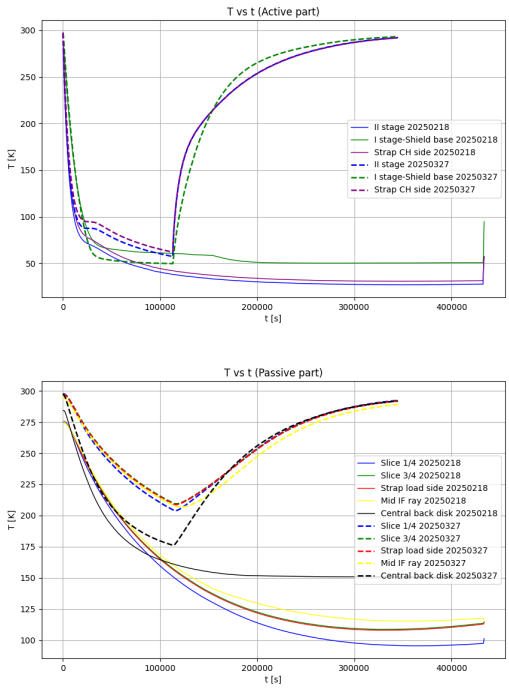

Figure 4.11: *Upper panel*: Plot showing a comparison of the T as a function of t for the active parts of the calibrator cryostat between run 2 (February, continuous line) and run 3 (March, dashed line). *Lower panel*: Analogous plot but for the passive components.

In the third run the cool down is less effective with respect to the one of the second run, in fact the curves are going down with a lower rate and the minimum temperatures reached (even though it had not been possible to get to the equilibrium temperatures in the third run) are much higher. These comments hold for both the active and passive

components of the calibrator cryostat. The underlying reason for this discrepancy can be found in the different radiative heat load onto the slices, thus, onto the Cold Head through the thermal straps. In fact, this is due to the difference in the temperature that the slices of the calibrator cryostat are seeing (the interior of Strip at cryogenic T in one case, Strip at ambient T in the other). For this reason, the performances of the calibrator cryostat in the third run are worse in terms of minimum temperatures reached.

Eventually, a further test was performed, to test the strength performance of Strip's UHMWPE window, when exposed to high vacuum on both sides: the test consists in pumping the vacuum even over Strip's cryostat. The result is that, even when $P < 10^{-4}$ mbar on both sides, the window does not undergo deformations that could compromise the seal of the vacuum.

At the end of the third run, following the usual procedure, the calibrator cryostat has been de-integrated from Strip, to open Strip and replace the cold head.

4.2.4 The 4$^{\text{th}}$ dry run (April 2025)

The 4th run was dedicated to verifying the stand-alone calibrator — when facing a 300 K environment, representative of the 3rd run condition, considered as the worst case.

For this reason, it has been chosen to couple the calibrator with an UHMWPE window, to make it look the external environment at 300 K.

It must be specified that the window, unlike the one mounted on Strip, has no grooves. They are useful to limit reflections at microwave,but, for our purpose (IR filtering and vacuum seal), the flat one is enough . In addition, the nominal one would mechanically interfere with the IR filter, due to the grooves.

In this way, it is possible to continue the analysis started in the third run.

The aim of this fourth run is also to verify if there could be a good coupling between the calibrator cryostat and the window. In fact, as previously outlined, a window had always been mounted on Strip, and not directly on the calibrator cryostat.

The window has been mounted onto the calibrator cryostat, using both O-rings in order to ensure a better sealing.

The usual procedure (see A) has been performed in order to put the calibrator cryostat under thermal vacuum.

The pressure values are the expected ones, therefore, this serves as a verification of the fact that the window is well-matched with the calibrator.

The following plots show the temperature curves resulting from the cooling process.

Figure 4.12: Photographs showing a front view of the calibrator cryostat. The slices, visible before the coupling with the flat (without grooves) window (*Left*) and then the UHMWPE window mounted (*Right*).

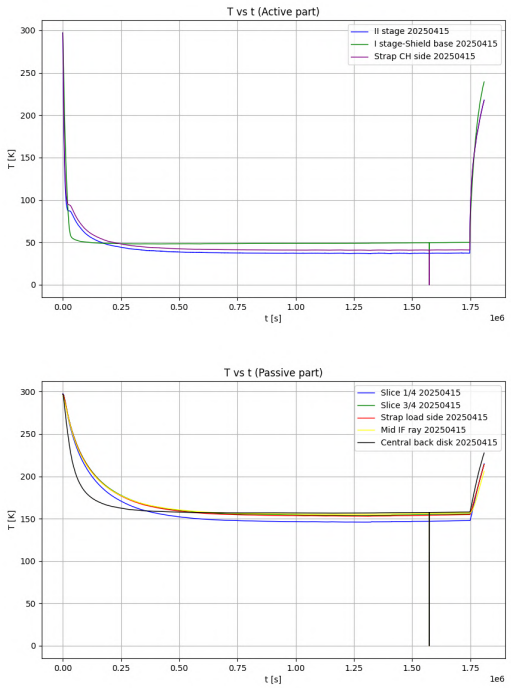

Figure 4.13: *Upper panel*: Plot of the T as a function of t for the active parts of the calibrator cryostat in dry run 4. *Lower panel*: Analogous plot but for the passive components.

The temperatures reached at the stationary condition are reported in Table 4.5

Table 4.5: T at equilibrium measured by the different thermometers.

Component	**Temperature [K]**
CH II stage	37.31
CH I stage-Shield Base	49.93
Strap CH side	41.07
Slice 1/4	147.68
Slice 3/4	155.54
Strap load side	154.74
Mid IF ray	156.81
Central back disk	157.77

Then, it is particularly important to compare the T curves and the lowest temperature reached by each sensor with those of the other runs. Specifically, for what concerns the comparison between dry runs 4 and 1, the curves are superposed in Fig. 4.14

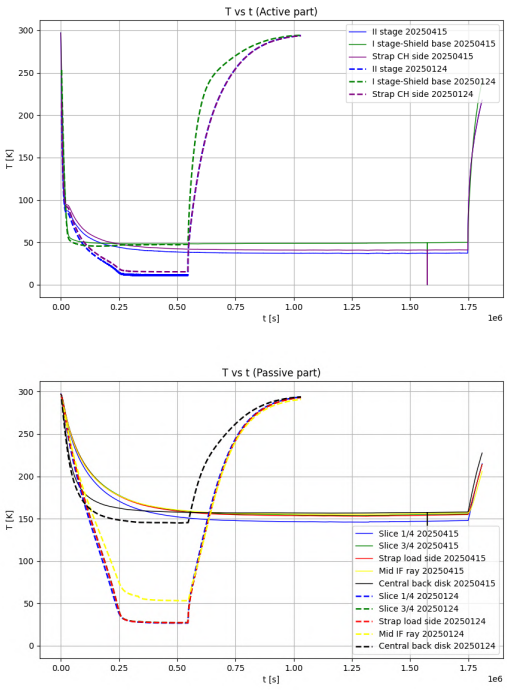

Figure 4.14: *Upper panel*: Plot showing a comparison of the T as a function of t for the active parts of the calibrator cryostat between run 1 (January, dashed line) and run 4 (April, continuous line). *Lower panel*: Analogous plot but for the passive components.

As it can be seen from the plots, for both the active and passive parts, the cooling in the fourth dry run is less effective and slower. This is due to the fact that now the

calibrator is receiving (through the window) radiation from the hot environment at 300 K, while in the first dry run the Aluminium plate, due to its poor emissivity, reflected back the internal temperature of the calibrator. Therefore, now the radiative heat load onto the slice (and then onto the Cold Head) is much larger.

In Fig. 4.15 the comparison between the T *vs* t plots of runs 3 and 4 are shown.

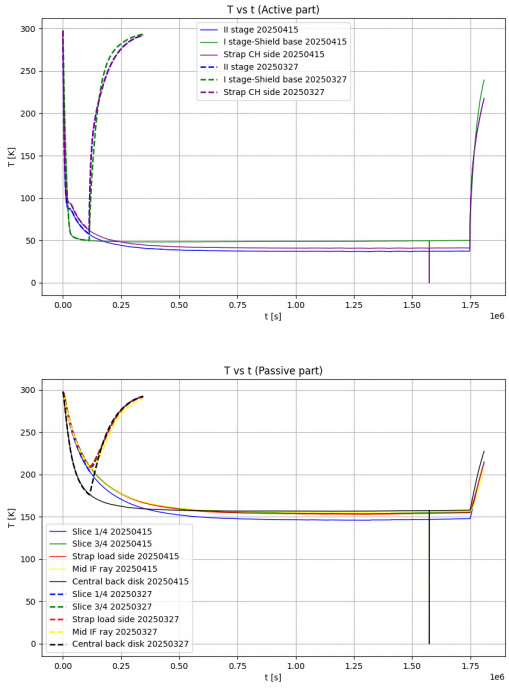

Figure 4.15: *Upper panel*: Plot showing a comparison of the T as a function of t for the active parts of the calibrator cryostat between run 3 (March, dashed line) and run 4 (April, continuous line). *Lower panel*: Analogous plot but for the passive components.

This comparison is of crucial importance, being the fourth run a replication of the third, yet with a different experimental setup. The aim was to see how the T curves would have behaved if there would have been more time to continue the third run. The fact that the initial parts of the curves of the two runs of Fig. 4.15 are almost perfectly superposed is exactly the wanted result. In fact this is a confirmation of the fact that the situation of dry run 3 has been well-replicated by means of the window.

In order to try to reach lower values of T, especially for the slices, the plan was to insert an IR filter at the calibrator input, in front of the slices. In analogy with the filters of Strip, it must mechanically fit the radiative shield as best as possible, to thermalize (the radiative shield is connected to the Cold Head I stage). In this way, it should be able to shield the slices from the hot radiation at 300 K from the outside and re-emit thermal radiation, towards the interior, at a lower temperature (its physical

temperature).

4.3 Calibrator thermal analysis and modelling

At the end of this first phase of dry runs, test data were used to better estimate some specific conductors.

Moreover, a thermal model in ThermXL has been developed, in order to simulate the expected radial temperature gradient of the IR filter (that will be mounted on the calibrator), and estimate the temperatures of the slices.

4.3.1 Thermal analysis

The thermal analysis has been carried out by considering the equilibrium temperatures obtained in the first and in the fourth dry run. The main difference between the two runs is the radiative interface at the window aperture: metal lid in the first run, UWHM-PE window in the second case.

One outcome of the analysis is also a prediction of the optimal temperature of the IR filter, which is going to be installed in the calibrator cryostat.

We focused on the subset of thermal network (represented in Fig. 4.16). Specifically, the only thermal exchanges considered have been:

- the **radiative ones**, between the window/plate and the two slices
- the **conductive ones**, between the two slices and the cold head II stage, connected through Cu thermal straps.

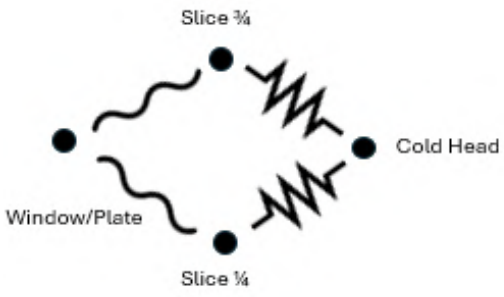

Figure 4.16: The sketch shows the network of volumes considered, where the black dots represent the nodal pints, the wave-like lines represent the radiative exchange and the zigzag lines represent the linear conduction.

The values of the total dissipated power onto the slices (thus, onto the Cold Head, being in thermal contact through the thermal straps) is estimated by considering the

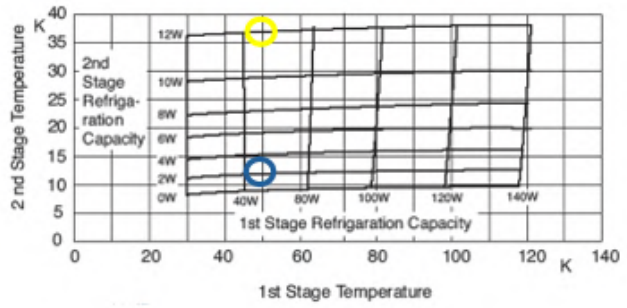

Figure 4.17: The diagram in phase space shows the temperatures of the two stages of the Cold Head on the axis. Then, from the grid in the diagram, is possible to evaluate the corresponding dissipated power on the two stages. The blue circle represents the P dissipated in the run of January (the first) while the yellow is corresponding to the run of April (the fourth).

following diagram showing the typical heat load map of the cold head model used, Leybold CoolPower 5/100 (lifting 5 W at 20 K 2nd stage and 100W at 80 K 1st stage).

The values of the dissipated power are reported there:

- $\dot{Q}_{1,\frac{1}{4}+\frac{3}{4}} = 2$ W
- $\dot{Q}_{4,\frac{1}{4}+\frac{3}{4}} = 12.2$ W

where the subscript 1 (4) indicates the first (fourth) run and the $\frac{1}{4} + \frac{3}{4}$ is used so as to underline that the values are the total power dissipated (so the sum of the one dissipated onto the slices singularly). The value of $\dot{Q}_{\frac{1}{4}+\frac{3}{4}}$ is higher in the fourth run, since the radiative heat load is much larger, as expected.

The first part of the thermal analysis describes the radiative heat exchange between the window and the slices.

The two assumptions used to treat this part of the thermal analysis are:

- At first order, all the heat load transmitted, through copper straps, to the Cold Head is due to the radiative heat exchange between the window and the slices
- Radiative conductances χ of the slices $\frac{1}{4}$ and $\frac{3}{4}$ are in a 3:1 ratio (due to geometrical reasons), so $\chi_{\frac{3}{4}} = 3\chi_{\frac{1}{4}}$.

Therefore, it is possible to write $\dot{Q}_{\frac{1}{4}+\frac{3}{4}} = \dot{Q}_{\frac{1}{4}} + \dot{Q}_{\frac{3}{4}}$ with $\dot{Q}_{\frac{1}{4}} = \chi \cdot \Delta T^4$ and $\dot{Q}_{\frac{3}{4}} = 3\chi \cdot \Delta T^4$. Then, Eq. 4.2 can be written specifically for the simplified model and for the two runs as

$$\begin{cases} \dot{Q}_{1,\frac{1}{4}+\frac{3}{4}} = \chi_{\frac{1}{4}}(T^4_{plate} - T^4_{1,\frac{1}{4}}) + 3\chi_{\frac{1}{4}}(T^4_{plate} - T^4_{1,\frac{3}{4}}) \\ \dot{Q}_{4,\frac{1}{4}+\frac{3}{4}} = \chi_{\frac{1}{4}}(T^4_{amb} - T^4_{4,\frac{1}{4}}) + 3\chi_{\frac{1}{4}}(T^4_{amb} - T^4_{4,\frac{3}{4}}) \end{cases}$$

having considered $\chi_{\frac{1}{4}}$ equal in both the dry runs, being linked to the geometry of the system and to the emissivity properties of the slices.

It is possible to get the **radiative conductance** $\chi_{\frac{1}{4}}$ from the second equation of the system, by the knowledge of the T_{amb} and $\dot{Q}_{4,\frac{1}{4}+\frac{3}{4}}$ (from Fig. 4.17). The result is $\chi_{\frac{1}{4}} = 4.46 \cdot 10^{-10} \ \frac{\mathrm{W}}{\mathrm{m}^2}$. By inserting this result in the first equation of the system, the equivalent temperature of the Aluminium plate used in the first run can be obtained, leading to $T_{plate} = 183$ K.

The value of $\chi_{\frac{1}{4}}$ has also been independently estimated with a direct calculation by assuming $F_{12} = 1$ at first order and $F_e \approx \varepsilon \approx 0.1$ for the Aluminium slices, getting $\chi_{\frac{1}{4}} = 8.6 \cdot 10^{-10} \ \frac{\mathrm{W}}{\mathrm{m}^2}$, so a comparable value with the former one. The Al plate is reflective, meaning that it is partly reflecting the temperature of the interior of the cryostat itself, rather than emitting at his physical T (that is approximately 300 K). Therefore, the Al plate (characterised by low emissivity and at $T \approx 300$ K) can be equivalently imagined as a good emitter ($\varepsilon \approx 1$) but at a temperature $T < 300$ K. So this representation is similar to that of the IR filter mounted, that would be colder than T_{amb} being mounted on the radiative shield, thermalised with the Cold Head I stage and with high emissivity, so it would mainly emit radiation at his physical temperature. Since the results of the first run have been compliant to what needed, we can conclude that a filter with $T_{filter} \approx 180$ K would allow optimal results for the other internal temperatures.

From the radiative transfer equation of the fourth run, it is possible to get the value of F_{12}, that is $F_{12} = 1.37$ (different from the first order approximation). This value only depends on geometrical factors, thus, it must be the same in both the runs. By plugging $F_{12} = 1.37$ in the first equation of the system, $T_{plate} = 185$ K has been obtained, so a confirmation of the reliability of the previous result.

The individual values of the **dissipated power** for the two slices can be obtained for the fourth run, by considering the just found view factor, as follows

$$\dot{Q}_{4,\frac{1}{4}} = \sigma\varepsilon F_{12}\frac{1}{4}A(T^4_{amb} - T^4_{4,\frac{1}{4}}) \tag{4.10}$$

$$\dot{Q}_{4,\frac{3}{4}} = \sigma\varepsilon F_{12}\frac{3}{4}A(T^4_{amb} - T^4_{4,\frac{3}{4}}) \tag{4.11}$$

giving $\dot{Q}_{4,\frac{1}{4}} = 2.96$ W and $\dot{Q}_{4,\frac{3}{4}} = 8.77$ W. The sum of these two values gives the total power dissipated onto the Cold Head, that results in agreement with the 12 W obtained from Fig. 4.17. By means of the first hypothesis made at the beginning of the thermal analysis, all the power exchanged radiatively between the window (or plate)

and the slices is then exchanged conductively between the slices and the Cold Head II stage (through the Cu thermal straps).

The **linear conductances** for the fourth run can be computed by using the same dissipated powers obtained from the radiative heat exchange study. Thus, using the Fourier law Eq. 4.3: $K_{4,\frac{1}{4}} = 0.027$ and $K_{4,\frac{3}{4}} = 0.074$. The ratio $\alpha = \frac{K_{\frac{3}{4}}}{K_{\frac{1}{4}}} = 2.76$ is compatible with the actual setup, in fact the thermal straps connected to the two slices are mainly differing in their number (material, length and section are similar), then, the ratio must depend mainly on it. The straps from the $\frac{3}{4}$ slice are indeed twice as much as the ones from the $\frac{1}{4}$.

As further verification of the thermal description of the calibrator cryostat main subsystems we evaluated the dissipated powers on the two slices individually for the first run, as just done for the fourth one. Computing the $\dot{Q}$ values for the first run from the linear conduction equations, by assuming the same linear conductances of the fourth run, would give a wrong result. In fact the sum of the two would not be the expected 2 W, but a value lower by 1.22: $\frac{\dot{Q}_{graph}}{\dot{Q}_{estimated}} = 1.22$.

This difference is due to the fact that copper thermal conductivity strongly depends on the temperature, in this cryogenic range, see Fig. 4.18. The values of T of the straps in the two runs differ of ≈ 30 K, and it can be seen from the graph that the expected respective thermal conductivities are indeed different.

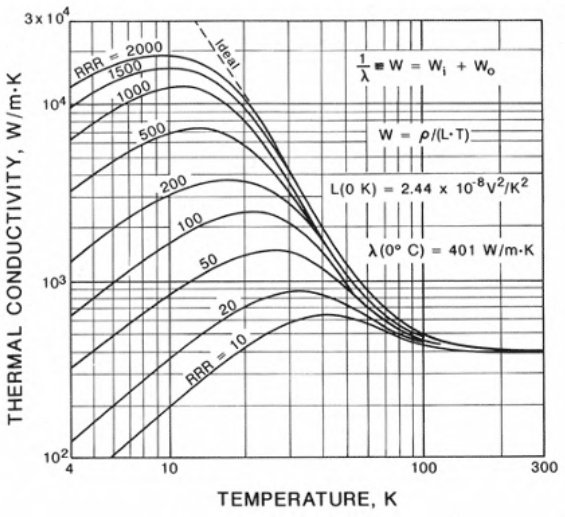

Figure 4.18: The graph shows the behaviour of thermal conductivity for different purities of Copper (RRR parameter). The values of thermal conductivity may be very different, especially before and after the peak.

A factor 1.22 is then considered compliant to the range of conductivity variation between the runs.

$$\begin{cases} \dot{Q}_{1,\frac{1}{4}+\frac{3}{4}} = 1.22 \cdot K_{\frac{1}{4}} \Delta T_{\frac{1}{4},CH} + 1.22\alpha K_{\frac{1}{4}} \Delta T_{\frac{3}{4},CH} \\ \dot{Q}_{4,\frac{1}{4}+\frac{3}{4}} = K_{\frac{1}{4}} \Delta T_{\frac{1}{4},CH} + \alpha K_{\frac{1}{4}} \Delta T_{\frac{3}{4},CH} \end{cases}$$

In this way the total dissipated power of the first run $\dot{Q}_{1,\frac{1}{4}+\frac{3}{4}}$ gives a value close to the 2 W expected.

Within the still large uncertainties related to this preliminary experimental assessment, we then could verify some of the main properties characterizing and driving the thermal behaviour of the cryostat.

4.3.2 Filter thermal model

In the previous chapter we estimated the value of T_{filter} that would ensure a satisfactory temperature distributioninside the calibrator cryostat. The filter is expected to show radial temperature gradients. To describe the filter, I developed a dedicated thermal model.

The dominant effects that are determining the filter temperatures are:

- Radiative heat load coming from the environment
- Thermal contact with the radiative shield (thermalised with the cryocooler I stage).

The scheme is the following: the radiation is coming through the window (seen as a uniform plane at ≈ 300 K) towards the filter. Thus, we must consider that:

- the window and filter exchange heat radiatively
- the heat flows conductively over the filter, radially from the center to the radiative shield

In this case, it is necessary to calculate the linear conductance K between concentric rings. Starting from the expression of the Fourier law in the case of cylindrical geometry with height h (and assuming an average value for the thermal conductivity $k(r) = \bar{k}$)

$$d\dot{Q} = \bar{k} A(r) \frac{dT}{dr} \tag{4.12}$$

where A is the area of the surface orthogonal to the direction of the heat flux, thus, in the case of heat exchange between different rings, $A(r) = 2\pi r h$. In stationary regime, the heat flux $\dot{Q}$ is constant with the radial direction, therefore it is possible to write

$$dT = \frac{\dot{Q}}{\bar{k} 2\pi h} \frac{dr}{r} \tag{4.13}$$

By integrating between two temperatures and the corresponding radial distances from the centre of the system

$$\int_{T_1}^{T_2} dT = \frac{\dot{Q}}{\bar{k} 2\pi h} \int_{r_1}^{r_2} \frac{1}{r} dr \tag{4.14}$$

That leads to the result

$$\dot{Q} = \bar{k} \frac{2\pi h}{\ln \frac{r_2}{r_1}} \Delta T = K_{12} \Delta T \tag{4.15}$$

where K_{12} is the linear conductance between two rings at distances r_1 and r_2 from the centre. For each ring the heat exchanges to consider are:

- the power received radiatively from the window
- the one exchanged conductively with the inner and the outer adjacent annuli
- the radiative one between the filter and the slices (that are exchanging heat conductively with the II stage through Cu thermal straps, see Fig. 4.19).

Thus, for the i-th node of the IR filter:

$$F_e F_v \sigma A_i (T_{window}^4 - T_i^4) = \bar{k} \frac{2\pi h}{\ln \frac{r_i}{r_{i-1}}} (T_{i-1} - T_i) + \bar{k} \frac{2\pi h}{\ln \frac{r_{i+1}}{r_i}} (T_i - T_{i+1}) \tag{4.16}$$

Eventually, this first part of the system is described by a system of five equation (one for each nodal point of the filter, divided in five annuli) of the fourth order in T_i, that are the quantities of interest.

The **thermal lumped parameter modelling** has been conducted using the ThermXL software. The system is represented by 10 nodal points, and the final aim is to determine the equilibrium temperatures along the radial dimension of the filter and, consequently, the T reached by the slices. The filter has been divided into 5 concentric annuli, each with its nodal point, and then there are:

- the Cold Head's first and second stages
- the $\frac{1}{4}$ and $\frac{3}{4}$ slices
- the window

each with its T at stationary regime.

Specifically, focusing on the modelling of the filter (see Fig. 4.20), the 5 nodal points have been considered positioned on the circle passing from the centre of each annulus and, thus, there are localised the respective temperatures. The total radius

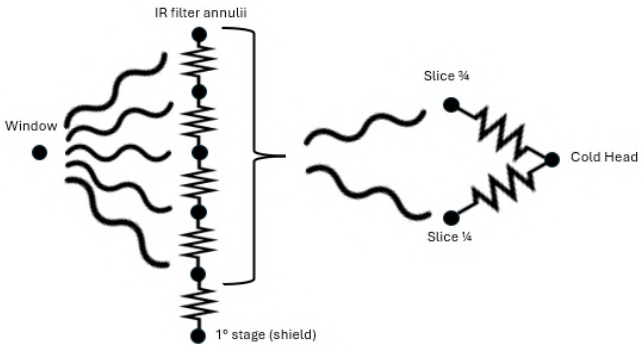

Figure 4.19: The sketch shows the network of volumes considered in the configuration with the IR filter, where the black dots represent the nodal points, the undulating lines represent the radiative exchange and the zigzag lines represent the linear conduction.

R_{tot} of the filter is equal to r_5 and corresponds to the thermal contact between the filter and the radiative shield (in contact with the I stage). In particular, $R_{tot} = 284$ mm. For the i-th annulus, $r_i = i \cdot r_1$ with $r_1 = \frac{R_{tot}}{5} = 56.8$ mm.

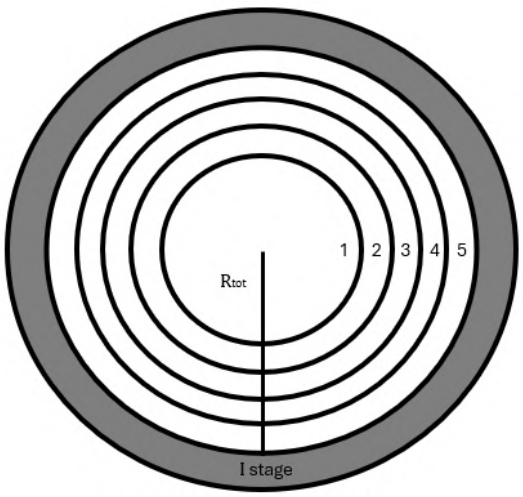

Figure 4.20: The sketch represents in a schematic way how the IR filter has been modelled, in order to analyse it. The 5 nodal points describing it have been considered as positioned at the centre of each annuli.

The surfaces of the annuli and the radiative and linear conductances needs to be computed and provided to the software. In output, the searched temperatures will be provided, together with the values of the power exchanged $\dot{Q}$

As boundary conditions, the results from the first run have been used (such as the

temperatures of the radiative shield and of the Cold Head II stage). For T_{window}, 300 K has been used.

The inputs required for the filter model are listed in the table, which summarises the Teflon properties [18]:

Table 4.6: Teflon IR filter properties needed for the thermal model.

Property	**Value**
Th. Conductivity $\bar{k}$ (65 K)	0.22 W/(m·K)
Density ϱ	2200 kg/(m^3)
Specific heat c_p (100 K)	350 J/(kg·K)
Height h	6 mm
Radius R_{tot}	284 mm

The computation of the surfaces of the annuli, using the general relation $A_i = \pi r_i^2 - \pi r_{i-1}^2$ gave the following results:

Table 4.7: Computation of the surfaces.

Surface	**Value [m^2]**
A_1	0.0101
A_2	0.0304
A_3	0.0507
A_4	0.0709
A_5	0.0913

In order to compute the heat capacities C, it has been necessary to previously evaluate the masses of the annuli , with $m_i = \varrho A_i h$. Then $C_i = c_p m_i$, giving the results summed up in the following table.

Table 4.8: Computation of the heat capacities.

Heat capacity	**Value [J/K]**
C_1	46.55
C_2	140.35
C_3	234.15
C_4	327.6
C_5	421.8

Linear conductances between the annuli have been computer by referring to the previously obtained relation (Eq. 4.15), so that $K_{i,i+1} = \bar{k}\frac{2\pi h}{\ln \frac{r_{i+1}-\Delta r}{r_i - \Delta r}}$. The $\Delta r = \frac{r_1}{2}$

has been used because the nodal points, as already underlined, have been taken at the centre of each annulus. The results are reported in the following table.

Table 4.9: Computation of the filter linear conductances.

Linear conductances	**Value [W/K]**
$K_{1,2}$	0.00755
$K_{2,3}$	0.016
$K_{3,4}$	0.0246
$K_{4,5}$	0.033
$K_{5,Istage}$	0.0787

For what concerns the linear conductances of the exchange between the slices and the Cold Head II stage, the values referred in the thermal analysis as the ones corrected for the different k have been used: $K_{\frac{1}{4}} = 0.032$ and $K_{\frac{3}{4}} = 0.072$.

Then, the radiative conductances have been treated. Starting from the radiative exchange between window and filter, $Fv = 1$ has been assumed, considering the window as a uniform plane at $T \approx 300$ K illuminating the filter and $\varepsilon_{filter} = 1$ as worst case. The result is that the χ terms are numerically equal to the surfaces of the annuli of Table 4.7.

The radiative conductances of the exchange between filter and slices have been computed for each slice by considering the product $\chi = \varepsilon_{slice} A_{slice} A_{annulus}$, in fact, in this case, the approximation of infinite uniform and homogeneous plane in front of the slices cannot be used, due to the temperature radiative gradient along the radial direction of the filter. Therefore, it has been assumed that the view factor F_v for each exchange is proportional to the product of the surfaces involved. In particular, $\varepsilon_{slice} = 0.1$ (for Aluminium) and $\varepsilon_{filter} = 1$ (as already reported). The results of the radiative conductances are indicated in the following table.

Table 4.10: Computation of the filter-slices radiative conductances.

Radiative conductances	**Value [W/K^4]**
$\chi_{\frac{1}{4},r_1}$	0.000642
$\chi_{\frac{1}{4},r_2}$	0.00193
$\chi_{\frac{1}{4},r_3}$	0.00321
$\chi_{\frac{1}{4},r_4}$	0.00449
$\chi_{\frac{1}{4},r_5}$	0.00578
$\chi_{\frac{3}{4},r_1}$	0.00193
$\chi_{\frac{3}{4},r_2}$	0.00578
$\chi_{\frac{3}{4},r_3}$	0.00963
$\chi_{\frac{3}{4},r_4}$	0.0135
$\chi_{\frac{3}{4},r_5}$	0.0173

The result of the steady state simulation are that the filter shows a temperature gradient with $T \approx 290$ K in each annuli, thus, far from the average $T = 183$ K, estimated to be enough to obtain the optimal results of the first run for the other internal subsystems, in particular the slices. Their equilibrium temperature result to be, therefore, higher with respect to that of the first run.

In order to make the model more accurate, $\varepsilon_{slices} = 1$ has been used. In fact, in the nominal configuration, the calibrating units would be mounted onto the slices and would efficiently absorb the radiation. As previously pointed out, they must behave as quasi-perfect blackbody. The result is that they would absorb much more the heat coming from the outside with respect to the slices alone, resulting in a larger $\dot{Q}$ and a higher equilibrium temperature. The results of this more realistic simulation are listed in the following table:

Table 4.11: Resulting temperatures from the model for the filter annuli and the slices with $\varepsilon_{slices} = 1$.

Temperatures	**Value [K]**
$T_{\frac{1}{4}}$	145
$T_{\frac{3}{4}}$	173
T_{r_1}	278
T_{r_2}	278
T_{r_3}	278
T_{r_4}	276
T_{r_5}	247

The large temperature of the filter (and, consequently, of the slices) is mainly due to the reduced thickness of the IR filter, which limits the efficient heat transfer across it. It is easy to verify that the thermal radial gradient would be, indeed, characterised by lower T at each r from the centre of the filter if it was thicker. On the other hand, the filter cannot be too thick in order to limit its impact in the signal travelling from the calibrating source to the Strip polarimeters.

4.4 Calibrator cryostat dry runs (II phase)

The penultimate dry run has been performed with the IR filter mounted, in order to experimentally verify the results obtained from the thermal model. Then a dry run with two absorbing panels (Eccosorb CR-110 and TK-RAM), has been done, in order to find the most suitable one, to then proceed with the actual calibration.

4.4.1 The 5th dry run (May 2025) and comparison with the thermal model

The external flange of Strip's calibrator has been demounted, in order to install the IR filter (shown in Fig. 4.22) and, then, to verify the results obtained from the thermal model.

The thermometer on the load side of the thermal strap has been attached to the centre of the IR filter (by using Kapton tape and a thin film of Apiezon grease to improve the thermal contact) to monitor its temperature. The diode on the strap (load side) has been chosen to be removed because the T measured was always ≈ 1 K colder than the slices themselves.

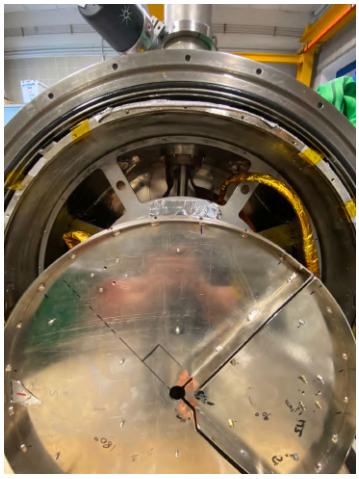

Figure 4.21: The photograph shows the slices demounted from the rotative wheel. The Si diode thermometer has been passed from the interior towards the exterior through the hole and, then, attached to the IR filter.

The calibrator cryostat has been closed and then put under thermal-vacuum (A).

Figure 4.22: The photograph shows the IR filter before mounting it onto Strip's calibrator and attached to the thermometer.

The plots showing the behaviour of the different T as function of time have been obtained.

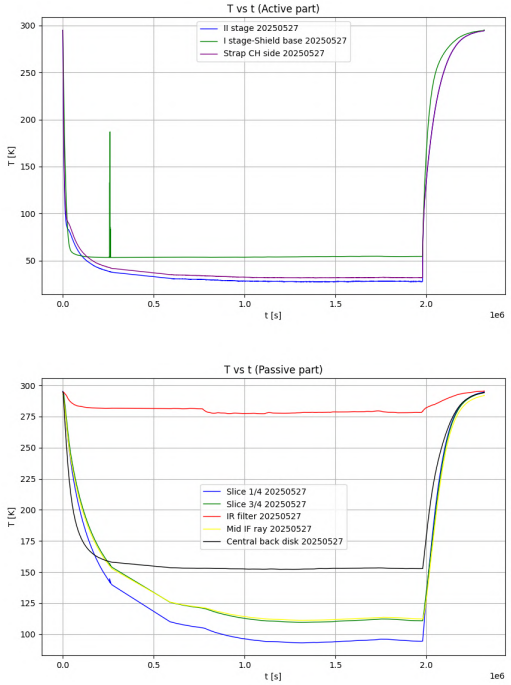

Figure 4.23: *Upper panel*: Plot of the T as a function of t for the active parts of the calibrator cryostat in dry run 5. *Lower panel*: Analogous plot but for the passive components. At odds with the previous plots, this time there is also the thermometer describing the behaviour of the temperature as a function of time for the filter.

In the first part of the plot showing the passive components, it is possible to see that the temperature reached by the IR filter are similar to that predicted by the simulation (close to $\approx$ 280 K). There is still a downward trend, but not too much accentuated, due to the inefficient heat conduction.

It can be noted that all the other subsystems (with the exception of the radiative shield) are colder with respect to the run of April (the fourth dry run), because of the IR filter being $\approx$ 10 K colder than T_{amb}, thus, reducing the radiative heat load onto the internal subsystem. The radiative shield (so the I stage of the Cold Head too) is hotter than in the fourth run due to the fact that now it is attached to the filter, therefore, now it has a larger heat load.

A first comparison between the data and the thermal model described in the previous section has been performed (still regarding the first part of the plots). In fact, in order to obtain from the model the same temperatures of the slices ($T_{\frac{1}{4}}$ and $T_{\frac{3}{4}}$) observed from the data, $\varepsilon_{slices} = 0.7$ is needed. In fact, the commonly used $\varepsilon = 0.1$,

used for the slices, is realistic for highly polished Aluminium, but it increases for oxidized Aluminium [11]. In this way the simulation gives as results: $T_{\frac{1}{4}} = 133$ K and $T_{\frac{3}{4}} = 157$ K for the slices, while for the filter there is an average temperature for the central annuli of ≈ 279 K and of ≈ 245 K for the outer one. Therefore, the likeliest value for the emissivity of the slices has been obtained in order to have the same results from model and from data. Furthermore, the results from the simulation for the power dissipated onto the Cold Head stages ($\dot{Q}$) are in agreement with the ones taken from Fig. 4.17, by knowing from the data the temperatures reached by the two stages.

After a few days, the stationary condition has been reached, therefore the respective temperatures reached by the different subsystems are reported in the following table.

Table 4.12: T at equilibrium measured by the different thermometers with no Al plate.

Component	**Temperature [K]**
CH II stage	29.98
CH I stage-Shield Base	53.65
Strap CH side	34.08
Slice 1/4	105.25
Slice 3/4	121.08
IR filter	281.35
Mid IF ray	121.55
Central back disk	152.97

Given the fact that the IR filter does not reach the desired equilibrium temperatures when the calibrator is facing the hot environment, it has been decided to test its behaviour when facing something colder, when, in terms of acquisition time, $t \approx 7.5{\cdot}10^5$ (referring to Fig. 4.23).

In fact, in the nominal condition, the calibrator receives its own cold radiation reflected by the Strip's filter holder, as well as the emission from the filter holder and the IR filters, both weighted by the transmission of the Strip vacuum window. Therefore, this situation could be simulated by an Al plate put in front of the calibrator.

The effect of the Al plate has started to be evident after almost a day, when a new descending trend has been seen in the curves. The most evident effect is on the IR filter, being the one directly exposed to the exterior, and its temperature lowers of $\approx 3-4$ K, reaching $T_{filter} = 277.34$ K. The subsequent effect on the slices is that they are still descending in T.

In particular, a comparison with the thermal model has been performed when $T_{\frac{1}{4}} = 94.3$ K and $T_{\frac{3}{4}} = 111.3$ K. The presence of the Al plate in front of the calibrator is implemented in the simulation by considering a $T_{window} \approx 290$ K. It is important to check the effect of the Aluminium plate and IR filter in terms of the dissipated power

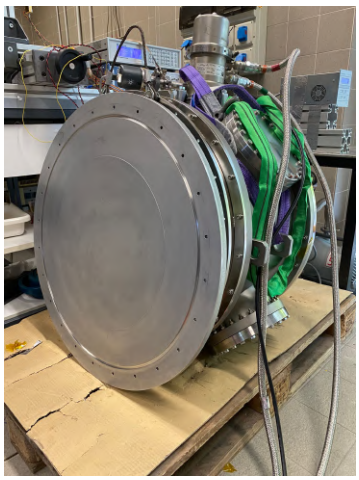

Figure 4.24: The photograph shows the Aluminium plate lying in front of Strip's calibrator.

onto the Cold Head, with respect to the previous runs with only the window at 300 K in front of the slices. In the run of April, the temperature of the Cold Head II stage was ≈ 37 K and that of the I stage was ≈ 50 K, which means having 12.2 W dissipated onto the II stage (from the dissipated power diagram in Fig. 4.17). Now, in the fifth run, with IR filter and Al plate, the T of the II stage is ≈ 28 K and that of the I stage is ≈ 53 K, so the dissipated power onto the II stage is less than 10 W. This means that the current experimental setup enabled to reduce the power dissipated onto the II stage of 2 W. Moreover, the dissipated power onto the slices from the filter by radiative heat transfer has been computed, in order to verify the result of the 10 W dissipated onto the II stage (as usual, it has been assumed that all the heat exchanged radiatively between filter and slices is then transferred by linear conduction through the Cu thermal straps to the Cold Head). The filter is not all homogeneous in temperature, but the annuli from 1 to 4 are mostly isothermal and, in addition, the thermometer of the filter had been attached in its central part, thus, the assumption of almost isothermal filter (from $r = 0$ to $r = r_4$) at $T = T_{filter}$ is reasonable.

The result obtained is ≈ 9 W, thus compatible with what found from Fig. 4.17.

Starting from $\approx 10^6$ s, an increasing trend has been detected in the curves. The I stage of the Cold Head is the first one that started heating, then, as a result, also the filter, followed by the slices. In order to try to find a reasonable explanation, at first the dissipated powers $\dot{Q}$ between the window and the filter have been computed. The temperature of the window has been directly measured with a thermometer and the value obtained is of 280 K (in fact a thin condensation layer was detected on the window, due to the reflective action of the Al plate towards the window itself).

The estimation of the dissipated power has been done by dividing the run in three different phases, in order to have values of $\dot{Q}$ as reference: before putting the Al plate ($T_{filter} = 281$ K and $T_{window} = 295$ K), at equilibrium with the Al plate ($T_{filter} = 277$ K) and the value during the just detected reheating ($T_{filter} = 279$ K). The values $\varepsilon_{filter} = 1$ and $F_v = 1$ (filter seen as a homogeneous disc) have been used.

The results are reported in the following table.

Table 4.13: $\dot{Q}$ computed during three phases of the fifth run: before putting the Al plate (I phase), at equilibrium reached with Al plate (II phase) and at the current maximum during the evident reheating (III phase).

Phase	**Dissipated power $\dot{Q}$ [W]**
I phase	18.59
II phase	3.11
III phase	1.88

The discrepancy between the result of phase I and the last two gives evidence of the positive effect of the Al plate in terms of radiative heat load onto the internal subsystems of Strip's calibrator. The difference between the values computed for phase II and III (≈ 1 W) is not negligible. It can be concluded that the observed reheating can be due to a larger radiative heat exchange between window and filter (and then the effect is then propagating to the other inner subsystems, as already said). There are a few possible explanations, such as that the effect is due to hotter days, so a larger T_{amb}, or due to the aforementioned thin layer of condensation on the window. Thus, the Al plate reflects back to the calibrator more the thermal emission from water (at a higher T than $T_{calibrator}$) than the internal T of the calibrator, causing the reheating. Eventually, it can be seen from the dissipated power diagram in Fig. 4.17, that in a region on the left there is a regime where the dissipated power on the I stage increases if the one on the II stage decreases, so this may be another valid explanation.

After a few days, the increasing temperature trend became oscillatory, therefore, the Al plate has been removed. After ≈ 5 hours, the temperature of the filter increased by 1 K. Then, following the usual procedure, the calibrator has been opened again.

To conclude, the configuration with the filter (even if the situation improves when facing something at $T < T_{amb}$ as would be in the nominal condition) does not meet the required standards for the Strip experiment, thus the possible solution may be to use the calibrator in front of Strip but without the window between them (that would, then, be characterized in a stand-alone configuration). The negative aspect of this possibility is that the calibration would not take place in the nominal operational conditions of Strip.

4.4.2 The 6th dry run (July 2025)

The actual calibrating units need to be mounted onto the slices. It has been chosen to consider two different samples of calibrating units (having the geometry of an array of pyramids), made of two different materials: a panel of Eccosorb CR-110 and one of TK-RAM (with pyramids having a lower height). In this way it is possible to study the different behaviour of the two panels during a dry run and, then, being able to decide which one is more suitable for the calibration of Strip.

In particular, the Eccosorb CR-110 is a castable epoxy absorber made of two components: a resin matrix and a curing agent (a substance added to the resin to make it harden and turn into a solid, due to the resulting crosslinking of its epoxy groups), mixed in a specific ratio, that depends on the case. In addition, there are finely dispersed metallic particles within the epoxy matrix, that dissipate electromagnetic energy through dielectric and magnetic losses, enhance electrical properties (for optimized absorption in specific frequency bands) and improve thermal stability (by increasing thermal conductivity to dissipate the heat generated during EM energy absorption).

For what concerns the TK-RAM (*Tessellating TeraHertz Radar-Absorbing Material*), it is a conductive plastic loaded with high absorption capability.

For both the tiles, the pyramidal shape of the surface helps the reduction of the reflections and the dissipation of the incoming radiation too (due to the fact that Black-Bodies are perfect absorbers).

The temperature behaviour of the two samples during the subsequent dry run cooldown must be monitored by two different thermometers mounted on the respective calibrating unit, thus, it has been necessary to open the calibrator from the front flange (so as to access the slices and attach the two samples of calibrating units) and from the small lateral flange (in order to add the two new Cernox thermometers).

The **lateral flange** has been opened, as shown in Fig. 4.25.

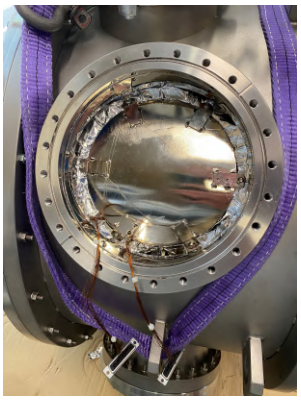

Figure 4.25: The photograph shows the lateral side of the calibrator, with the cables that were attached to the internal part of the flange seeable at the bottom of the image.

The **metallic plate** at the centre of the image must be removed too in order to access the interior of the calibrator cryostat, shown in Fig. 4.26.

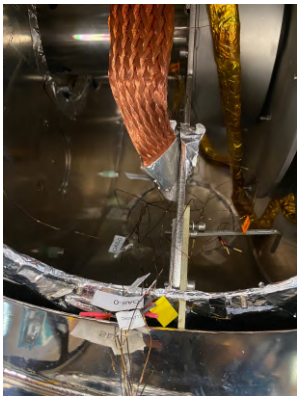

Figure 4.26: The photograph shows the interior of the calibrator cryostat. The metal mounting bracket for two 25-pin male connectors is visible near the fixed rays.

In order to implement the two additional Cernox thermometers (for the two samples of pyramids arrays), an additional male-to-female connector jumper wired with manganin leads was needed, because the other two were already fully occupied by the other thermometers. Moreover, it has been necessary to substitute the current metal mounting bracket for the connectors, in order to have room for the new one. After having done that, the two new thermometers have been added.

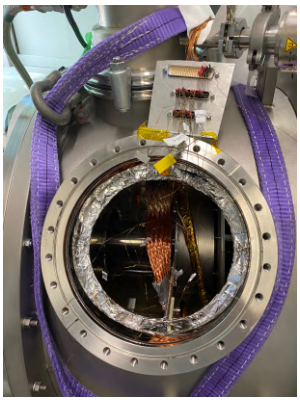

Figure 4.27: The photograph shows the thermometers (each with its own four wires) connected to the male-to-female connector jumper.

In Fig. 4.27 the final configuration of the thermometers' wires (I_+, V_+, I_- and V_- for each thermometer) attached onto the two 25-pin male-to-female connector jumper and the additional 50-one, mounted onto the metal mounting bracket, can be seen.

Then, the **metal mounting bracket** has been attached onto the calibrator cryostat and, before closing the lateral flange, the correct functioning of the thermometers has been verified (Fig. 4.28).

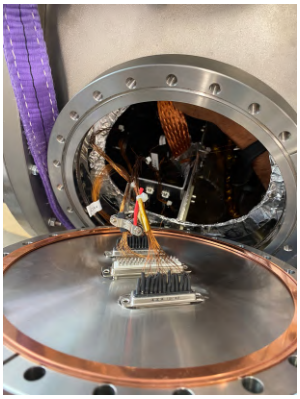

Figure 4.28: The photograph shows the thermometers directly connected to the external flange, in order to check the pin-to-pin connections made. The metal mounting bracket had already been attached to the callibrator cryostat.

After that, the lateral flange of the calibrator has been closed properly.

For what concerns the attachment of the two new thermometers to the calibrating unit samples, at first the $\frac{1}{4}$ and the $\frac{3}{4}$ slices have been demounted. Then, the two Cernox thermometers have been routed through the hole at centre of the slices plate and the pyramids have been attached onto the Al plates, anchored to the slices (Fig. 4.29).

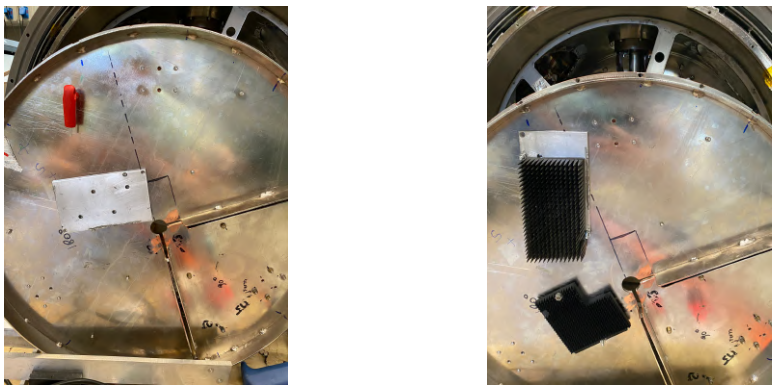

Figure 4.29: Photographs showing an Al plates mounted onto the slices (*left*) and then the two samples of calibrating units in the 'final' setup (*Right*).

Eventually, the thermometers have been attached onto the pyramids (Fig. 4.30), putting also a thin film of Apiezon grease (in order to obtain a better thermal contact between the thermometers and the respective pyramid).

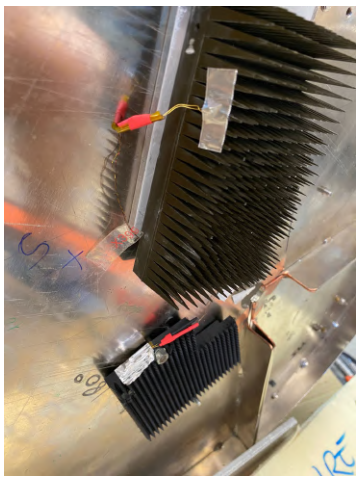

Figure 4.30: The photograph shows the thermometers attached to the pyramids by means of tape.

The usual procedure has been followed so as to put Strip's calibrator under thermal vacuum condition.

The curves showing the behaviour of T vs t are reported in Fig. 4.31.

The temperatures of the different subsystems once the stationary condidtion has been reached are outlined in the following table.

Table 4.14: Equilibrium T measured by the different thermometers.

Component	**Temperature [K]**
CH II stage	41.34
CH I stage-Shield Base	51.70
Strap CH side	45.66
Slice 1/4	154.63
Slice 3/4	175.86
IR filter	274.02
Mid IF ray	172.75
Central back disk	165.16
CR-Panel	243.17
PL-Panel	227.78

Thus, the sample of pyramids array made of the conductive plastic (PL-Panel in the Table) is able to reach a temperature ≈ 15 K lower with respect to that made of Eccosorb CR-110 (CR-Panel in the Table).

However, in order to decide which material to choose, the procurement time must be taken into account too.

In any case, the results, as previously outlined, are far from the desired $\approx 25 - 40$ K, expected for the calibration of Strip and the only solution to meet the requirements may be to attach the calibrator in front of Strip but without the 'hot' window between them.

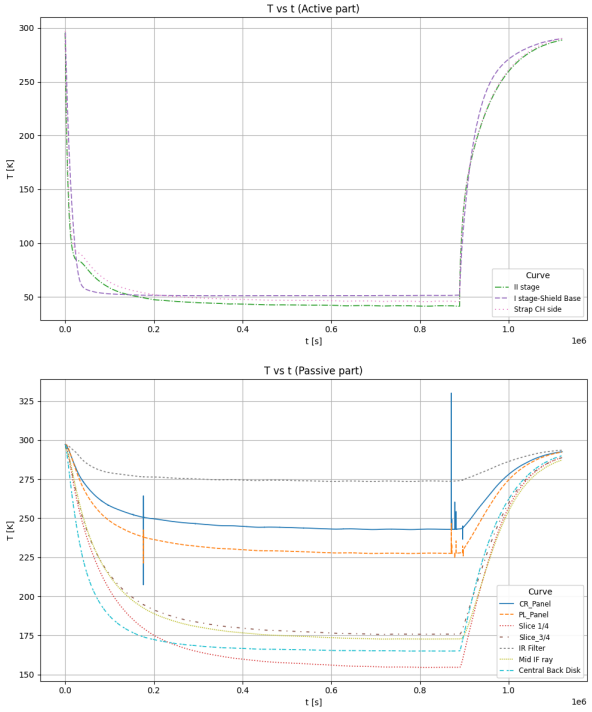

Figure 4.31: *Upper panel*: Plot of the T as a function of t for the active parts of the calibrator cryostat in dry run 6. *Lower panel*: Analogous plot but for the passive components. In this dry run there are also the calibrating units samples, so their curves are labelled as CR-panel for the pyramids in Eccosorb CR-110 and PL-panel for the ones in conductive plastic.

Chapter 5

Integrated system verification

The calibrator cryostat must be tested integrated with Strip, both at cryogenic temperatures: at this stage, we have already positively verified the calibrator cryostat's thermal-vacuum performances both in the stand-alone configurations (both with and without integrated emissive elements) and mounted in front of Strip (that was at $T \approx T_{amb}$).

The objective is to study how the two system, when integrated, mutually influence one another from a thermal point of view. For instance, the temperature distribution of the different subsystems of the calibrator are expected to behave in a different way when facing Strip cooled down, with respect to when facing the Aluminium plate or the external environment (through the UHMW-PE window).

In particular, the two systems, when both cooled down, should each benefit from the other's presence. In fact, a system that sees a colder environment is subjected to a reduced radiative heat load, therefore, the dissipated power onto its cooling system is lower and the refrigeration is more effective.

However, it must be underlined that, during this test, Strip was not in his nominal condition: in fact the polarimeters in the focal plane were not attached through thermal straps to the Copper H-Frame (in thermal contact with the cold head second stage). In fact, due to the replacement of the problematic cryocooler with the new one, an acceptance test of its cold head had been performed, to verify that its actual performances are coherent with the nominal ones. For this reason it was necessary to limit the conductive heat load onto the cold head.

Therefore, a subsequent test with the calibrator mounted in front of Strip in its nominal condition will be performed subsequently.

In this chapter, a preliminary characterisation of the system with two absorbing panels, installed in the calibrator and both candidates for the final setup, is discussed. The goal is to determine their equilibrium temperature under the current radiative and conductive conditions, and to assess the polarimeters' response when viewing either the absorber panels or a reflective surface (partially inside a cavity). The aim is to check the internal consistency of the results and make a first estimate of the polarimeters'

noise temperature under thermal and biasing conditions significantly different from the nominal ones.

In order to apply the Y-factor method (described in 3.1), a reference blackbody signal, at two different temperature at least, is needed. For this reason, several cycles of cooling-downs and warm-ups of Strip's calibrator have been planned, to then compute the noise temperature T_{noise} of the four detectors for each of the polarimeters connected and biased (they are eight, for thermal reasons: to avoid overloading the cold head, especially the second stage, through the harness during the dry run).

5.1 System integration and thermal verification

After the assembly of the vacuum bench (showed in Fig. 5.1, together with the two pressure sensors) the usual procedure was followed, in order to evacuate Strip's cryostat.

The Scroll pump (dry-oil free) pumped for two days before reaching $P \approx 4 \cdot 10^{-2}$ mbar, after cycle of gas ballast on-off (in order to speed up pump down by repeatedly cleaning the pump by alternating the ballast setting). After three days with the turbomolecular pump evacuating Strip's cryostat, the internal pressure was $P \approx 4 \cdot 10^{-4}$ mbar, therefore the cooler was turned on. After one day $P \approx 4.5 \cdot 10^{-7}$ mbar.

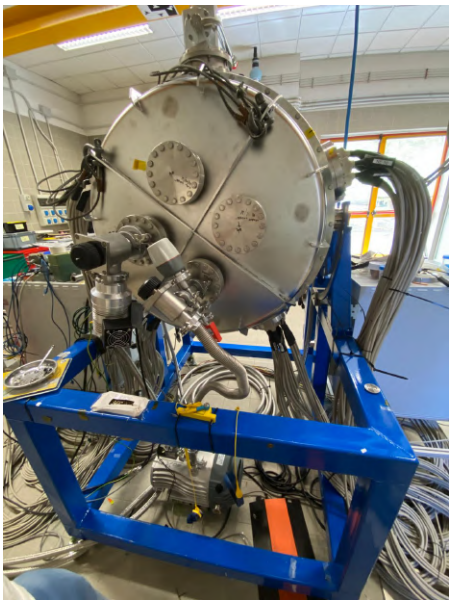

Figure 5.1: The photograph shows the rear of Strip and its assembled vacuum bench.

The results of the cooling down are showed in Fig. 5.4 for $t < 8 \cdot 10^5$ s. The most relevant sensors measured the following temperatures at equilibrium:

- $T_{IIstage} = 4.8K$
- $T_{Istage} = 99.6K$
- $T_{FocalPlane} = 185K$

In particular, it is important to monitor the temperatures reached by the Strip H-Frame (see Fig. 5.2) that will be used to thermally connect the focal plane to the cold head II stage (by means of thermal straps). Two thermometers are used: one placed on the Cu structure near the II stage, the other one in the bottom left corner, in order to study the temperature gradient along the structure.

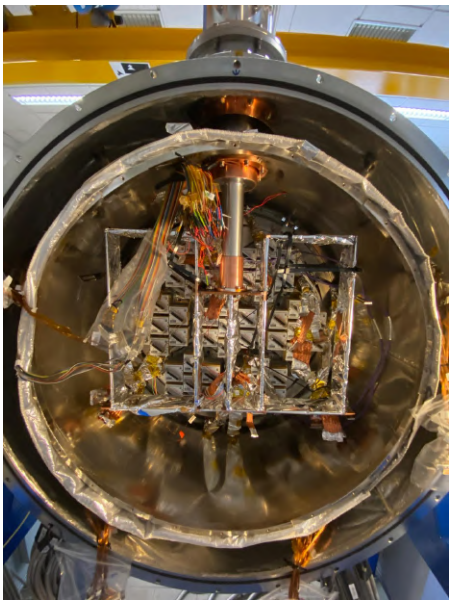

Figure 5.2: The photograph shows Strip's Copper structure, needed to thermalise the focal plane with the cold head II stage.

The resulting behaviour of the cooling of the Strip H-Frame are reported in 5.5 for $t < 8 \cdot 10^5$ s.

The values of the equilibrium temperature reached by the part of the Strip H-Frame near the cold head II stage and the one in the bottom left corner are respectively:

- $T_{near\ CH} = 4.9K$
- $T_{far\ from\ CH} = 11K$

The internal pressure was of $P = 1.9 \cdot 10^{-7}$ mbar after the cool down.

The temperatures in stationary condition reached by the subsystems of Strip are compliant with expected values, therefore the calibrator cryostat was integrated in front of Strip's focal plane.

The calibrator cryostat was moved towards Strip's cryostat by using a transpallet, lifted with an overhead travelling crane and then mounted onto Strip's frontal flange.

The usual procedure, outlined in A was followed in order to put the calibrator cryostat under vacuum. After a weekend, the internal pressure of the calibrator cryostat was $P = 4.6 \cdot 10^{-2}$ mbar, as pre-vacuum. Then the turbomolecular pump was activated bringing the internal pressure to $P \approx 5 \cdot 10^{-5}$ mbar after one hour.

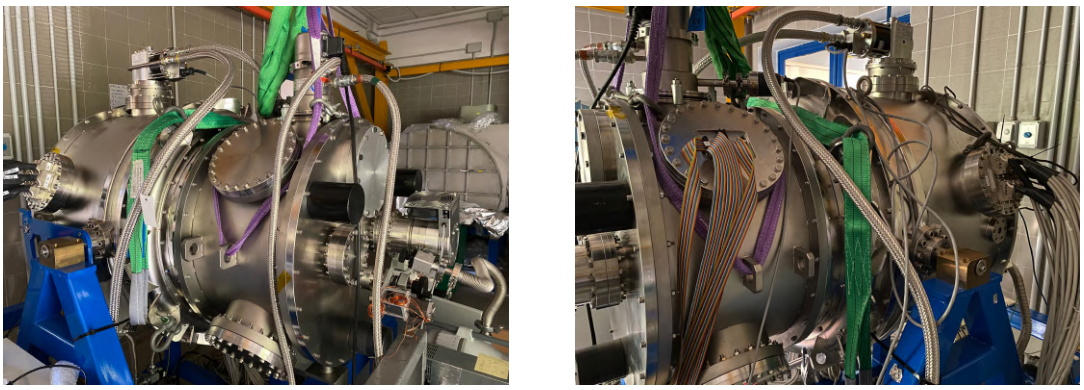

Figure 5.3: Photographs taken at the INAF-OAS Cryowaves Laboratory, showing Strip and its calibrator cryostat integrated, seen from the lateral views.

The integration of the two systems had an almost immediate effect onto the internal temperatures of each other. This effect visible in the behaviour of Strip's subsystems, reported in the plots in Fig. 5.4 and in Fig. 5.5, and also in the internal temperatures of the calibrator, reported in Table 5.1

Table 5.1: Equilibrium T measured by the different thermometers of the calibrator.

Component	**Temperature [K]**
CH II stage	284.5
CH I stage-Shield Base	286.8
Strap CH side	285.8
Slice 1/4	279.5
Slice 3/4	278.2
IR filter	254.6
Mid IF ray	279.2
Central back disk	287.1
CR-Panel	272.2
PL-Panel	272.4

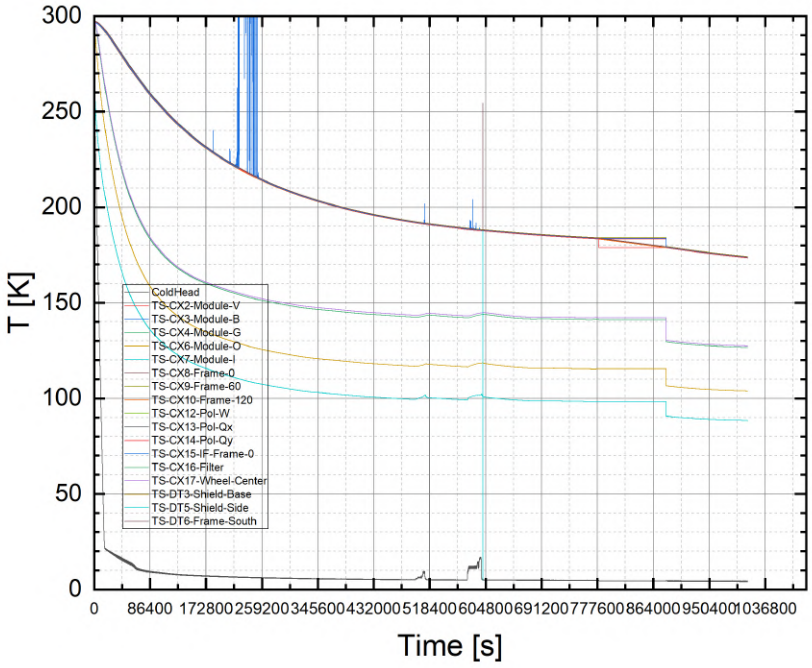

Figure 5.4: Plot showing the behaviour of the temperatures of the Strip's cryostat internal subsystems. After $t < 8 \cdot 10^5$ s, the effect of the calibrator cryostat mounted in front of Strip's focal plane is visible.

As expected, there is a sudden decrease in the temperatures of the internal parts of Strip, and also of the internal temperatures of the calibrator, that, even if not cooled down, are lower with respect to the *dry run* when the calibrator was facing the environment at $T \approx 295$ K (*dry run* 6) through the microwave transparent vacuum window.

This may be interpreted as the fact that the two systems are influencing each other, as expected.

After one day, the two absorbing panels are ≈ 23K colder than the room ambient temperature and hotter than the IR filter. In fact, the temperature of the IR filter ($T \approx 254.6$ K) is a proof of the influence that facing the cold cryostat of Strip has on the internal part of the calibrator cryostat. Due to the radiative heat exchange with the cold window, the filter is cooled down by the window itself, while the slices are exchanging heat radiatively with the IR filter, lowering their temperatures.

The system has been modelled in a simple way in order to characterise the heat exchanges between the window and the IR filter, and between the slices and the cold head, to better understand the system from a thermal point of view.

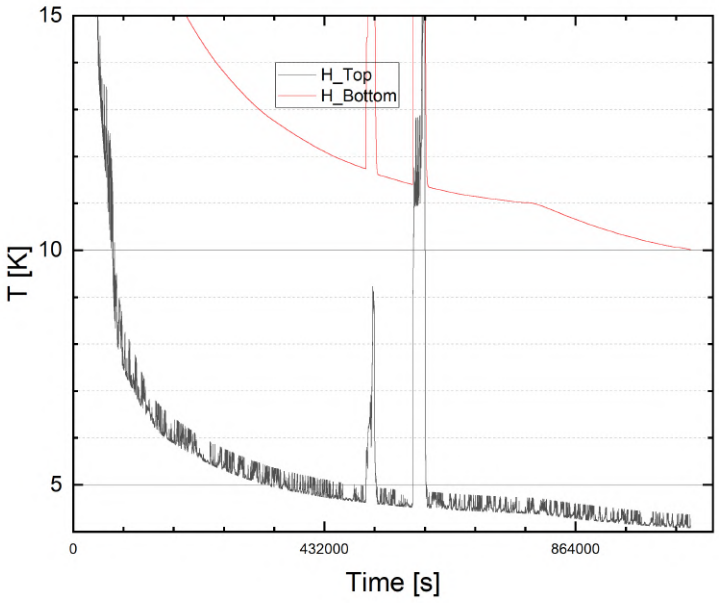

Figure 5.5: Plot showing the behaviour of the temperatures of the Strip H-Frame. The curve denoted as H Top describes the cooldown of the structure near the cold head, while H Bottom the one at the bottom left corner of the Cu support.After $t \approx 8 \cdot 10^5$ s, the effect of the calibrator cryostat mounted in front of Strip's focal plane is visible.

It was assumed that the power exchanged radiatively between the slices and the filter ($\dot{Q}_{\frac{3}{4}+\frac{1}{4},filter} = 2.61$ W) equals that exchanged radiatively between the filter and the window. Therefore, the temperature of the window has been evaluated, giving $T_{window} = 251.8$

By considering that value of T_{window} as input in the ThermXL model of the system, the resulting output temperatures of the slices are:

- $\dot{Q}_{\frac{1}{4}} = 70$ K
- $\dot{Q}_{\frac{3}{4}} = 78$ K

Thus, they are near the boiling point of Nitrogen (77 K). Moreover, by considering a reasonably lower value for the temperaure of the window: $T_{window} = 230$ K, the results are:

- $\dot{Q}_{\frac{1}{4}} = 51$ K
- $\dot{Q}_{\frac{3}{4}} = 61$ K

The value obtained for T_{filter} is 220 K, which is close to the one that would ensure an internal temperature distribution of the calibrator cryostat compliant with the best expectations.

The dissipated powers between the two slices and the cold head second stage are computed by assuming that the ratio between the respective thermal conductivity of the current cool down and that of the first *dry run* equals that of the conductances (being the geometrical term $\frac{S}{L}$ the same). The results are $\dot{Q}_{\frac{3}{4}+\frac{1}{4},CH} = 0.49$ W.

The radiative heat exchange between the shield and the bottom of the slices must be considered too. The resulting dissipated power from the shield walls and the back of the slices is $\dot{Q}_{\frac{3}{4}+\frac{1}{4},Shield} = 0.99$ W.

Therefore, the power dissipated radiatively from the shield onto the slices is dominant with respect to that dissipated conductively by the cold head.

After one day with the polarimeters in Strip's focal plane facing the absorbing panels, the active cool-down started.

The thermal effect of the cooling down of the calibrator cryostat on the internal Strip's subsystems has been a reduction in the minimum temperatures reached.

For what concerns the calibrator, its subsystems cool at a faster rate with respect to *dry run* 6. However, it must be underlined that the initial values of the temperatures were lower with respect to the previous run, given the fact that the calibrator had been preliminarily cooled radiatively by the Strip's cold cryostat.

After one week, the internal pressure of the calibrator cryostat is $P = 2.2{\cdot}10^{-7}$ mbar. The table reporting the minimum temperatures reached by the different subsystems of the calibrator cryostat is reposted below.

Table 5.2: Minimum T measured by the different thermometers of the integrated and cooled calibrator.

Component	**Temperature [K]**
CH II stage	24.85
CH I stage-Shield Base	48.35
Strap CH side	28.78
Slice 1/4	72.11
Slice 3/4	95.48
IR filter	218.45
Mid IF ray	99.98
Central back disk	155.02
CR-Panel	182.94
PL-Panel	165.51

The plot showing the cooling down results is reported.

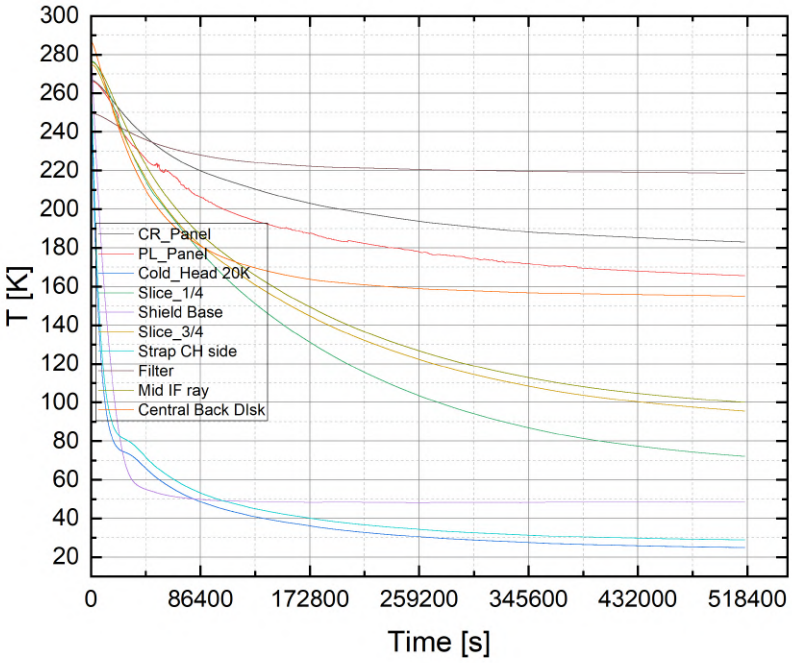

Figure 5.6: Plot showing the T *vs* t curves for the calibrator.

5.2 Strip's polarimeters responsivity and T_{noise} estimation

Measures have been performed with Strip's polarimeters, in order to determine a preliminary calibration curve and a first estimate of the noise temperature T_{noise}. These results are preliminary because the Strip instrument configuration is not the nominal one: the polarimeters of the focal plane are not connected to the cold head second stage, thus, they are not actively cooled down. However, they reached $T \approx 160$ K as a consequence of the reduced radiative heat load from the shield, that is thermalised with the cold head first stage, and from the calibrator, that is cooled down.

Several tests were performed in the past years, in order to determine the **Strip polarimeters responsivity** in the operative temperature range, but the calibrator was still not present. Therefore, the calibration curve was built by the best fit line between only two reference signals, such as the ambient temperature at $T \approx 300$ K as warm load and a lower temperature, obtained by plugging the vacuum window with a reflective metal flange: this way, a reflected brightness temperature towards the receivers, proportional to the focal plane physical temperature, is generated. This method can only provide qualitative results, as it is very difficult to estimate the equivalent bright-

ness temperature of the reflective plate (given its low emissivity and multi-reflections). While, advantaging of the calibrator, that can be actively cooled down, it is possible to observe a quasi blackbody with the polarimeters, operating in a wider and tunable temperature range. Therefore, the calibration curve can be obtained not just from the best fit line connecting only two points, but a larger number of data (corresponding either to multiple discrete temperature steps, or to continuous temperature variations), resulting in a more accurate result, being based on an expanded statistical sample. In this way, the responsivity of the instrument in that temperature range is obtained as the angular coefficient of the best-fit line, assuming that the response is linear in the range considered (see Eq 3.4).

The **noise temperature** T_{noise} associated to the Low Noise Amplifiers (LNAs) of each polarimeter is obtained from this fit (equivalent to the application of the Y-factor method). Low-noise amplifiers are active components of the polarimeters, therefore, they introduce noise into the signal, which typically represents the main contribution to the overall noise of the instrument. Under ideal conditions, that is, in the absence of noise, the line should pass through the origin of the axes. This would occur if a zero-temperature calibrator were used, as no signal should be observed in such a case. However, this is not what happens, since the noise temperature acts as an additional load (a resistor at a physical temperature equal to the noise temperature) placed in front of the receiver, resulting in a positive signal measurement even when the load temperature is zero. By considering the value on the $x-$ axis, corresponding to the temperature for which $V = 0$ (where V is the output signal of a detector diode of a polarimeter), the corresponding temperature is T_{noise}.

In order to perform the aforementioned tests, it is necessary to measure the polarimeter output corresponding to different temperatures. The electronics of Strip generate a 100 Hz modulated digital signal, corresponding to the four PWR and DEM signals for each detector, while, for technical and convenience reasons, depending on the tests, it was decided to acquire the temperature of the calibrator sensors every 20 seconds or every 2 seconds (in the final tests, where, as we will see, better sampling is necessary). For this reason, the values of voltage outputs in ADU have been down-sampled by applying a rebin, in order to obtain one voltage in correspondence of each temperature, every 20 seconds or 2 seconds.

In this way it was possible to carry out two types of analyses: a slow-sampling analysis, using voltage-temperature pairs recorded every 20 seconds and a fast-sampling analysis, using pairs recorded every 2 seconds. The first one took place during the cool down of the calibrator (having a longer duration, of about 6 days), while, for the second one, the cryocooler was turned off, in order to let the absorbing panel heat up.

In this way, the signal measured by the polarimeters was measured with the variation of the temperature of the calibrator, on both short and long timescales.

5.2.1 Uncertainties and Limitations

At the current integration stage, the system still presents a non-negligible number of uncertainties, which will be solved or, at least, reduced, subsequently. Specifically:

1. The **biases** VD (drain voltage) and VG (gate voltage) applied to the polarimeters are set to allow operation at the physical temperature at which they are currently working ($\approx$ 160 K), which is significantly different from the nominal one ($\approx$ 25 K). In addition, the observed scene covers a wide temperature range, from approximately 300 K down to more or less 100 K.

2. The **observed temperature** results from a combination of different sources: the blackbody-like emission from the absorbing panels, the reflective slices (having weak emissivity), and the temperature of the surrounding environment.

3. The **window temperature** is currently not directly measured, but only estimated from the thermal model. The window behaves as a microwave emitter at its physical temperature T_{win}, with its emissivity of about 0.1 (including also other passive components, at the head of the LNAs, contributes in addition to the total losses). The window cools down as the calibrator temperature decreases, but with a delay. Therefore, the window introduces a differential offset on the "hot" and "cold" temperatures observed by the polarimeters, influencing the evaluation of the Y-factor.

A simplified RF model can be constructed, with a few unknown parameters. The first concerns the way in which the temperatures of the absorbing panels and slices combine to determine the brightness temperature observed by the polarimeters, which can be written as:

$$T_{cal} = T_{slice} \cdot \alpha + T_{panel} \cdot (1 - \alpha), \tag{5.1}$$

where α is a mixing parameter that depends on the portion of the calibrator seen by each polarimeter's horn.

The second regards the variation of the window temperature (including also IR filters in this simplified model), which affects both T_{hot} and T_{cold}, expressed as:

$$T_{hot} = T_{cal,hot} \cdot (1 - \varepsilon_{win}) + T_{win,hot} \cdot \varepsilon_{win}, \tag{5.2}$$

$$T_{cold} = T_{cal,cold} \cdot (1 - \varepsilon_{win}) + T_{win,cold} \cdot \varepsilon_{win}, \tag{5.3}$$

assuming a linear emissivity $\varepsilon_{win} = 0.1$, considering the window and other passive components.

The main unknowns in this model are:

- The **drift in received power** that may happen when the polarimeters are switched on and off to determine the offset

- The **temperature gradient** across the filters and the window.

5.2.2 Strip's polarimeters used

In these tests eight Q-band polarimeters have been used. They are reported in Table 5.3, together with the load they are observing.

Board	Polarimeter	Load
Y	2	Slice $\frac{3}{4}$
	3	TK-RAM
O	4	CR-110
	5	CR-110
I	1	TK-RAM
	6	Slice $\frac{1}{4}$
R	0	CR-110
	6	CR-110

Table 5.3: Table reporting the polarimeters used, including the board they belong to and the respective observed load.

The following image was included in order to clarify what the biased polarimeters are observing.

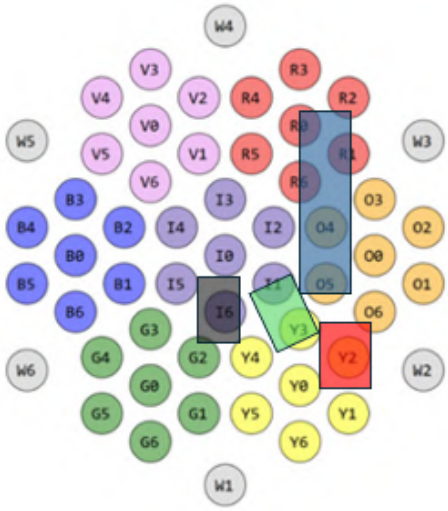

Figure 5.7: Image showing what the different biased polarimeters are orbserving. Specifically, the blue box indicates the CR-110 panel, the green one that of TK-RAM, the black one the $\frac{1}{4}$ slice and the red one the $\frac{3}{4}$.

The polarimeters were turned on (biased) on 29/09/2025 at 12:25 UTC.

5.2.3 Offset determination

The offset is a digital bias, produced by the instrument's electronics. In particular, each detector diode (in charge to integrate the signal amplified through the receiver), receives and straightens the oscillating EM signal, converting it in a DC signal proportional to the amplitude of the input signal. This voltage is then further amplified by the electronic circuitry, in order to improve the signal-to-noise ratio ($\frac{S}{N}$). After the amplification, the analogue-to-digital converter (ADC) digitizes the signal into arbitrary digital units (ADU), providing its corresponding value.

This processing of the signal introduces the offset, that is not part of the desired measurements, thus, it must be quantified and subtracted.

In order to do so, the amplifiers have been disabled by setting the drain voltage $V_D = 0$. In this way the signal path through the polarimeter to the detector is interrupted and no actual signal is passing through the polarimeter, allowing the measurement of the offset component generated solely by the electronic system (and the detector diode, looking just a not-amplified thermal signal).

The most accurate responsivity measurement procedure involves an offset measurement at each temperature step. This is to account for any (frequent) offset drift over time, due both to electronic drift (ADC gain circuits) and to the different responsivity of the diode as its physical temperature varies. Therefore, an offset measurement has been performed before the slow-sampling analysis and others during the fast-sampling analysis.

The offsets are computed as the average value of the PWR signal measured by each detector during the time range with $V_D = 0$. Then, this value is subtracted from the interpolated voltage outputs, before performing the best-fit in the plot $V\ vs\ T$.

The HDF5 files used to evaluate the offsets (by setting $V_D = 0$) related to the fast and slow sampling are reported in the following Table.

File name	Time range (UTC)	Sampling
`2025_10_09_13-44-12.h5`	14:03:00 - 14:13:00	Slow
`2025_10_10_10-44-12.h5`	10:55:00 - 11:00:00	Fast
`2025_10_10_16-44-11.h5`	17:08:00 - 17:13:00	Fast

Table 5.4: Table reporting the HDF5 files used to determine the offsets. The time range selected within the whole HDF5 file is reported, together with the fast- or slow-sampling specification.

An intermediate offset was also computed as the arithmetic mean between the two offsets of the fast sampling.

5.2.4 T_{noise} estimation - calibrator cool down

This analysis provides a cooling down of the calibrator over a wide range of temperatures, which provides a subsequently significant variation in the voltage outputs. On the other hand, the long duration of the analysis introduces uncertainties linked to the variation of the instrument response over time, mostly caused by the cross-coupling between the calibrator (cooling down) and the Strip instrument facing it.

The fact that the offset was measured only at the end of the cool down (for technical reasons the offset data at the beginning could not be recovered) adds other uncertainties. A more accurate analysis would require more than one offset measurement, so that each dataset can be associated with the offset taken closest in time.

The acquisition of the calibrator cryostat internal temperatures was started on 30/09/25 at 08:31 UTC, when the calibrator cool down started. The temperatures are sampled every 20 seconds.

The HDF5 files that were used are reported in the following Table:

File name	ID number	Time range (UTC)
`2025_09_30_09-44-12.h5`	1	09:44:12 - 10:42:00
`2025_10_02_02-44-11.h5`	2	02:44:11 - 03:42:00
`2025_10_03_16-44-11.h5`	3	16:44:11 - 17:42:00
`2025_10_06_03-44-12.h5`	4	03:44:12 - 04:42:00

Table 5.5: Table reporting the HDF5 files used in the slow-sampling analysis with the calibrator cooled down. The time range selected within the whole HDF5 file is reported too.

The voltage offset (in ADU) was hence measured at the end of the cooldown of the calibrator. The file used to compute the offset for the slow-sampling analysis is the one indicated in the previous paragraph.

The temperatures of the two absorbing panels and of the two slices at the beginning of the test are:

- $T_{\frac{1}{4}} = 272.37$ K
- $T_{\frac{3}{4}} = 270.32$ K
- $T_{CR-110} = 264.34$ K
- $T_{TK-RAM} = 263.93$ K

At the end of the test the temperatures are:

- $T_{\frac{1}{4}} = 72.78$ K
- $T_{\frac{3}{4}} = 96.11$ K

- $T_{CR-110} = 183.27$ K
- $T_{TK-RAM} = 165.84$ K

5.2.5 T_{noise} estimation - calibrator warm-up

This part of the analysis was performed in order to verify whether the polarimeters in the Strip focal plane are sensitive to a temperature variation (increase) of roughly 10 K, in the case of the absorbing panels, and of roughly 25 K for the slices, by turning off the cryocooler for ≈ 5 hours. Therefore, the expected ADU variation is reduced with respect to the one of the previous analysis.

In this test, lasting only 5 hours, small uncertainties in the environmental conditions of Strip are expected; however, even small drifts in offset or signal may introduce large uncertainties in the estimation of the noise temperature

The cryocooler was turned off on 2025-10-10 at 11:14:53, in order to let the polarimeters in the focal plane observe the heating of the two blackbodies. The system was again cooled down on 2025-10-10 at 17:44:11.

The temperatures are sampled every 2 seconds.

In the following Table the used HDF5 files are reported.

File name	ID number	Time range (UTC)
`2025_10_10_11-44-11.h5`	1	11:44:11 - 12:42:00
`2025_10_10_13-44-11.h5`	2	13:44:11 - 14:42:00
`2025_10_10_15-44-11.h5`	3	15:44:11 - 16:42:00

Table 5.6: Table reporting the HDF5 files used in the fast-sampling analysis with the calibrator cryostat turned off . The time range selected within the whole HDF5 file is reported too.

The offsets associated to the voltage outputs are taken before turning off the cooler and before turning it on again.

The temperatures of the two absorbing panels and of the two slices at the beginning of the test are:

- $T_{\frac{1}{4}} = 73.96$ K
- $T_{\frac{3}{4}} = 93.82$ K
- $T_{CR-110} = 181.26$ K
- $T_{TK-RAM} = 164.15$ K

At the end of the test the temperatures are:

- $T_{\frac{1}{4}} = 101.87$ K

- $T_{\frac{3}{4}} = 113.7$ K
- $T_{CR-110} = 187.91$ K
- $T_{TK-RAM} = 172.61$ K

Analysis and interpretation of the results

At first, the noise temperatures were computed both from the best-fit method and using the Y-factor, by applying the nominal physical temperatures observed by the polarimeters: that of the CR-110 panel, that of the TK-RAM panel and those of the slices (as if they were blackbodies).

For completeness, the results are reported in Appendix B and in Appendix C, together with the measured signal levels, which are useful for subsequent analyses. Most of these results yield negative noise temperatures, and are, therefore, physically meaningless.

In the following tables, some of the positive obtained values for the T_{noise} are reported.

Polarimeter	$T_{noise}(Q_1)$	$T_{noise}(Q_2)$	$T_{noise}(U_1)$	$T_{noise}(U_2)$
O4	87.94 ± 5.6	68.8 ± 4.3	52.8 ± 6.7	70.5 ± 4.7
I1	123.6 ± 1.7	131.9 ± 2.8	177.7 ± 3.5	108.5 ± 2.0
I6	465.4 ± 4.9	417.7 ± 3.9	471.1 ± 6.2	435.8 ± 4.9

Table 5.7: Table reporting the evaluated values of the T_{noise}, for each detector diode of each polarimeter during the calibrator cool down.

Polarimeter	$T_{noise}(Q_1)$	$T_{noise}(Q_2)$	$T_{noise}(U_1)$	$T_{noise}(U_2)$
O4	576.0 ± 14.2	494.9 ± 14.3	254.5 ± 4.9	351.1 ± 7.4
I6	327.6 ± 1.5	256.3 ± 1.3	358.8 ± 1.8	316.1 ± 1.3

Table 5.8: Table reporting the evaluated values of the T_{noise}, for each detector diode of each polarimeter during the calibrator's warm up.

The negative values of T_{noise} are are mathematically due to one of the two following conditions:

- Y-factors lower than one (occurring only in a few instances)
- an excessively high polarimeter responsivity, that is, an overly large ratio of $\frac{\Delta V}{\Delta T}$.

Y-factors lower than one can be attributed to cases in which the change in the observed conditions is small compared with the uncertainties in the signal estimation.

These uncertainties are typically caused by: (i) offset drifts between the beginning and end of the measurement, when only one offset value is available and (ii) signal drifts, due to possible changes in the environmental conditions.

In the second case, which results in a Y-factor that is higher than expected or even variable depending on the environmental conditions, the signal variation is too large compared with the corresponding temperature variation. As a result, the second term in the numerator becomes larger than the first one, making the numerator negative. This suggests either an incorrect estimation of the brightness temperature associated with the observed load or a change in the responsivity of the polarimeter (affecting either the LNA or the detector diode or both) when its physical (thermal) conditions change.

The next step was to make assumptions regarding the observed temperature. In particular:

- the temperature T_{hot} was assumed to be correct
- the value of T_{cold} was then calculated so as to yield a reasonable T_{noise} for the current configuration
- the same T_{noise} value was assumed for all polarimeters

Based on the signal model, it can be estimated that under nominal conditions, with optimal bias settings and a physical temperature of 20 K, the polarimeters would exhibit a noise temperature greater than 80 K. This estimate assumes an intrinsic noise temperature of 25 K, a thermal susceptibility of the noise with respect to the physical temperature of at least 0.24 K/K, and an additional contribution introduced by the window and all the other passive components of the polarimetric chain.

Therefore, for each polarimeter, T_{cold} can be evaluated by solving the Y-factor equation for it, yielding

$$T_c^* = \frac{(1 - Y) \cdot T_n + T_h}{Y} \tag{5.4}$$

The calculation was done for the polarimeters O4, I1 and I6 (that are situated at the centre of Strip's focal plane), giving as results:

Cool down data: the obtained temperatures are very close to those of the slices. This suggests that, in the considered configuration based on the simple above assumptions, the main contribution to the observed brightness temperature comes from the slices rather than from the absorbing panel.

Warm up data: the results instead indicate that the temperature of the slices should be used in order to minimize T_{noise}, although the corresponding T_{noise} values remain different (and generally higher than in the cooldown test).

In order to try to find greater consistency among the results and base on a more physical model, the previously developed RF model was applied to the warm-up test

for polarimeters I1, I6, and O4, which are located in adjacent areas of the focal plane, sharing similar thermal conditions (heat load form the same region of the window and filter facing them) .

$$T_h = [T_{TK-RAM,hot} \cdot \alpha + T_{slice,hot} \cdot (1-\alpha)] \cdot (1-\varepsilon_{window}) + T_{Hot,window} \cdot \varepsilon_{window}, \quad (5.5)$$

$$T_c = [T_{TK-RAM,cold} \cdot \alpha + T_{slice,cold} \cdot (1-\alpha)] \cdot (1-\varepsilon_{window}) + T_{Cold,window} \cdot \varepsilon_{window}. \quad (5.6)$$

with $\varepsilon_{window} = 0.16$, $T_{Hot,window} = 240$ K and $T_{Cold,window} = 231$ K.

The model was applied to obtain the T_h and T_c of the first and the last dataset of the warm-up test (the temperatures considered for the $\frac{3}{4}$ slice, and the TK-RAM panel are the ones reported in Subsection 5.2.5).

The results are:

- $T_h = 166.12$
- $T_c = 155.61$

The value of T_{noise} reported in the following Table are obtained from the Y-factor method by (following the order of the columns):

- Using as T_h and T_c the ones derived from the expression of the developed model
- Using T_h and T_c of the $\frac{3}{4}$ slice
- Using T_h and T_c of the TK-RAM panel
- Using a combination of T_{slice} and T_{TK-RAM}, with a mixing factor $\alpha = 0.75$ (to obtain results similar to those predicted by the model).

To conclude, the method used is certainly useful at a qualitative level, but it is not able to provide precise quantitative results.

However, it could serve as a valid backup to the baseline method (based on the rotation of the slices by $\pm 180°$, assuming that the slices reach different temperatures) if a series of precautions are adopted, such as:

- Measure the offset using rapid on/off cycles that do not significantly affect the polarimeter's thermal state (and thus its responsivity). This effect is expected to be less critical when the focal plane is actively connected to the second stage of the cryocooler and cooled to lower temperatures than the current ones.
- Use active heaters to warm up the slices instead of relying on passive warm-ups. This allows heat-up and cool-down cycles to be accelerated and controlled through an automated procedure, alternated with offset measurements.

POL	**DET**	P_{cold}	**Offset 1**	P_{hot}	**Offset 2**	**Y**	$T_{n,model}$	$T_{n,slice}$	$T_{n,RAM}$	$T_{n,mix}$
I1	Q1	208189	214519	208842	215443	1.043	89.9	274.7	22.9	85.8
I1	Q2	211163	216162	211907	217168	1.052	45.0	206.3	-11.4	43.1
I1	U1	232371	239609	232973	240513	1.042	96.3	284.5	27.7	91.9
I1	U2	208612	215476	209199	216350	1.042	95.8	283.7	27.3	91.4
I6	Q1	210620	218259	211297	219323	1.051	51.9	216.8	-6.1	49.6
I6	Q2	210356	216544	211044	217615	1.062	14.2	159.5	-34.7	13.8
I6	U1	213307	222112	213956	223172	1.047	69.6	243.8	7.4	66.5
I6	U2	214968	223728	215585	224753	1.047	70.1	244.5	7.8	67.0
O4	Q1	344996	350500	345176	350913	1.042	92.7	279.0	25.0	88.5
O4	Q2	324754	329341	324959	329749	1.044	81.9	262.5	16.8	78.2
O4	U1	298540	306642	298729	307096	1.033	165.8	390.2	80.6	158.0
O4	U2	326198	331448	326362	331826	1.041	102.3	293.5	32.3	97.6

Table 5.9: Table summing up the results for the T_{noise} calculation.

- Monitor the temperature of the Strip window by adding a thermometer in a position that minimally impacts the field of view of the feedhorns. This measure is useful regardless of the method employed.
- Fully cover the slices with absorbing panels so that an observed brightness temperature can be uniquely associated without making strong assumptions on the emissivity of the slices and the surrounding environment (as in the case studied).
- Accurately characterise the variation of the polarimeters' responsivity (both of the diodes and the amplifiers) as a function of their physical temperature, in order to apply post-processing corrections to both the determination of the offset and to spurious signal drifts caused by generic gain variations of the polarimeter, which can mimic a change in the input signal.

Conclusions

The calibrator is a relevant subsystem, allowing to characterize and optimize the Strip instrument, both thermally and radiometrically. The Strip calibrator is a subsystem needing to operate in cryogenic conditions. In this aim, it was fundamental to characterize its thermal-vacuum behaviour and optimize its performance to fit the Strip test requirements.

My thesis work starts from a configuration of the calibrator only partially assembled, and describes in detail the steps taken to arrive at an architecture close to the definitive one, which will be completed in the next few months.

The assembly followed an incremental scheme, adding successive levels of complexity, to characterize also the detailed behaviour arising from the interaction of the different components. The activities are logically divided in three phases: each phase was complemented and followed by experimental tests to provide immediate feedback on the correct progress and confirmation of the predictive theoretical models.

The work includes both stand-alone calibrator activities and other involving the integrated Strip and the calibrator-system. The former is aimed at completing the calibrator assembly, characterizing and optimizing it, while the latter evaluated the interaction between the calibrator and Strip and provided practical recommendations for improving the final architecture, test procedures, and data analysis.

The work described is developed through several tests, following a flow aimed at creating the conditions necessary to reach the vacuum and cryogenic temperature levels required for the Strip system tests. These were followed by tests of the integrated calibrator, aimed at obtaining an estimate, albeit still preliminary, of the interaction between the polarimeters (only a subset was on) and the calibrator, and useful indications regarding the measures to be adopted for correct use of the calibrator as a blackbody reference source for Strip.

A first phase includes all the tests performed on the stand-alone calibrator, insulated with respect to external environment. We obtained a first assessment of the capability of the instrument to reach and maintain cryogenic temperatures. Such a set of runs, in details, allowed to have a preliminary estimation of the main parameters driving the heat exchanges, inside the cryostat, and of its parts with the surrounding environment. This output was used as input to build a simplified thermal model which allows the prediction of thermal behaviour in the next phases of the process.

The second phase includes all the intermediate activities aimed at studying the

interaction between the calibrator and the external environment. These tests were performed both with the two sub-systems integrated and with the stand-alone calibrator closed by a vacuum window, representative of the Strip interface (material, size, thermal distribution).

From this set of runs we derived a clear confirmation of a relevant radiative heat load on the inner parts of the cryostat due to the presence of the vacuum window, a high emissivity body at almost room temperature. To mitigate this unwanted effect, an IR (infrared) filter was designed, manufactured and procured. I developed a dedicated thermal model allowing for the estimation of the radial temperature distribution of the IR filter and its expected thermal impact on the inner parts of the calibrator cryostat.

A dedicated test was run to measure the impact of the IR filter when integrated in the calibrator cryostat. These data were also used to refine the thermal model (fine tuning). During this phase two absorbing panels, representative of the two typologies (different in materials and design) selected as potential candidates to be used, were integrated.

The last phase, the third, includes all the tests performed with the calibrator in its closer to final architecture (nominal IR filter, only two absorbing panels, 10 out of the nominal 12 thermometers present, rotation system disabled) firstly alone, then integrated with Strip: in this test configuration a subset of the polarimeters was turned on.

These final activities allowed to: (i) have a reliable estimation of the temperature distribution we can expect for the nominal test; (ii) debug and identify, between the different options explored (test procedures run and data analysis methods applied), the best solutions allowing to measure the Strip noise properties; (iii) identify some key-elements, specific of this test setup, to be taken into account to improve the accuracy of the Strip calibration and the overall knowledge of the instrument.

Appendix A

Typical procedure to put under thermal vacuum the cryostat

The practical procedure to put Strip and its calibrator under thermal vacuum is analogous to that of any other cryostat.

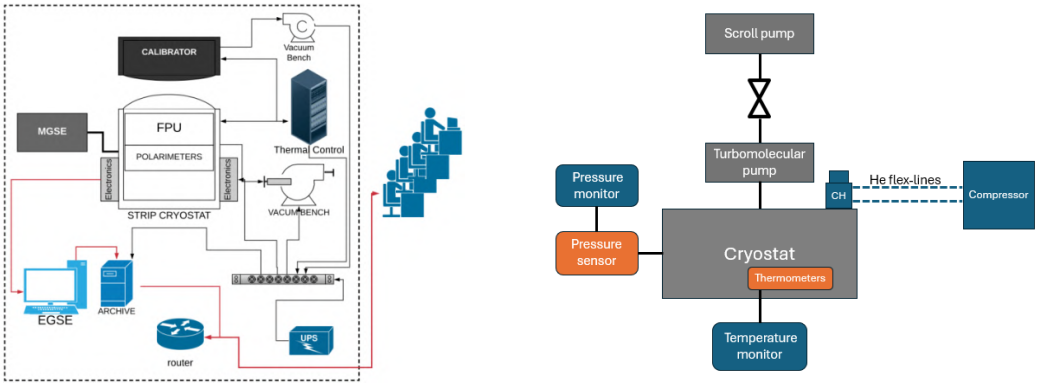

Figure A.1: *Left panel*: Scheme representing the hardware of Strip. *Right panel*: Focus on the vacuum pumping and cryocooler connection.

The first step is to put the cryostat under vacuum. In order to reach optimal values of pressure (almost 10^{-7} mbar in the case of Strip and its calibrator) a pre-vacuum must be obtained. For this scope a dry Scroll pump is previously used (reaching P almost 10^{-2} mbar) with a tombac vacuum line mounted.

Then, the vacuum line is attached to the valve on the rear of the cryostat, connecting its interior with the external environment. At first the valve must be closed, due to the fact that the vacuum line needs to be cleaned by pumping with the Scroll pump only over it. In fact, when the pump is started, residual water vapour and contaminants inside the tube can affect performances. For this reason, many scroll pumps are equipped with a gas ballast. It introduces air to dilute and prevent condensation, in order to avoid potential damages to the pump.

The gas ballast valve of the vacuum pump is turned on at its maximum level. After almost 10 minutes, the gas ballast level is reduced. Then the rear valve of the cryostat must be carefully and slowly opened, so as to let the Scroll vacuum pump start pumping over the chamber to reach the wanted pre-vacuum. After other almost 30 minutes, gas ballast is turned off.

Figure A.2: The dry Scroll vacuum pump used to evacuate the calibrator (pre-vacuum).

The time needed in order to reach Pressures of the order of 10^{-2} mbar strongly depends on the volume of the chamber to evacuate and on the pump capacity. For example, in the case of the calibrator, 24 hours are often enough. After having reached the pre-vacuum with the Scroll pump (P almost 10^{-2} mbar), the Turbomolecular pump is activated (with the Scroll pump still active, working as a backing pump), in order to efficiently remove light gaseous molecules too, that mechanical pumps cannot handle. Therefore, an even deeper vacuum is obtained, through the pumping with the turbomolecular pump.

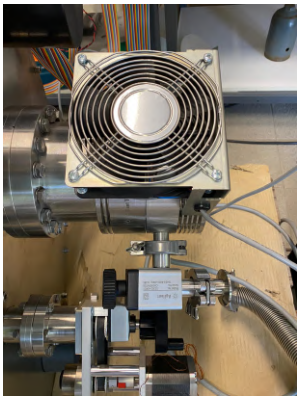

Figure A.3: The Turbomolecular vacuum pump used with the calibrator. The valve to which the Scroll pump is connected is visible too.

Once reached P almost 10^{-4} mbar, the cryocooler (a two-stages Gifford-McMahon He cryocooler in the case of the experiment described) is turned on from its compressor.

Figure A.4: The Gifford McMahon two.stages He cryocooler, mounted on the calibrator cryostat.

Yet, before switching on the cryocooler, it must be ensured that the compressor cooling circuit is active (necessary to cool down the hot gaseous He coming out from the cryocooler towards the compressor at the end of the thermodynamical cycle).

Figure A.5: Front of the compressor, connected to the cryocooler through two He flex lines.

The starting of the cooling procedure has also a positive feedback on the internal pressure, because it makes residual molecules condensate on the vacuum vessel walls. In the case of this experiment, the final pressures reached (with the action of vacuum pumping and cooling) are of the order of 10^{-7} mbar.

The values of the temperatures of the different subsystems and of the internal pressure are measured during the outlined procedure through the respective sensors. The pressure sensor is connected to turbomolecular vacuum pump monitor via an ethernet cable and turned on from it.

The thermometers are located in the various internal subsystems of the instrument in order to monitor their temperatures. These thermometers (Silicon diodes and Cernox resistors in this case) must be externally connected through flat cables to monitors, which enable also the acquisition of the data through the connection with a GPIB to a local PC.

Figure A.6: The sensor used to monitor the internal pressure of the calibrator cryostat.

For what concerns the procedure to open a cryostat, it is necessary to at first make it reach a temperature almost equal to the ambient one (more or less 300 K) and analogously for the pressure (of the order of 10^3 mbar). Therefore, the cryocooler and the vacuum pumps must be turned off. After a certain time period, again depending on the dimension of the cooled chamber, the internal temperature would reach the ambient one. Subsequently, the rear valve of the cryostat can be slowly opened so as to let air enters the chamber to get a value of internal pressure close to 10^3 mbar. Then, the cryostat can be opened.

Appendix B

Plots and tables, calibrator cool down

Board O	
File ID	**T_{board} [K]**
1	170.9
2	166.35
3	162.61
4	159.14

Table B.1: Table reporting the average temperature of the board for different data files.

Board O, Polarimeter O4		
Offset file name	**Time range (UTC)**	**Offset [ADU]**
`2025_10_09_13-44-12.h5`	14:03:00 - 14:13:00	**PWR Q1**= 348861.96
		PWR Q2= 327823.41
		PWR U1= 304596.11
		PWR U2= 329837.34

Table B.2: Table reporting the offset value considered for the detectors.

Board O: Polarimeter O4		
File ID	$\overline{\mathbf{T}}_{\mathbf{cal}}$ **[K]**	$\overline{\mathbf{V}}$ **[ADU]**
1	264.34	**PWR Q1**= −87079.91
		PWR Q2= −83761.23
		PWR U1= −100361.83
		PWR U2= −84795.27
2	205.93	**PWR Q1**= −57217.02
		PWR Q2= −54557.48
		PWR U1= −66972.95
		PWR U2= −55577.01
3	191.50	**PWR Q1**= −35304.79
		PWR Q2= −33429.89
		PWR U1= −42553.82
		PWR U2= −34294.61
4	183.27	**PWR Q1**= −16444.47
		PWR Q2= −15092.26
		PWR U1= −20818.10
		PWR U2= −15899.87

Table B.3: Table reporting the average temperatures of the observed calibrator subsystem and the related average values of the voltage output of the detectors, for the different data files.

Board O, Polarimeter O4-Fit with 4 datasets		
Detector	**α [ADU/K]**	**T_n [K]**
Q1	-785.9 ± 10.1	-148.9 ± 3.3
Q2	-764.2 ± 9.7	-150.1 ± 3.3
U1	-882.2 ± 11.5	-145.9 ± 3.4
U2	-766.6 ± 9.8	-145.1 ± 3.3

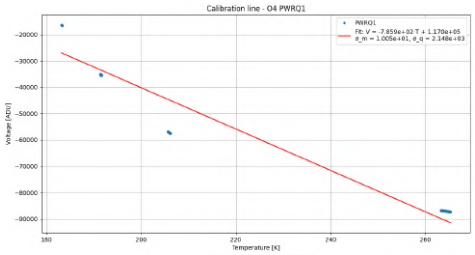

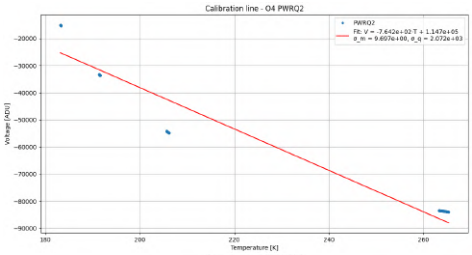

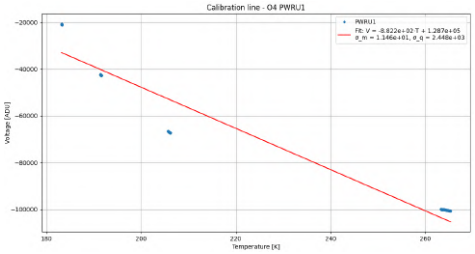

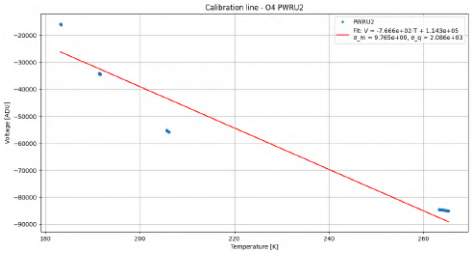

Board O, Polarimeter O4-Fit with 1 dataset: file 1		
Detector	**α [ADU/K]**	**T_n [K]**
Q1	-247.2 ± 4.9	87.9 ± 5.6
Q2	-251.1 ± 3.7	68.8 ± 4.0
U1	-316.4 ± 7.8	52.8 ± 6.7
U2	-253.3 ± 4.4	70.5 ± 4.7

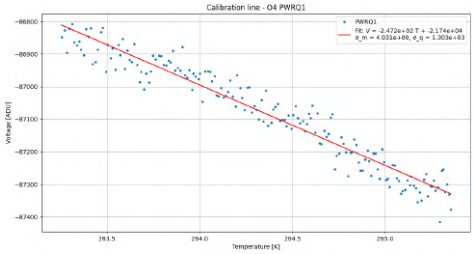

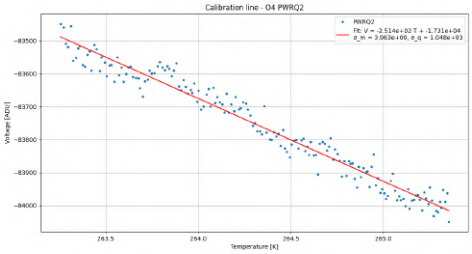

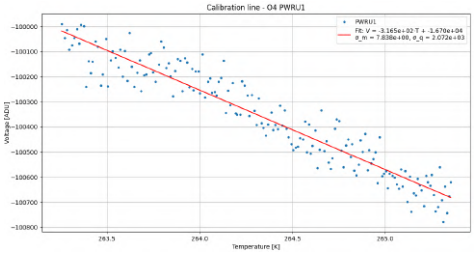

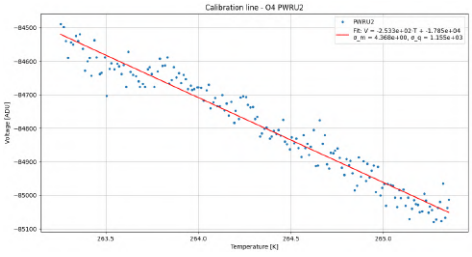

Board O, Polarimeter O4-Fit with 1 dataset: file 2		
Detector	**α [ADU/K]**	**T_n [K]**
Q1	-1160.0 ± 17.7	-156.6 ± 4.1
Q2	-1126.4 ± 16.9	-157.5 ± 3.9
U1	-1302.1 ± 27.8	-154.5 ± 5.5
U2	-1155.2 ± 18.9	-157.8 ± 4.3

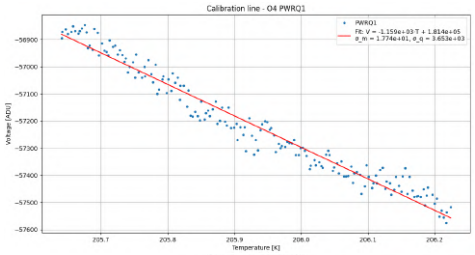

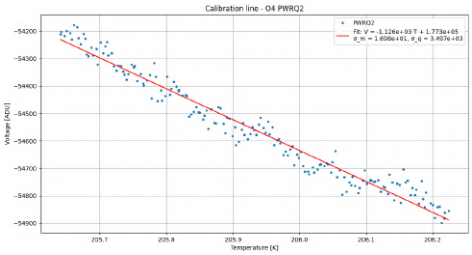

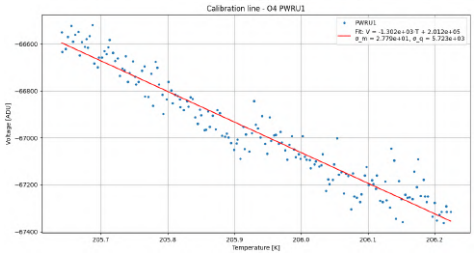

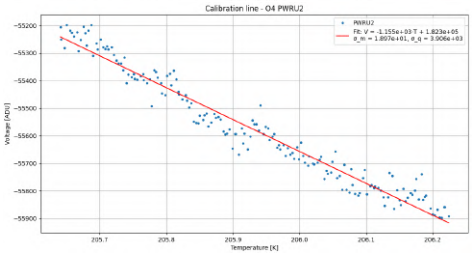

Board O, Polarimeter O4-Fit with 1 dataset: file 3		
Detector	**α [ADU/K]**	**T_n [K]**
Q1	-1795.9 ± 33.0	-171.9 ± 4.7
Q2	-1690.2 ± 32.3	-171.7 ± 4.9
U1	-1863.5 ± 61.7	-168.7 ± 8.5
U2	-1662.2 ± 35.2	-170.9 ± 5.4

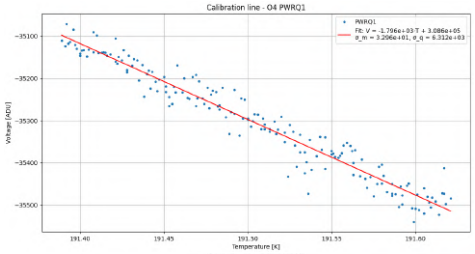

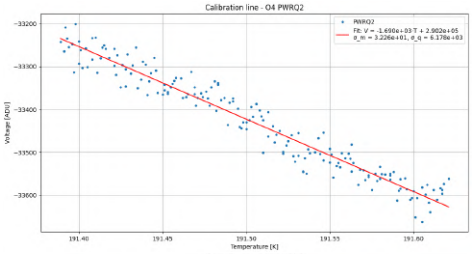

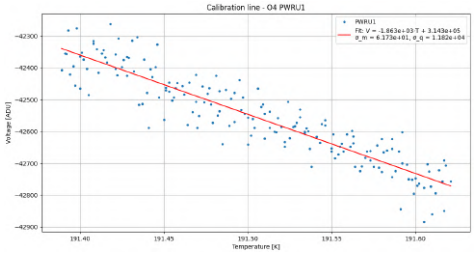

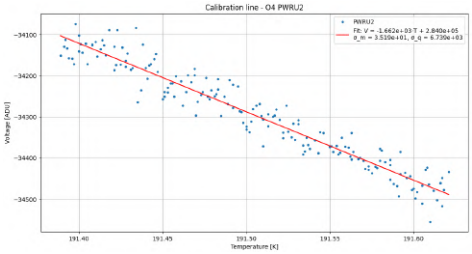

Board O, Polarimeter O4-Fit with 1 dataset: file 4		
Detector	**α [ADU/K]**	**T_n [K]**
Q1	-2756.6 ± 91.1	-177.3 ± 8.4
Q2	-2751.6 ± 109.8	-177.8 ± 10.2
U1	-3428.5 ± 173.3	-177.2 ± 12.9
U2	-2818.3 ± 100.1	-177.6 ± 9.1

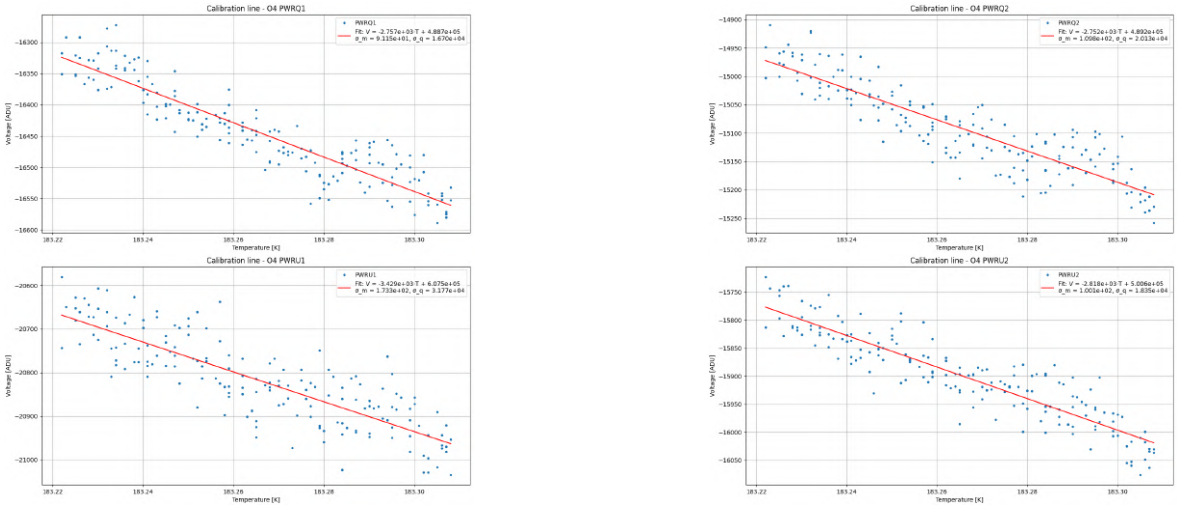

Board O, Polarimeter O4-Fit with 2 datasets: files 1,2		
Detector	**α [ADU/K]**	**T_n [K]**
Q1	-551.1 ± 0.3	-94.0 ± 0.1
Q2	-500.2 ± 0.2	-96.8 ± 0.1
U1	-571.6 ± 0.3	-88.8 ± 0.1
U2	-500.2 ± 0.3	-94.8 ± 0.1

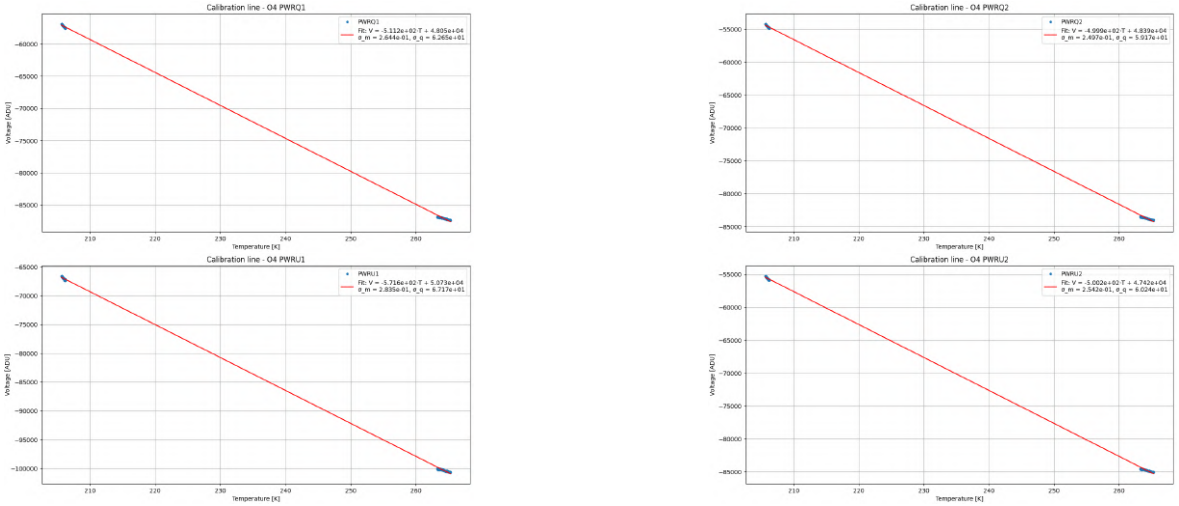

Board O, Polarimeter O4-Fit with 2 datasets: files 2,3		
Detector	**α [ADU/K]**	**T_n [K]**
Q1	-1520.0 ± 0.4	-168.3 ± 0.1
Q2	-1464.4 ± 0.6	-168.7 ± 0.1
U1	-1692.6 ± 0.6	-166.6 ± 0.1
U2	-1475.1 ± 0.4	-168.3 ± 0.1

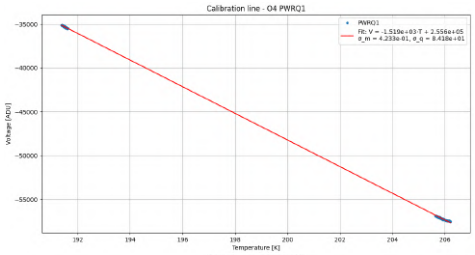

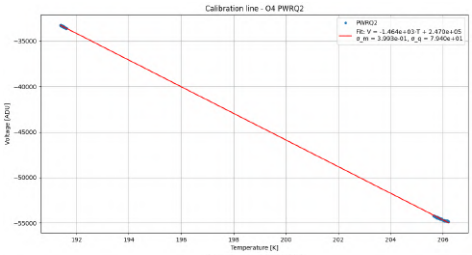

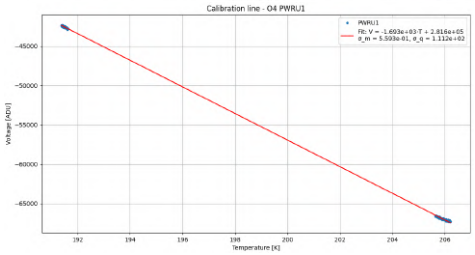

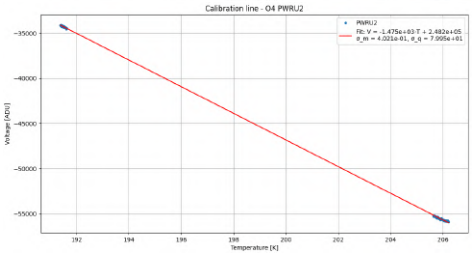

Board O, Polarimeter O4-Fit with 2 datasets: files 3,4		
Detector	**α [ADU/K]**	**T_n [K]**
Q1	-2289.2 ± 0.5	-176.1 ± 0.1
Q2	-2225.8 ± 0.6	-176.5 ± 0.1
U1	-2638.2 ± 0.9	-175.4 ± 0.1
U2	-2232.7 ± 0.6	-176.1 ± 0.1

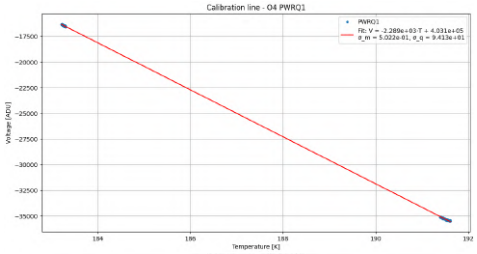

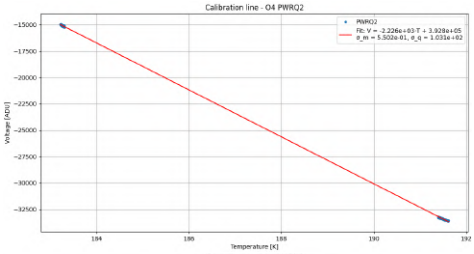

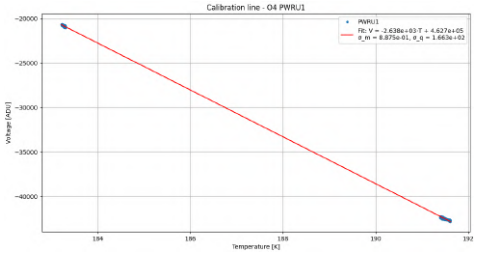

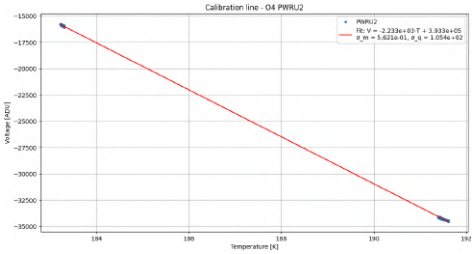

Board O, Polarimeter O5		
Offset file name	**Time range (UTC)**	**Offset [ADU]**
`2025_10_09_13-44-12.h5`	14:03:00 - 14:13:00	**PWR Q1**= 209862.07
		PWR Q2= 203282.94
		PWR U1= 213482.30
		PWR U2= 200936.35

Table B.4: Table reporting the offset value considered for the detectors.

Board O: Polarimeter O5		
File ID	$\overline{\mathbf{T}}_{\mathbf{cal}}$ **[K]**	$\overline{\mathbf{V}}$ **[ADU]**
1	264.34	**PWR Q1**= −153251.25
		PWR Q2= −154634.99
		PWR U1= −158297.57
		PWR U2= −156890.79
2	205.93	**PWR Q1**= −104330.73
		PWR Q2= −105353.45
		PWR U1= −107940.07
		PWR U2= −106974.55
3	191.50	**PWR Q1**= −63758.99
		PWR Q2= −64723.58
		PWR U1= −66455.42
		PWR U2= −65855.34
4	183.27	**PWR Q1**= −26914.47
		PWR Q2= −27179.09
		PWR U1= −28143.51
		PWR U2= −27905.57

Table B.5: Table reporting the average temperatures of the observed calibrator subsystem and the related average values of the voltage output of the detectors, for the different data files.

Board O, Polarimeter O5-Fit with 4 datasets		
Detector	**α [ADU/K]**	**T_n [K]**
Q1	-1384.3 ± 20.2	-148.4 ± 3.8
Q2	-1394.7 ± 20.4	-148.2 ± 3.8
U1	-1424.4 ± 20.8	-147.9 ± 3.8
U2	-1411.7 ± 20.6	-147.9 ± 3.8

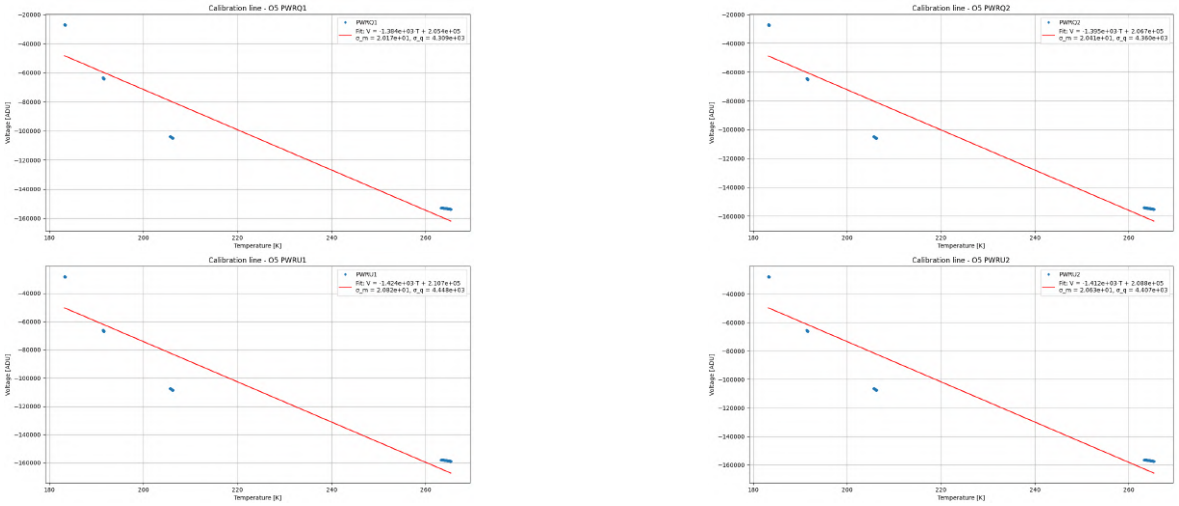

Board O, Polarimeter O5-Fit with 1 dataset: file 1		
Detector	**α [ADU/K]**	**T_n [K]**
Q1	-409.9 ± 2.5	110.4 ± 1.7
Q2	-433.8 ± 5.7	92.1 ± 3.7
U1	-440.7 ± 3.2	94.8 ± 2.0
U2	-442.2 ± 3.3	90.5 ± 2.1

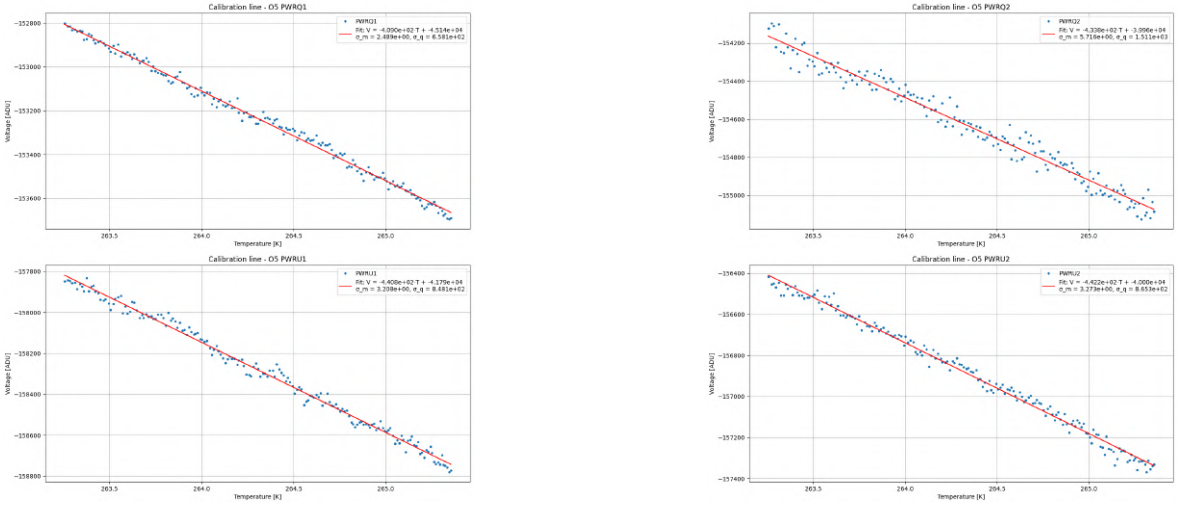

Board O, Polarimeter O5-Fit with 1 dataset: file 2		
Detector	**α [ADU/K]**	**T_n [K]**
Q1	-2017.4 ± 13.1	-154.2 ± 1.7
Q2	-2028.4 ± 23.0	-154.0 ± 2.9
U1	-2175.1 ± 10.1	-156.3 ± 1.2
U2	-2090.8 ± 1.0	154.8 ± 1.3

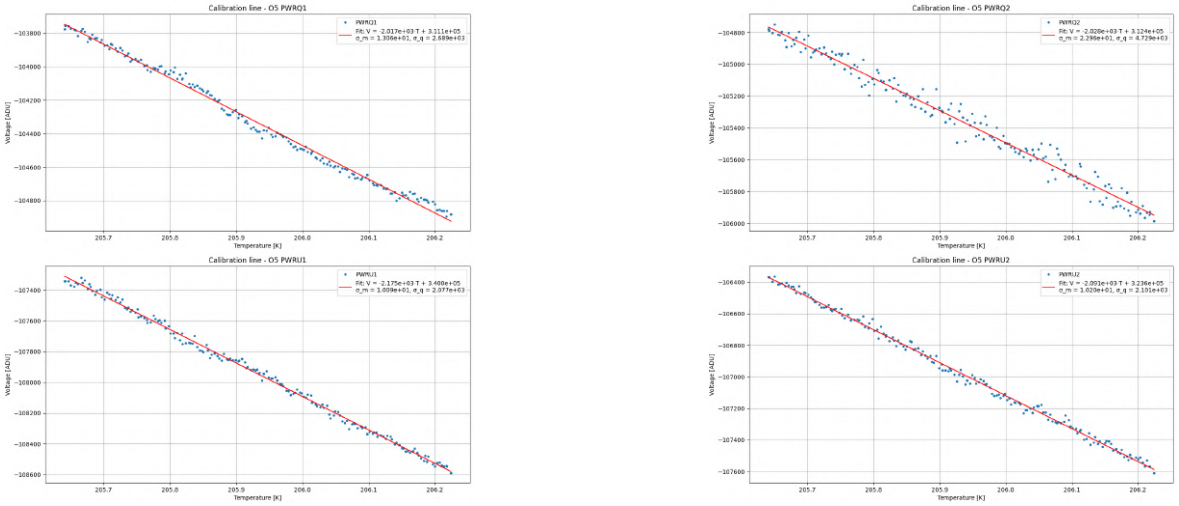

Board O, Polarimeter O5-Fit with 1 dataset: file 3		
Detector	**α [ADU/K]**	**T_n [K]**
Q1	-3488.9 ± 30.6	-173.2 ± 2.3
Q2	-3469.6 ± 63.1	-172.9 ± 4.7
U1	-3730.8 ± 28.9	-173.7 ± 2.0
U2	-3352.7 ± 33.5	-171.9 ± 2.6

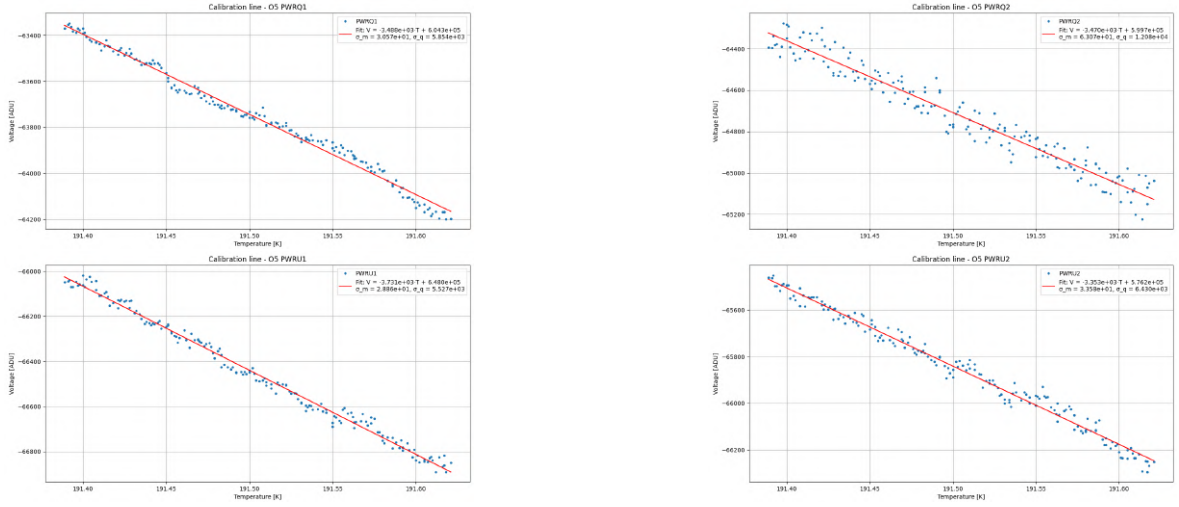

Board O, Polarimeter O5-Fit with 1 dataset: file 4		
Detector	**α [ADU/K]**	**T_n [K]**
Q1	-6133.8 ± 68.6	-178.9 ± 2.9
Q2	-5133.4 ± 190.0	-177.9 ± 0.5
U1	-5542.1 ± 69.8	-178.2 ± 3.2
U2	-5229.6 ± 92.0	-177.9 ± 4.5

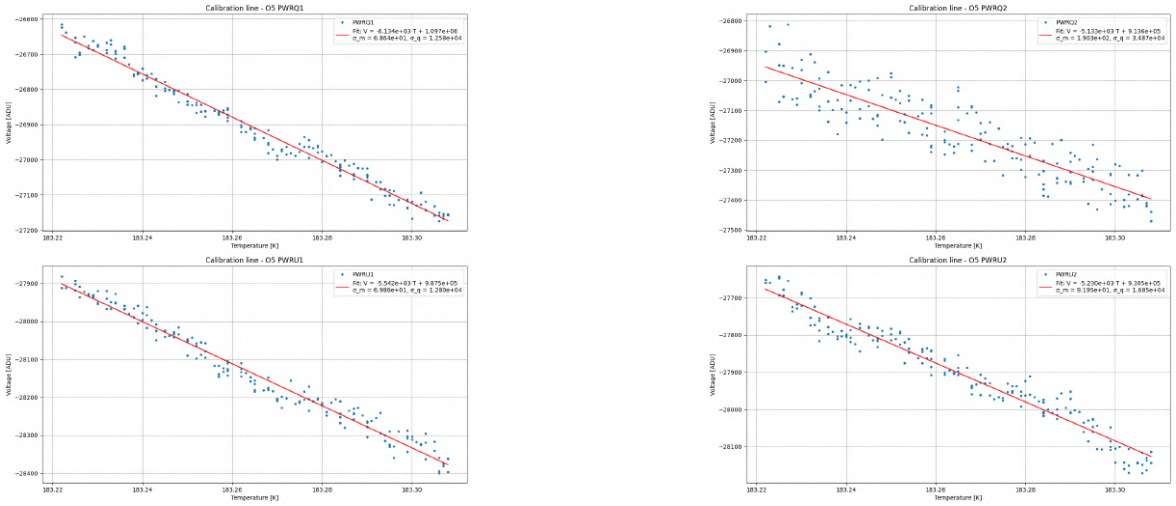

Board O, Polarimeter O5-Fit with 2 datasets: files 1,2		
Detector	**α [ADU/K]**	**T_n [K]**
Q1	-837.0 ± 0.4	-81.3 ± 0.1
Q2	-843.6 ± 0.4	-81.0 ± 0.1
U1	-862.1 ± 0.4	-80.7 ± 0.1
U2	-854.5 ± 0.4	-80.7 ± 0.1

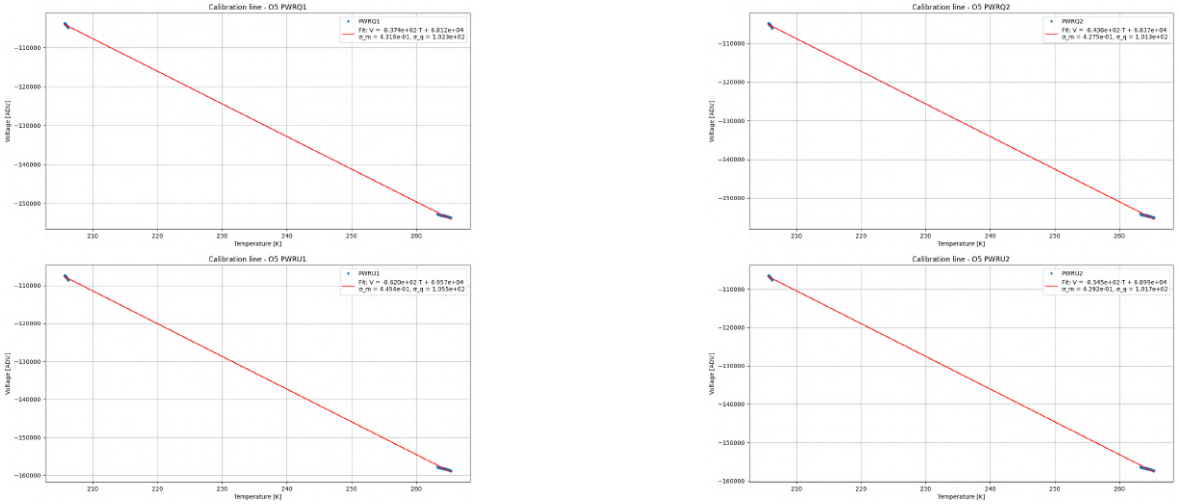

Board O, Polarimeter O5-Fit with 2 datasets: files 2,3		
Detector	α **[ADU/K]**	$\mathbf{T_n}$ **[K]**
Q1	-2812.1 ± 0.8	-168.8 ± 0.1
Q2	-2816.1 ± 0.8	-168.5 ± 0.1
U1	-2875.5 ± 0.7	-168.4 ± 0.1
U2	-2850.2 ± 0.7	-168.4 ± 0.1

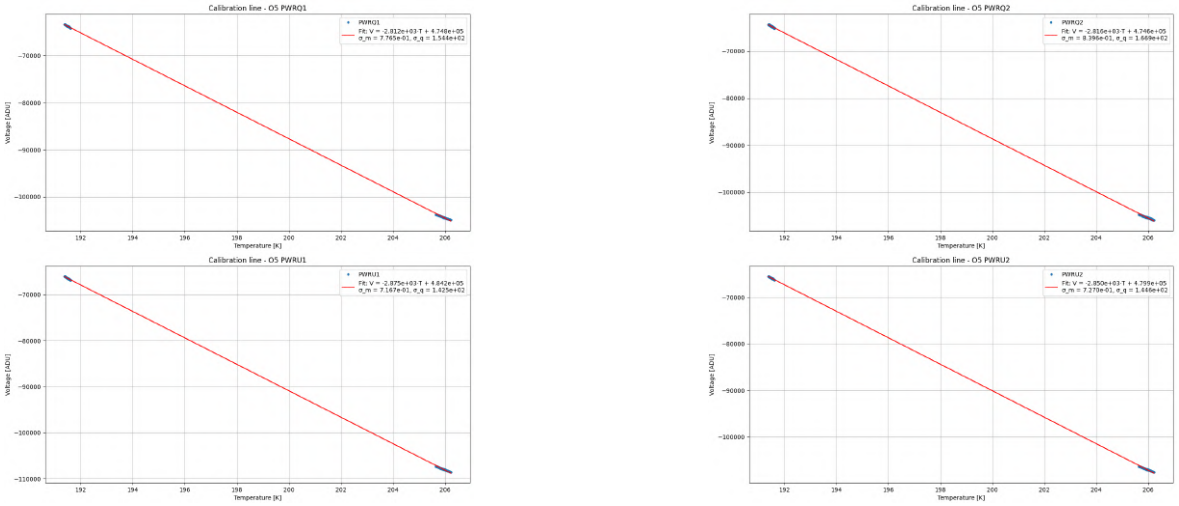

Board O, Polarimeter O5-Fit with 2 datasets: files 3,4		
Detector	α **[ADU/K]**	$\mathbf{T_n}$ **[K]**
Q1	-4472.0 ± 0.8	-177.3 ± 0.1
Q2	-4557.0 ± 1.0	-177.3 ± 0.1
U1	-4650.2 ± 0.7	-177.2 ± 0.1
U2	-4606.2 ± 0.9	-177.2 ± 0.1

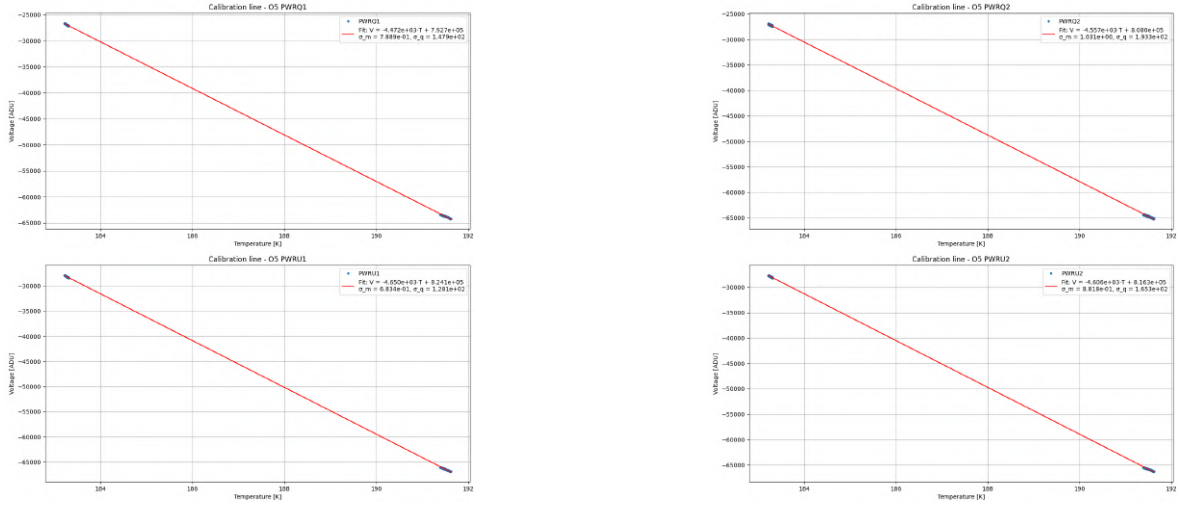

Board R	
File ID	**T_{board} [K]**
1	170.60
2	166.13
3	162.40
4	158.92

Table B.6: Table reporting the average temperature of the board for different data files.

Board R, Polarimeter R0		
Offset file name	**Time range (UTC)**	**Offset [ADU]**
`2025_10_09_13-44-12.h5`	14:03:00 - 14:13:00	**PWR Q1**= 211674.57
		PWR Q2= 200683.17
		PWR U1= 144307.81
		PWR U2= 155237.42

Table B.7: Table reporting the offset value considered for the detectors.

Board R: Polarimeter R0		
File ID	$\overline{\mathbf{T}}_{\mathbf{cal}}$ **[K]**	$\overline{\mathbf{V}}$ **[ADU]**
1	264.34	**PWR Q1**= −159181.74
		PWR Q2= −154316.87
		PWR U1= −152788.70
		PWR U2= −156360.00
2	205.93	**PWR Q1**= −108965.70
		PWR Q2= −104788.49
		PWR U1= −104397.34
		PWR U2= −107134.65
3	191.50	**PWR Q1**= −67899.68
		PWR Q2= −64365.44
		PWR U1= −65251.05
		PWR U2= −67398.52
4	183.27	**PWR Q1**= −29513.97
		PWR Q2= −27207.56
		PWR U1= −28758.03
		PWR U2= −30194.22

Table B.8: Table reporting the average temperatures of the observed calibrator subsystem and the related average values of the voltage output of the detectors, for the different data files.

Board R, Polarimeter R0-Fit with 4 datasets		
Detector	**α [ADU/K]**	**T_n [K]**
Q1	-1417.6 ± 20.7	-146.8 ± 3.8
Q2	-1392.3 ± 20.1	-148.3 ± 3.8
U1	-1357.5 ± 19.6	-146.6 ± 3.8
U2	-1380.5 ± 19.9	-145.8 ± 3.7

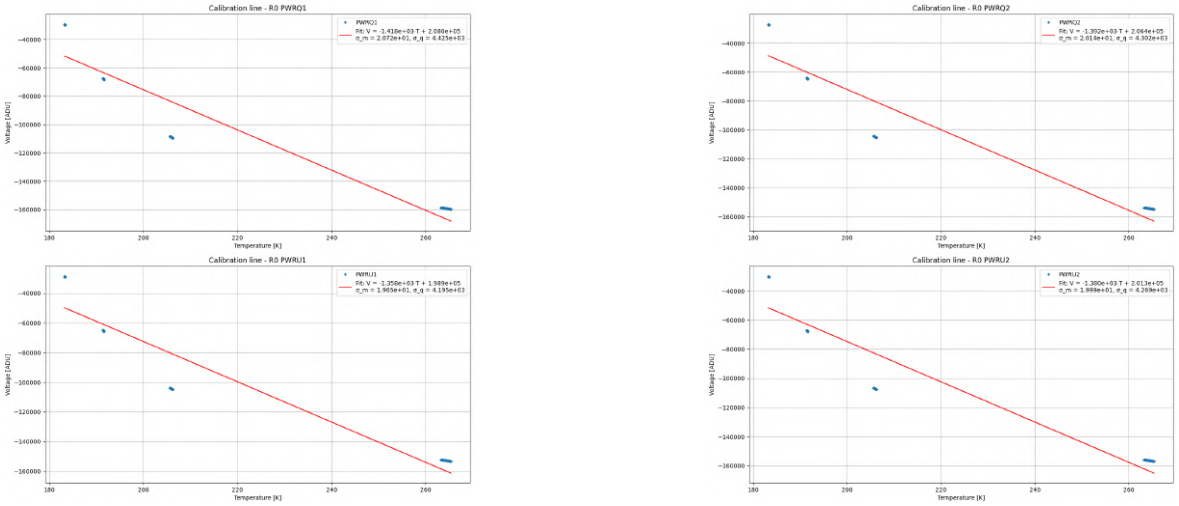

Board R, Polarimeter R0-Fit with 1 dataset: file 1		
Detector	**α [ADU/K]**	**T_n [K]**
Q1	-444.9 ± 3.5	93.5 ± 2.2
Q2	-437.5 ± 3.1	88.4 ± 2.0
U1	-427.2 ± 3.0	93.3 ± 2.0
U2	-442.2 ± 3.7	89.2 ± 2.3

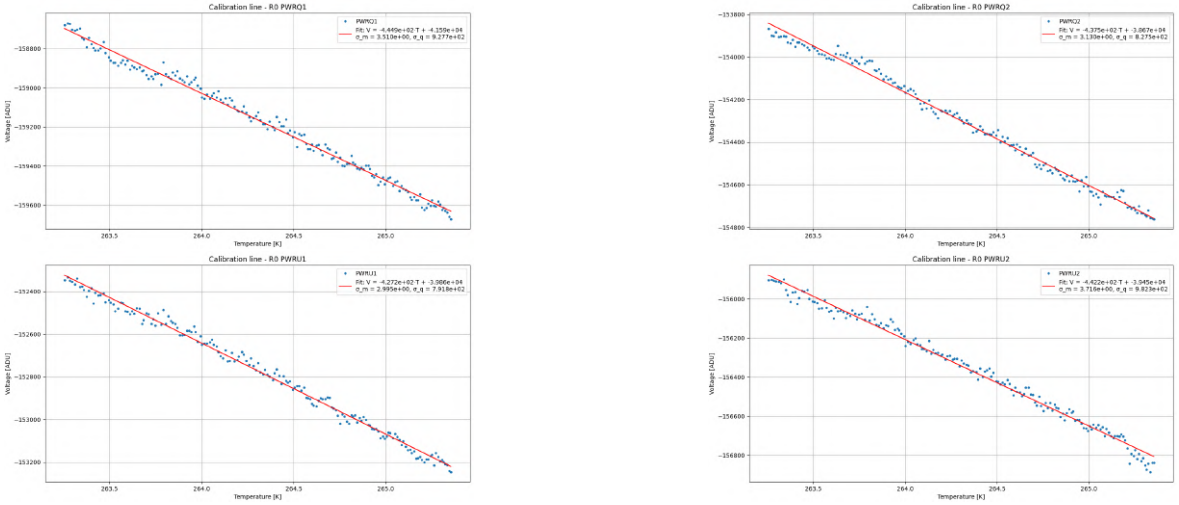

Board R, Polarimeter R0-Fit with 1 dataset: file 2		
Detector	**α [ADU/K]**	**T_n [K]**
Q1	-2030.0 ± 11.5	-152.3 ± 1.5
Q2	-1970.5 ± 10.4	-152.8 ± 1.4
U1	-1881.2 ± 9.5	-150.4 ± 1.3
U2	-1924.1 ± 9.5	-150.3 ± 1.3

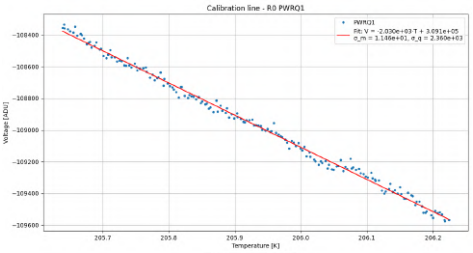

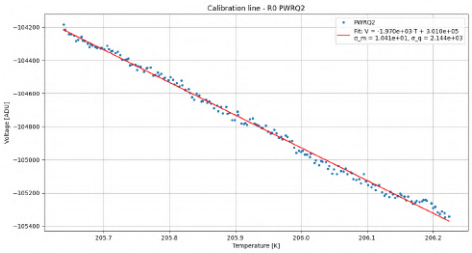

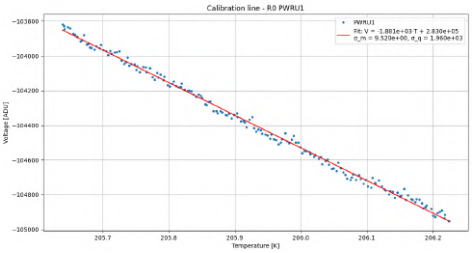

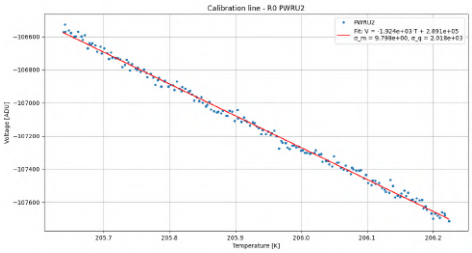

Board R, Polarimeter R0-Fit with 1 dataset: file 3		
Detector	**α [ADU/K]**	**T_n [K]**
Q1	-3492.9 ± 29.7	-172.1 ± 2.2
Q2	-3547.9 ± 24.3	-173.4 ± 1.6
U1	-3442.8 ± 24.3	-172.6 ± 1.8
U2	-3690.9 ± 25.1	-173.2 ± 1.8

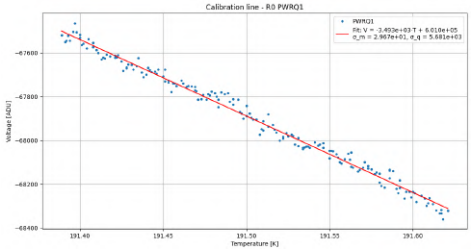

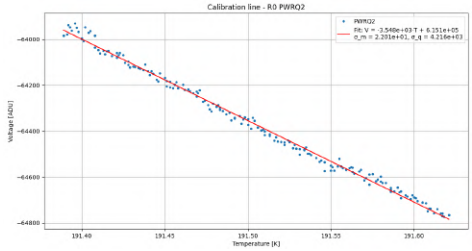

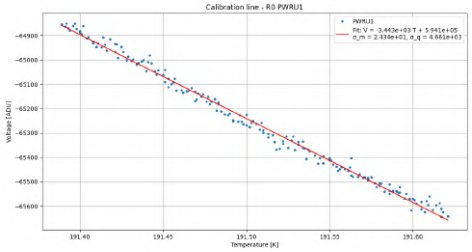

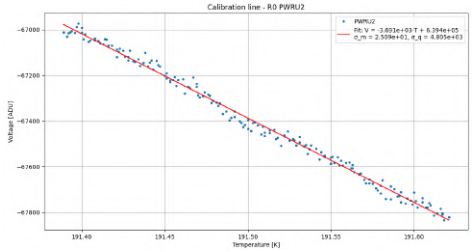

Board R, Polarimeter R0-Fit with 1 dataset: file 4		
Detector	**α [ADU/K]**	**T_n [K]**
Q1	-5206.9 ± 87.2	-177.6 ± 4.3
Q2	-5537.0 ± 55.2	-178.4 ± 2.2
U1	-4685.0 ± 69.0	-177.1 ± 3.8
U2	-5376.3 ± 63.7	-177.6 ± 3.0

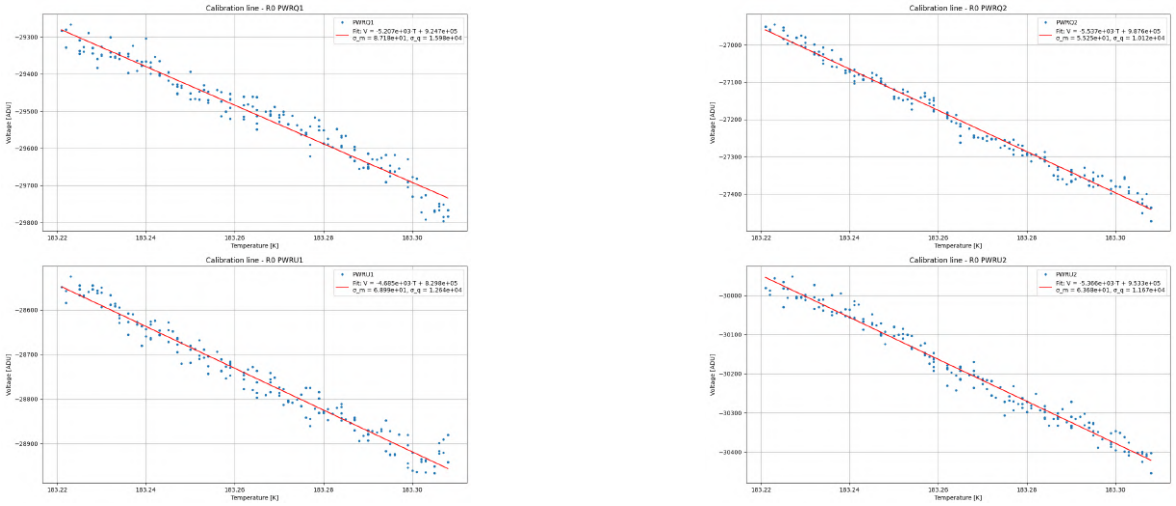

Board R, Polarimeter R0-Fit with 2 datasets: files 1,2		
Detector	**α [ADU/K]**	**T_n [K]**
Q1	-859.5 ± 0.4	-79.2 ± 0.1
Q2	-847.8 ± 0.4	-82.3 ± 0.1
U1	-828.3 ± 0.4	-79.9 ± 0.1
U2	-842.5 ± 0.4	-78.8 ± 0.1

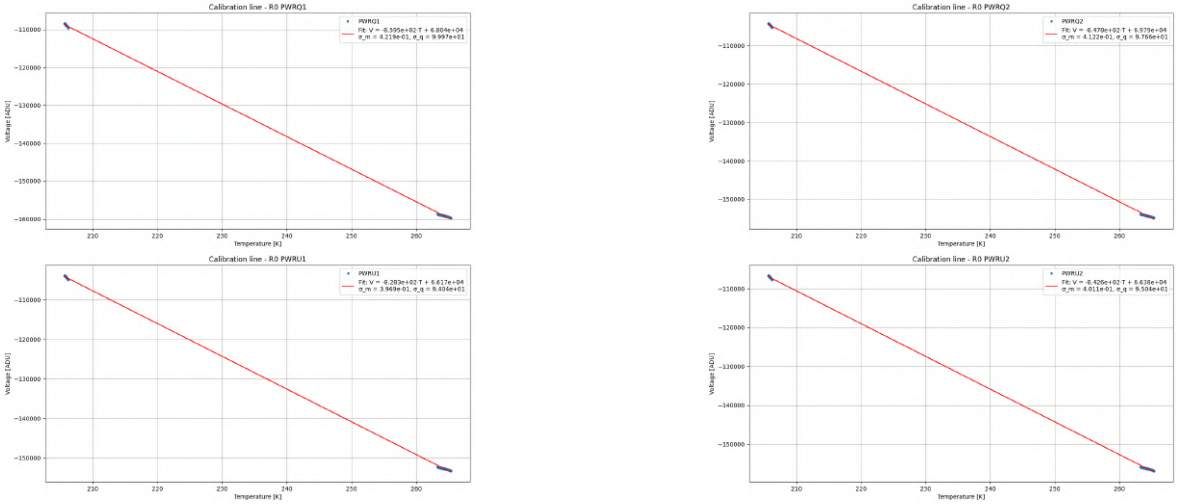

Board R, Polarimeter R0-Fit with 2 datasets: files 2,3		
Detector	α **[ADU/K]**	$\mathbf{T_n}$ **[K]**
Q1	-2846.4 ± 0.8	-167.7 ± 0.1
Q2	-2801.9 ± 0.8	-168.5 ± 0.1
U1	-2713.4 ± 0.8	-167.5 ± 0.1
U2	-2754.0 ± 0.8	-167.0 ± 0.1

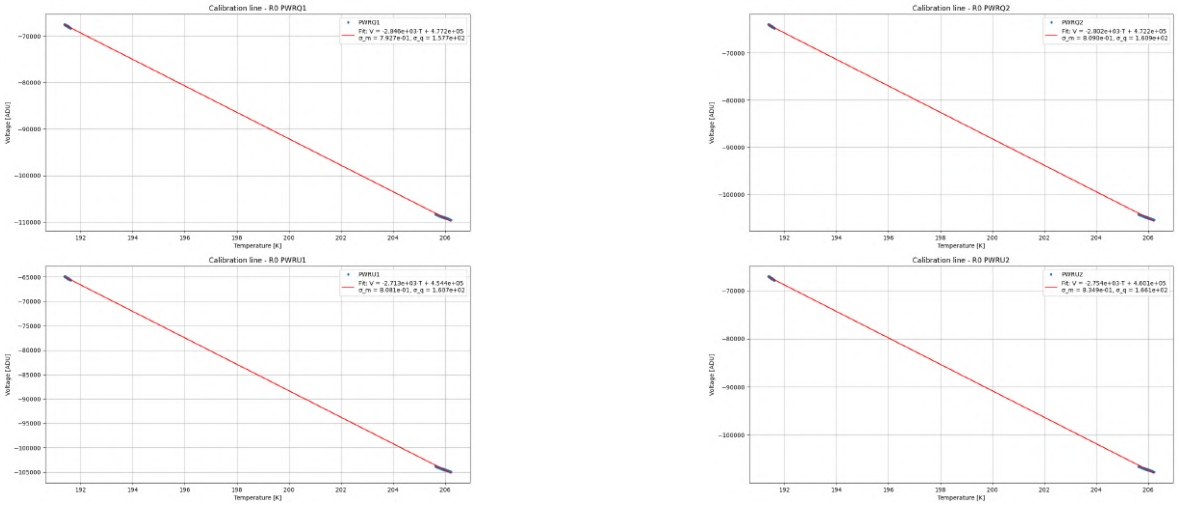

Board R, Polarimeter R0-Fit with 2 datasets: files 3,4		
Detector	α **[ADU/K]**	$\mathbf{T_n}$ **[K]**
Q1	-4659.7 ± 0.8	-176.9 ± 0.1
Q2	-4510.7 ± 0.7	-177.2 ± 0.1
U1	-4429.9 ± 0.7	-176.8 ± 0.1
U2	-4516.4 ± 0.6	-176.6 ± 0.1

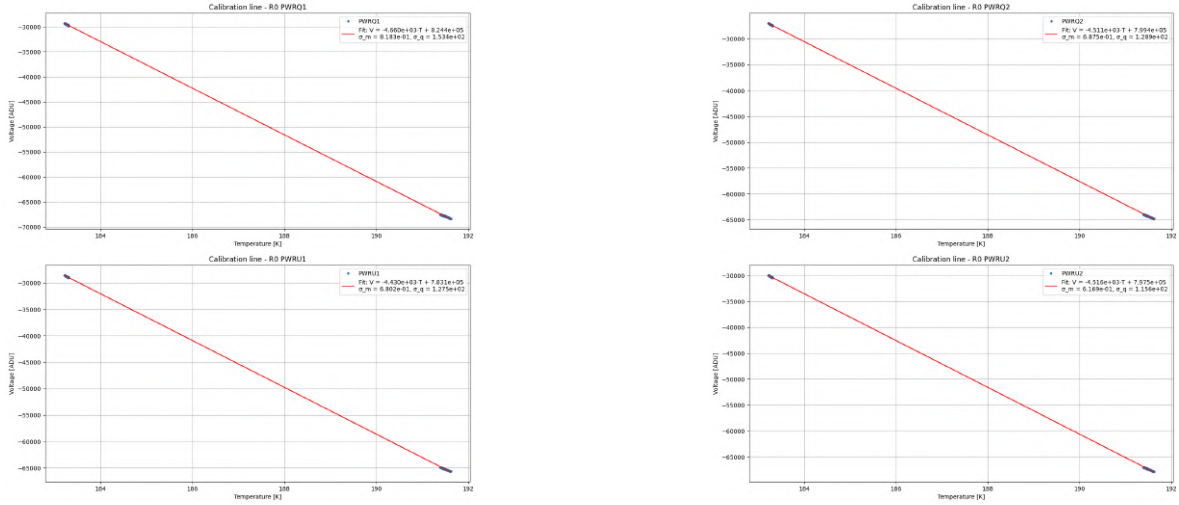

Board R, Polarimeter R6		
Offset file name	**Time range (UTC)**	**Offset [ADU]**
2025_10_09_13-44-12.h5	14:03:00 - 14:13:00	**PWR Q1**= 244860.21
		PWR Q2= 233907.75
		PWR U1= 239475.42
		PWR U2= 235730.19

Table B.9: Table reporting the offset value considered for the detectors.

Board R: Polarimeter R6		
File ID	$\overline{\mathbf{T}}_{\mathbf{cal}}$ **[K]**	$\overline{\mathbf{V}}$ **[ADU]**
1	264.34	**PWR Q1**= −170142.52
		PWR Q2= −174730.71
		PWR U1= −182920.26
		PWR U2= −173484.55
2	205.93	**PWR Q1**= −119638.99
		PWR Q2= −122734.39
		PWR U1= −130708.97
		PWR U2= −122051.64
3	191.50	**PWR Q1**= −79720.60
		PWR Q2= −81569.89
		PWR U1= −90614.42
		PWR U2= −81568.47
4	183.27	**PWR Q1**= −42966.23
		PWR Q2= −43654.31
		PWR U1= −53749.05
		PWR U2= −44280.04

Table B.10: Table reporting the average temperatures of the observed calibrator subsystem and the related average values of the voltage output of the detectors, for the different data files.

Board R, Polarimeter R6-Fit with 4 datasets		
Detector	**α [ADU/K]**	**T_n [K]**
Q1	-1396.7 ± 19.7	-137.4 ± 3.6
Q2	-1422.1 ± 19.6	-130.8 ± 3.5
U1	-1422.2 ± 19.6	-130.8 ± 3.5
U2	-1419.4 ± 19.9	-137.0 ± 3.6

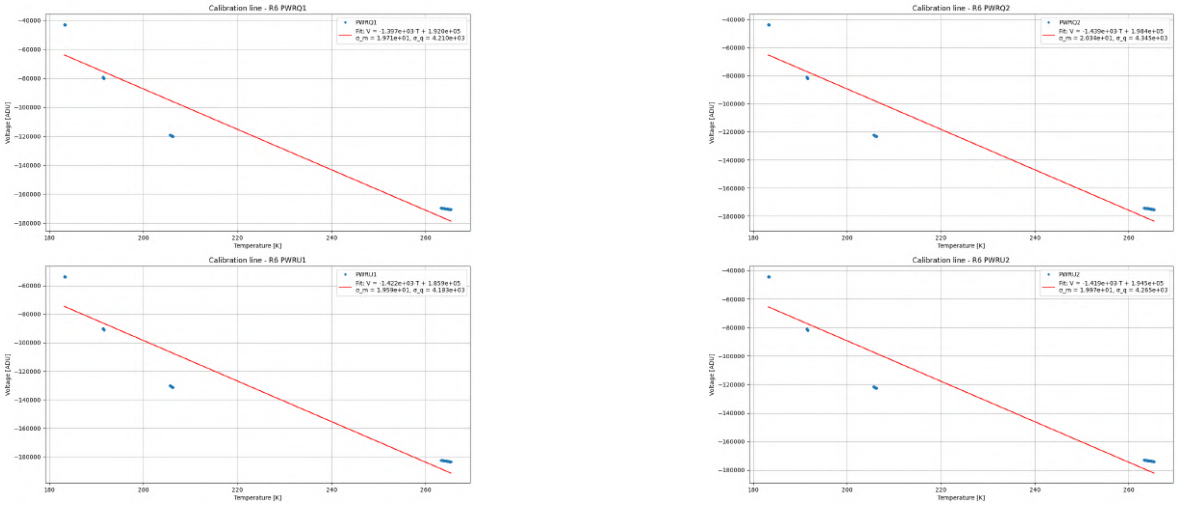

Board R, Polarimeter R6-Fit with 1 dataset: file 1		
Detector	**α [ADU/K]**	**T_n [K]**
Q1	-429.6 ± 4.4	131.7 ± 3.0
Q2	-459.3 ± 4.3	116.1 ± 2.7
U1	-498.5 ± 4.8	102.6 ± 2.7
U2	-458.2 ± 3.0	114.3 ± 1.9

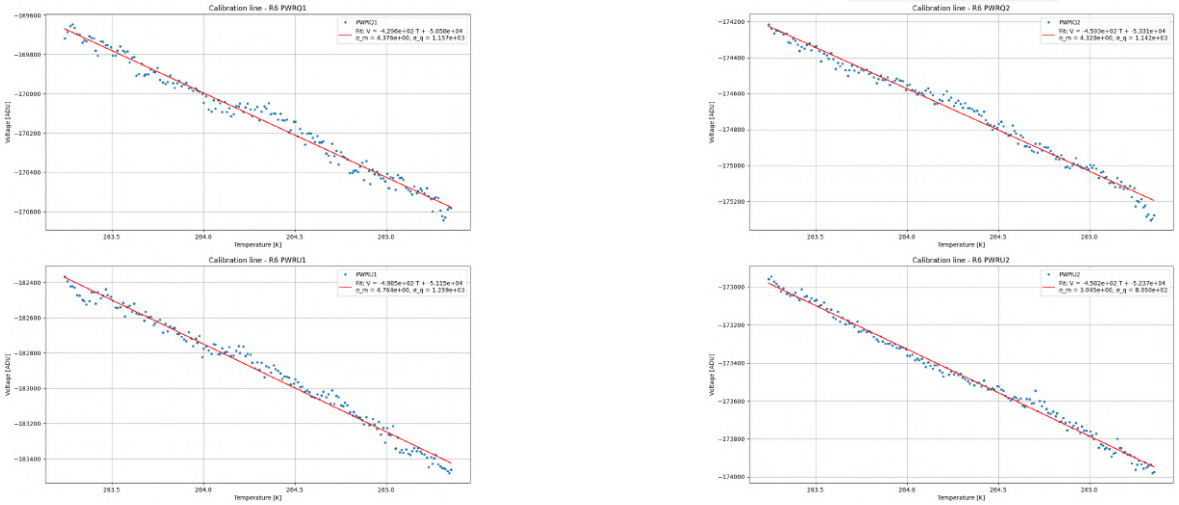

Board R, Polarimeter R6-Fit with 1 dataset: file 2		
Detector	**α [ADU/K]**	**T_n [K]**
Q1	-2085.9 ± 13.6	-148.6 ± 1.7
Q2	-1955.8 ± 11.5	-143.2 ± 1.5
U1	-2007.2 ± 13.3	-140.8 ± 1.7
U2	-2073.0 ± 9.2	-147.0 ± 1.1

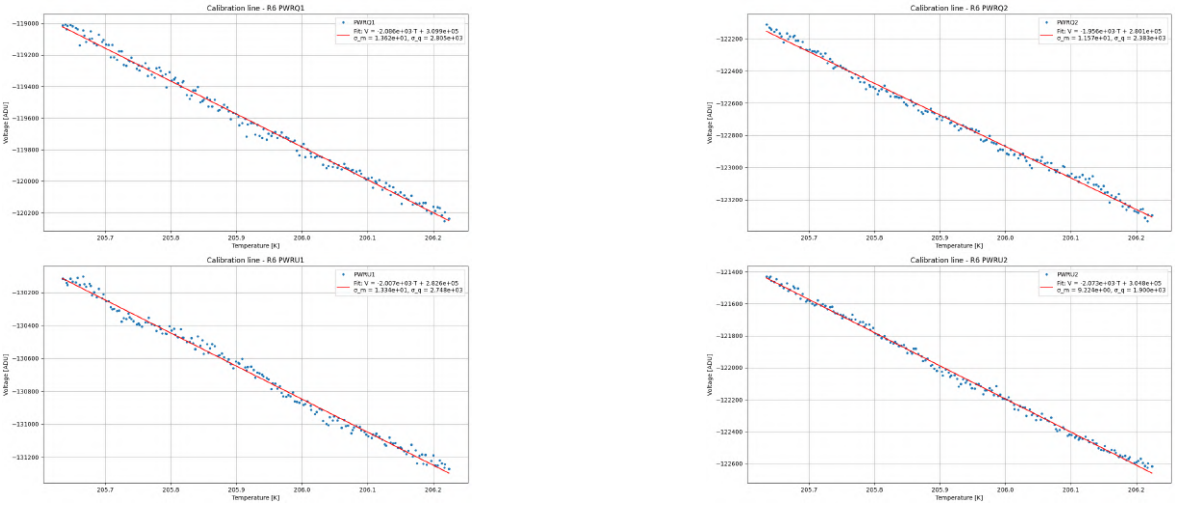

Board R, Polarimeter R6-Fit with 1 dataset: file 3		
Detector	**α [ADU/K]**	**T_n [K]**
Q1	-3562.1 ± 33.4	-169.1 ± 2.4
Q2	-4072.0 ± 21.1	-171.5 ± 1.3
U1	-3945.1 ± 32.3	-168.5 ± 2.1
U2	-3511.2 ± 20.1	-168.3 ± 1.5

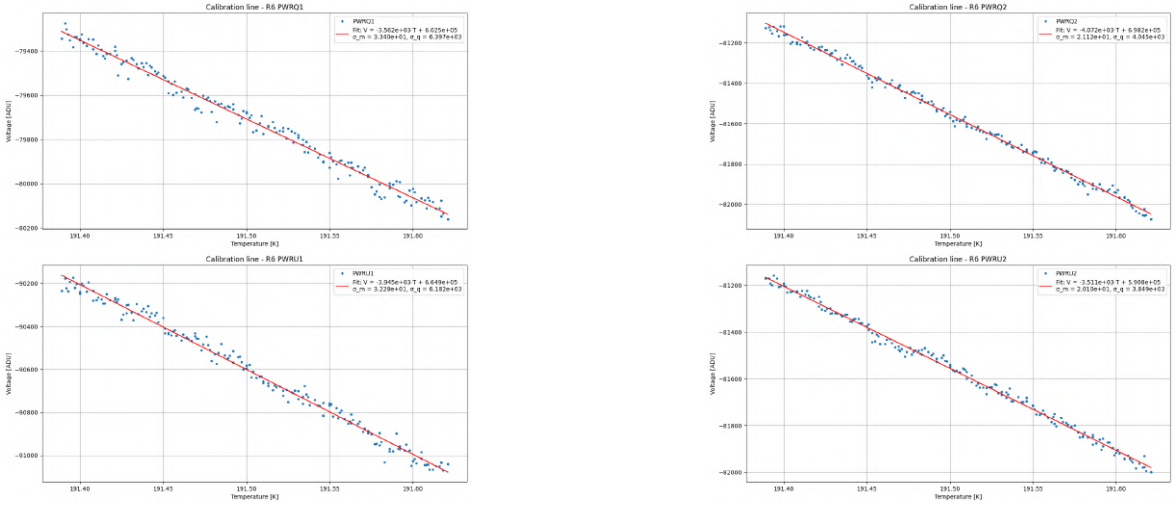

Board R, Polarimeter R6-Fit with 1 dataset: file 4		
Detector	**α [ADU/K]**	**T_n [K]**
Q1	-5330.3 ± 105.0	-175.2 ± 5.0
Q2	-5088.2 ± 75.1	-174.7 ± 3.7
U1	-5820.9 ± 87.3	-174.0 ± 3.8
U2	-5430.0 ± 62.2	-175.1 ± 2.9

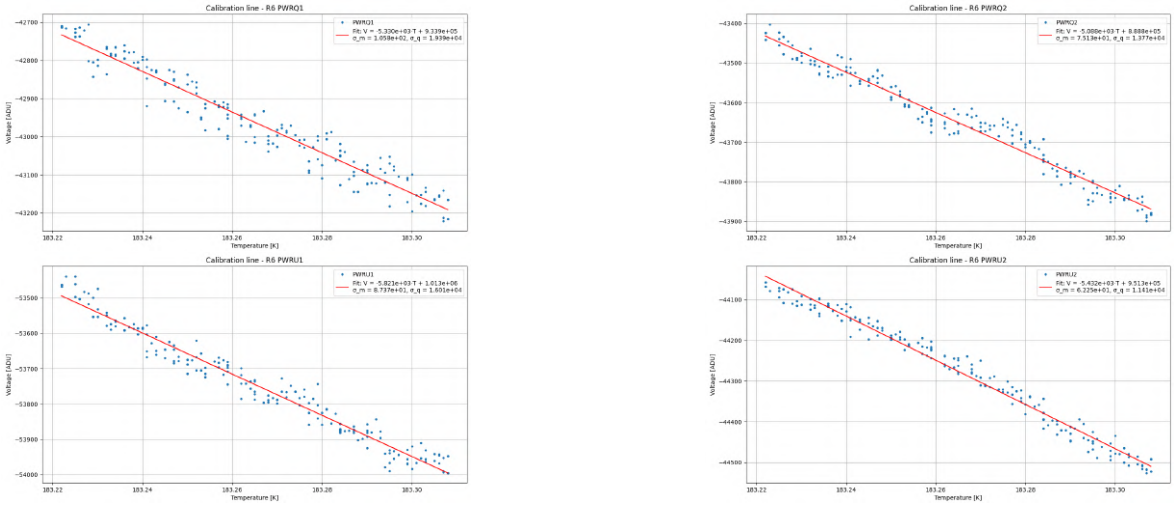

Board R, Polarimeter R6-Fit with 2 datasets: files 1,2		
Detector	**α [ADU/K]**	**T_n [K]**
Q1	-864.5 ± 0.4	-67.6 ± 0.1
Q2	-890.1 ± 0.4	-68.0 ± 0.1
U1	-894.0 ± 0.4	-59.7 ± 0.1
U2	-880.1 ± 0.4	-67.3 ± 0.1

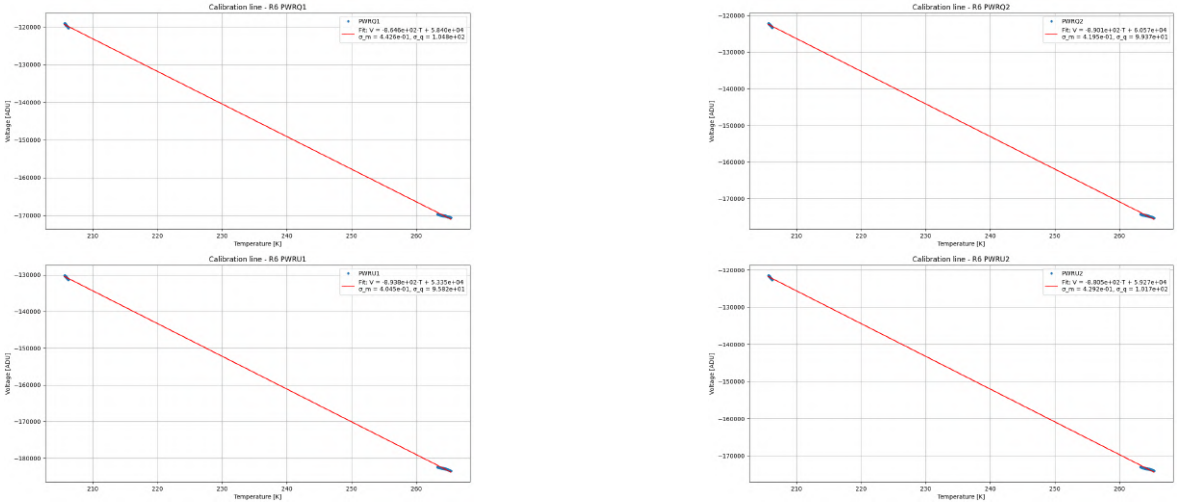

Board R, Polarimeter R6-Fit with 2 datasets: files 2,3		
Detector	**α [ADU/K]**	**T_n [K]**
Q1	-2766.8 ± 0.7	-162.7 ± 0.1
Q2	-2853.2 ± 0.9	-162.9 ± 0.1
U1	-2779.5 ± 0.8	-158.9 ± 0.1
U2	-2810.0 ± 0.7	-162.4 ± 0.1

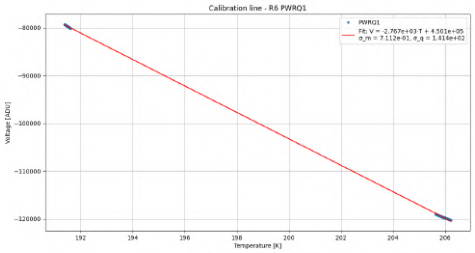

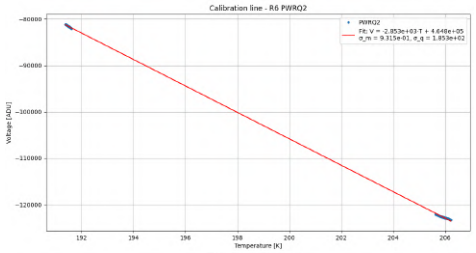

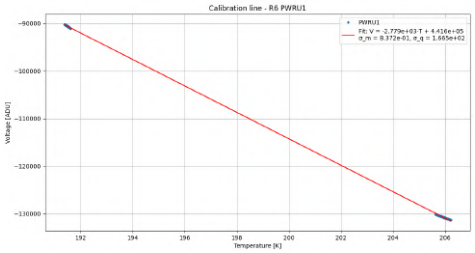

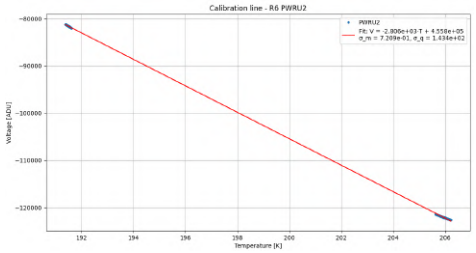

Board R, Polarimeter R6-Fit with 2 datasets: files 3,4		
Detector	**α [ADU/K]**	**T_n [K]**
Q1	-4461.1 ± 0.7	-173.6 ± 0.1
Q2	-4602.5 ± 0.5	-173.8 ± 0.1
U1	-4475.0 ± 0.6	-171.3 ± 0.1
U2	-4526.0 ± 0.7	-173.5 ± 0.1

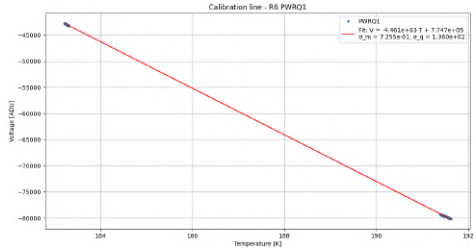

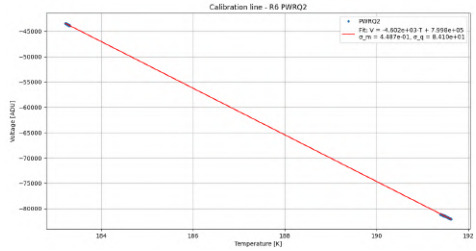

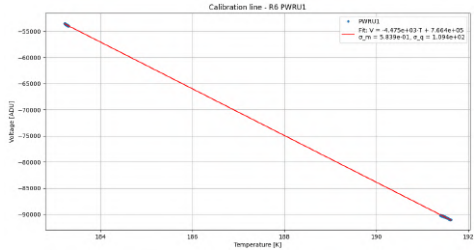

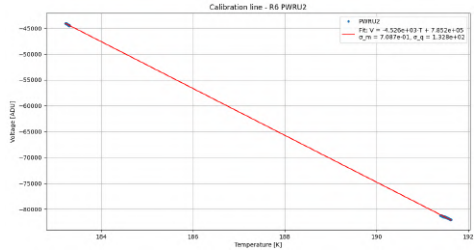

Board I	
File ID	**T_{board} [K]**
1	171.08
2	166.59
3	162.85
4	159.34

Table B.11: Table reporting the average temperature of the board for different data files.

Board I, Polarimeter I1		
Offset file name	**Time range (UTC)**	**Offset [ADU]**
`2025_10_09_13-44-12.h5`	14:03:00 - 14:13:00	**PWR Q1**= 210874.69
		PWR Q2= 212571.33
		PWR U1= 235959.37
		PWR U2= 211888.00

Table B.12: Table reporting the offset value considered for the detectors.

Board I: Polarimeter I1		
File ID	$\overline{\mathbf{T}}_{\mathbf{cal}}$ **[K]**	$\overline{\mathbf{V}}$ **[ADU]**
1	263.93	**PWR Q1**= −158925.52
		PWR Q2= −155078.83
		PWR U1= −158870.04
		PWR U2= −158258.16
2	190.33	**PWR Q1**= −109098.08
		PWR Q2= −106500.54
		PWR U1= −109205.82
		PWR U2= −108746.13
3	175.56	**PWR Q1**= −68789.85
		PWR Q2= −66716.35
		PWR U1= −69637.45
		PWR U2= −68710.65
4	165.84	**PWR Q1**= −31127.17
		PWR Q2= −29634.98
		PWR U1= −32240.82
		PWR U2= −31248.39

Table B.13: Table reporting the average temperatures of the observed calibrator subsystem and the related average values of the voltage output of the detectors, for the different data files.

Board I, Polarimeter I1-Fit with 4 datasets		
Detector	**α [ADU/K]**	**T_n [K]**
Q1	-1137.9 ± 17.9	-118.1 ± 3.7
Q2	-1116.0 ± 17.7	-118.7 ± 3.7
U1	-1127.6 ± 17.7	-116.9 ± 3.7
U2	-1130.7 ± 17.8	117.8 ± 3.7

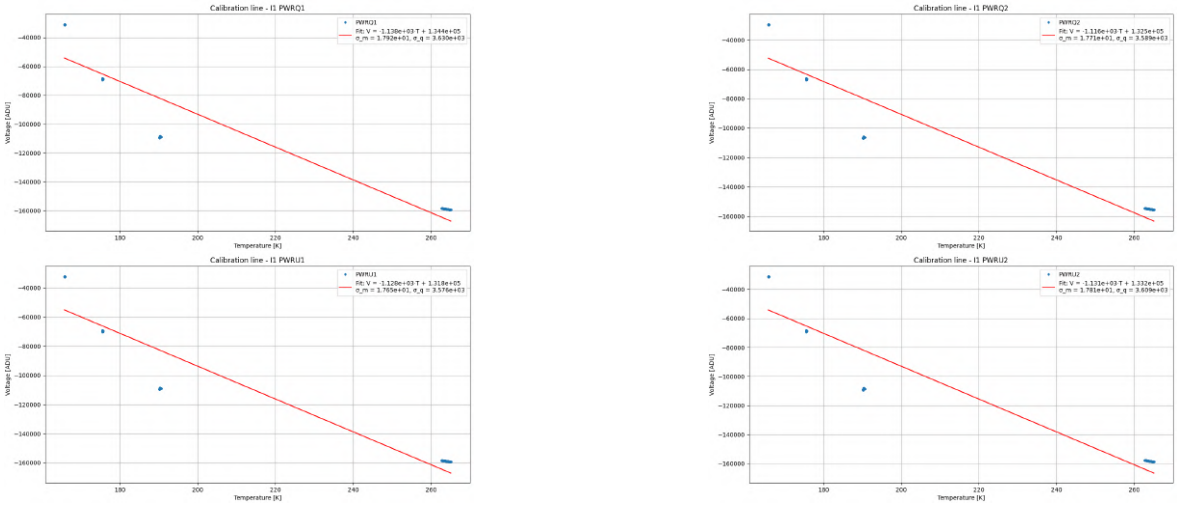

Board I, Polarimeter I1-Fit with 1 dataset: file 1		
Detector	**α [ADU/K]**	**T_n [K]**
Q1	-410.1 ± 2.4	123.6 ± 1.7
Q2	-319.8 ± 3.7	131.9 ± 2.8
U1	-359.7 ± 4.0	177.7 ± 3.5
U2	-424.9 ± 2.9	108.5 ± 2.0

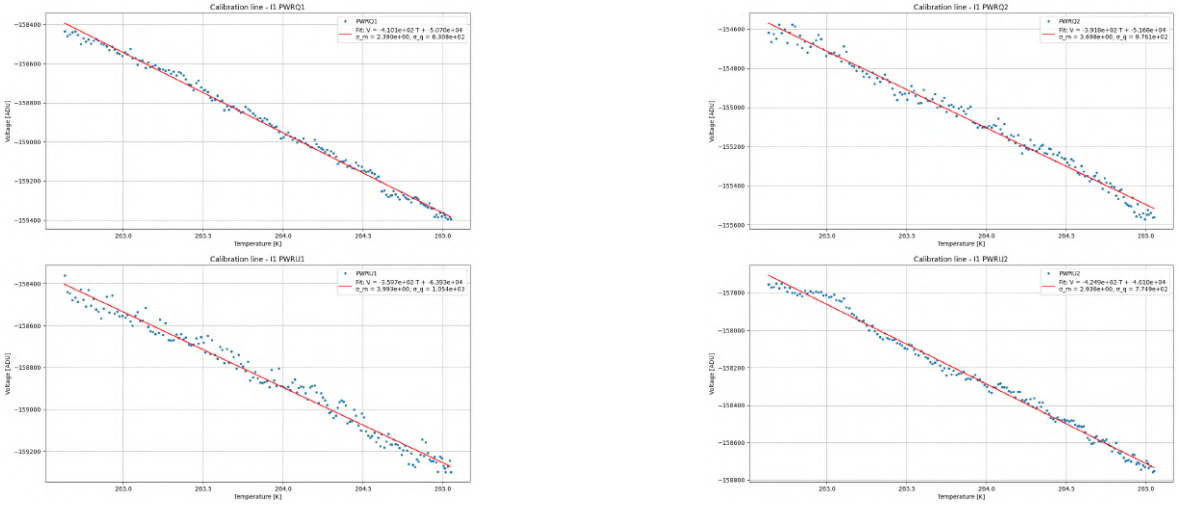

Board I, Polarimeter I1-Fit with 1 dataset: file 2		
Detector	**α [ADU/K]**	**T_n [K]**
Q1	1818.1 ± 152.0	-250.3 ± 26.3
Q2	1659.3 ± 132.2	-254.5 ± 25.3
U1	1852.7 ± 143.4	-249.3 ± 24.3
U2	1963.5 ± 155.0	-245.7 ± 24.7

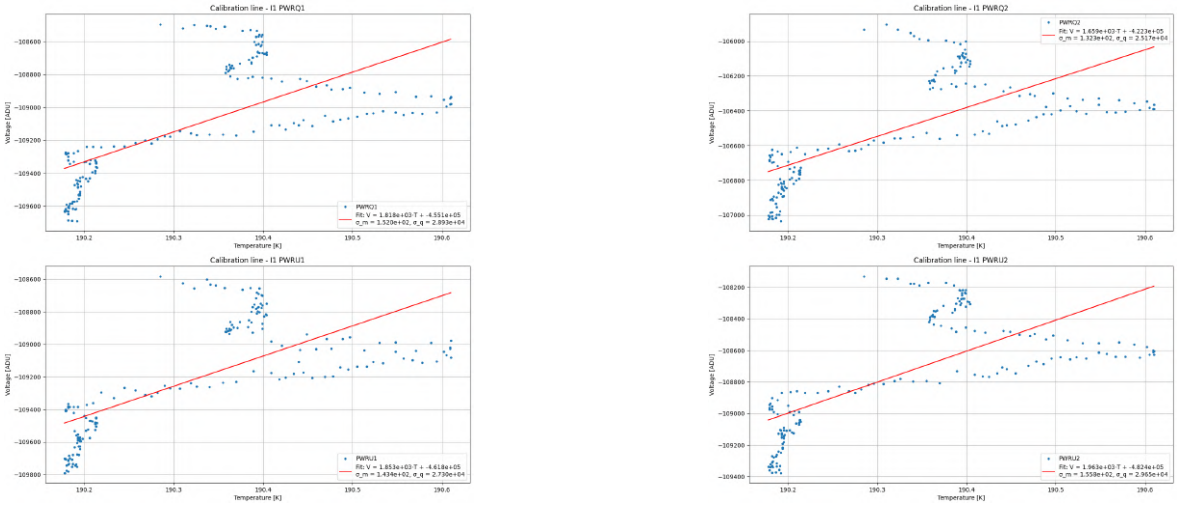

Board I, Polarimeter I1-Fit with 1 dataset: file 3		
Detector	**α [ADU/K]**	**T_n [K]**
Q1	-2275.4 ± 402.6	-145.3 ± 40.3
Q2	-2615.7 ± 379.0	-150.1 ± 33.5
U1	-2517.2 ± 394.3	-147.9 ± 36.0
U2	-2102.5 ± 353.7	-142.9 ± 38.1

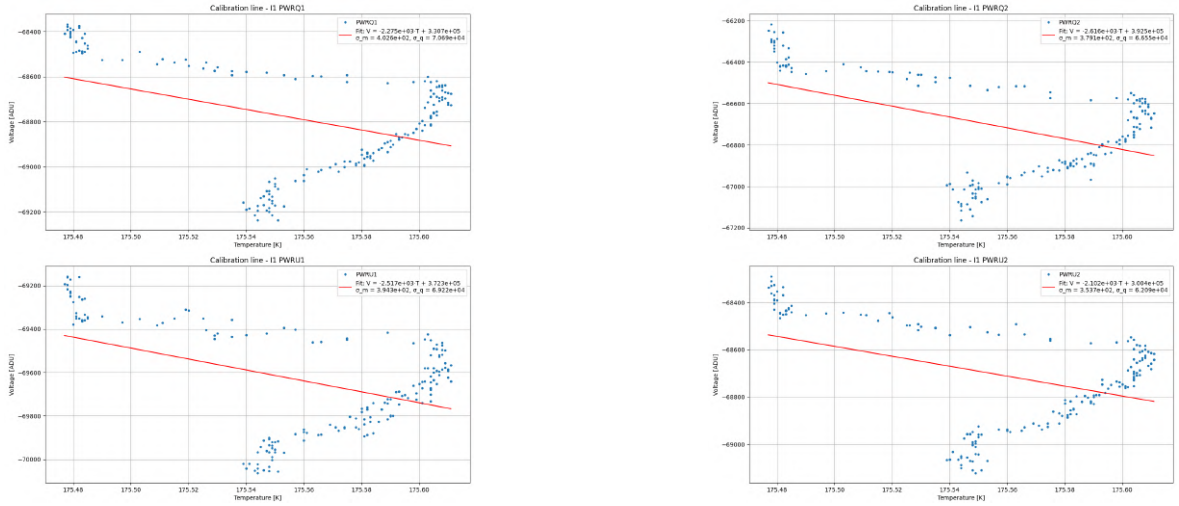

Board I, Polarimeter I1-Fit with 1 dataset: file 4		
Detector	**α [ADU/K]**	**T_n [K]**
Q1	-6012.3 ± 54.3	-160.7 ± 4.5
Q2	-5202.2 ± 105.6	-160.1 ± 4.7
U1	-5256.6 ± 96.1	-159.7 ± 4.2
U2	-4797.4 ± 58.6	-159.3 ± 2.8

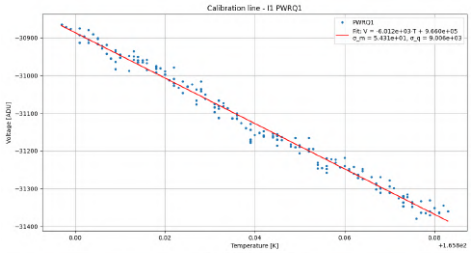

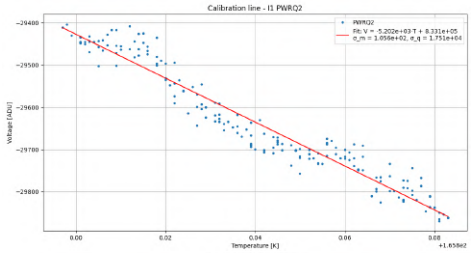

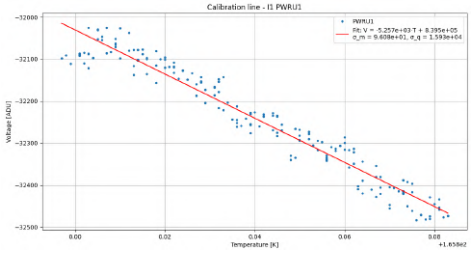

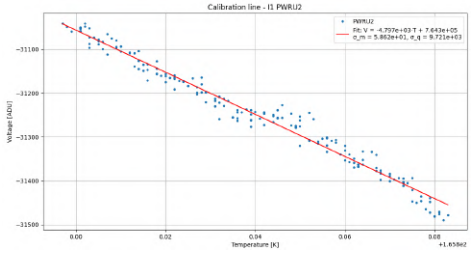

Board I, Polarimeter I1-Fit with 2 datasets: files 1,2		
Detector	**α [ADU/K]**	**T_n [K]**
Q1	-676.9 ± 0.5	-29.2 ± 0.2
Q2	-659.9 ± 0.4	-28.9 ± 0.2
U1	-675.6 ± 0.5	-28.5 ± 0.2
U2	-672.6 ± 0.5	-28.7 ± 0.2

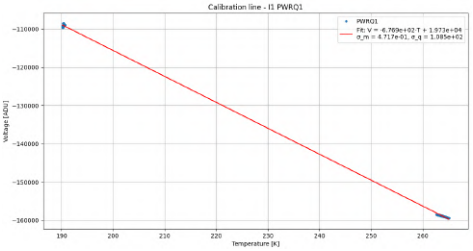

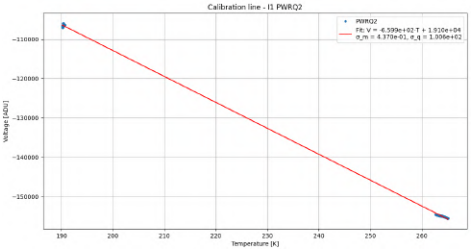

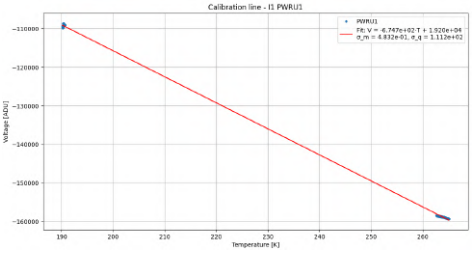

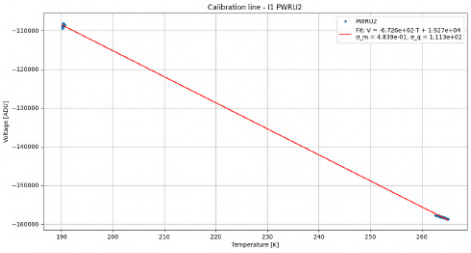

Board I, Polarimeter I1-Fit with 2 datasets: files 2,3		
Detector	α **[ADU/K]**	$\mathbf{T_n}$ **[K]**
Q1	-2729.1 ± 3.5	-150.4 ± 0.3
Q2	-2693.3 ± 3.3	-150.8 ± 0.3
U1	-2679.8 ± 3.5	-149.6 ± 0.3
U2	-2710.5 ± 3.6	-150.2 ± 0.3

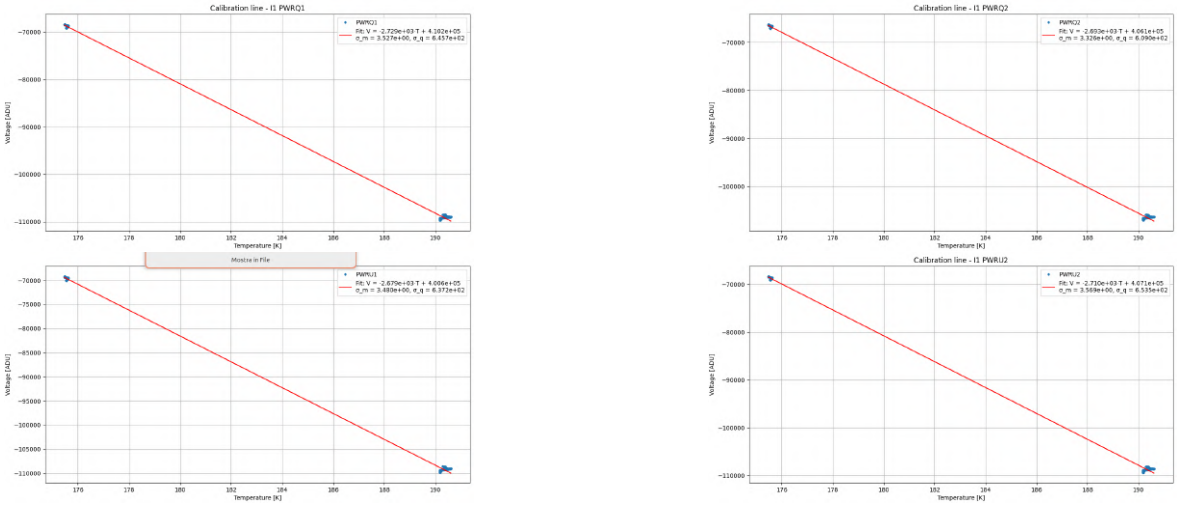

Board I, Polarimeter I1-Fit with 2 datasets: files 3,4		
Detector	α **[ADU/K]**	$\mathbf{T_n}$ **[K]**
Q1	-3875.4 ± 1.9	-157.8 ± 0.1
Q2	-3815.1 ± 1.8	-158.1 ± 0.1
U1	-3847.6 ± 1.8	-157.5 ± 0.1
U2	-3854.2 ± 1.7	-157.7 ± 0.1

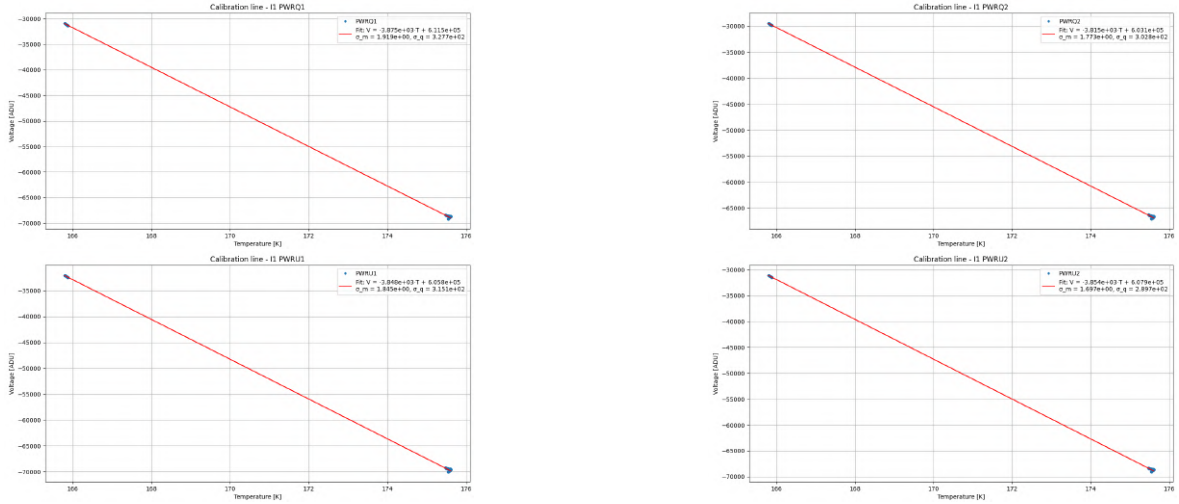

Board I, Polarimeter I6		
Offset file name	**Time range (UTC)**	**Offset [ADU]**
`2025_10_09_13-44-12.h5`	14:03:00 - 14:13:00	**PWR Q1**= 214664.47
		PWR Q2= 212987.21
		PWR U1= 218376.32
		PWR U2= 220127.45

Table B.14: Table reporting the offset value considered for the detectors.

Board I: Polarimeter I6		
File ID	$\overline{\mathbf{T}}_{\mathbf{cal}}$ **[K]**	$\overline{\mathbf{V}}$ **[ADU]**
1	272.37	**PWR Q1**= −155374.60
		PWR Q2= −154683.58
		PWR U1= −162137.12
		PWR U2= −156160.08
2	139.34	**PWR Q1**= −107481.02
		PWR Q2= −106228.19
		PWR U1= −112336.43
		PWR U2= −108274.56
3	96.43	**PWR Q1**= −68170.07
		PWR Q2= −66690.77
		PWR U1= −71619.73
		PWR U2= −68985.74
4	72.78	**PWR Q1**= −31474.40
		PWR Q2= −30044.76
		PWR U1= −33509.92
		PWR U2= −32505.34

Table B.15: Table reporting the average temperatures of the observed calibrator subsystem and the related average values of the voltage output of the detectors, for the different data files.

Board I, Polarimeter I6-Fit with 4 datasets		
Detector	**α [ADU/K]**	**T_n [K]**
Q1	-567.1 ± 7.0	14.6 ± 2.0
Q2	-571.1 ± 7.0	11.3 ± 2.0
U1	-588.7 ± 7.3	15.9 ± 2.0
U2	-566.3 ± 7.0	16.3 ± 2.0

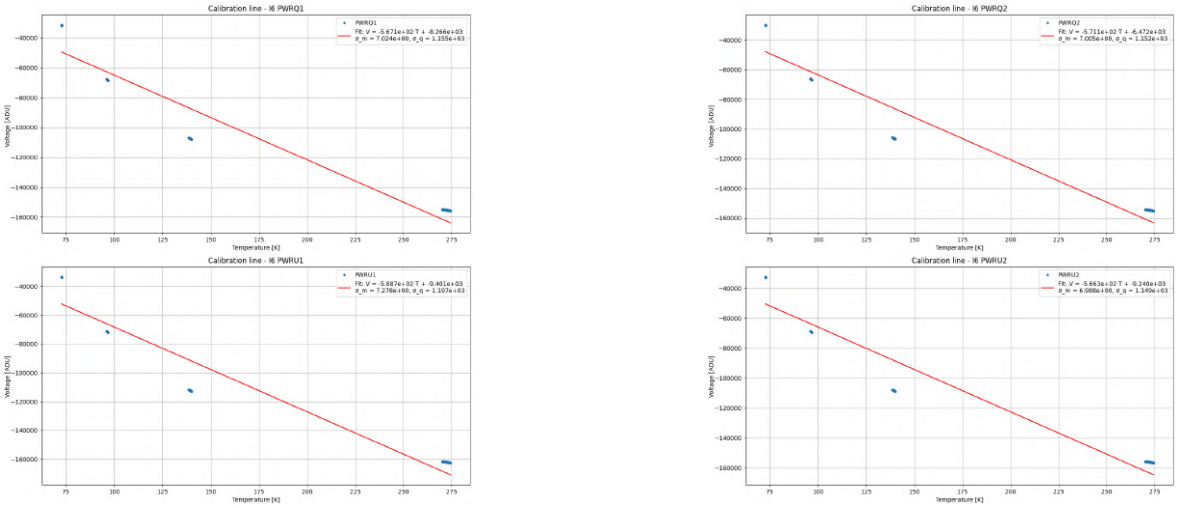

Board I, Polarimeter I6-Fit with 1 dataset: file 1		
Detector	**α [ADU/K]**	**T_n [K]**
Q1	-210.6 ± 1.9	465.4 ± 4.9
Q2	-224.2 ± 1.8	417.7 ± 3.9
U1	-218.1 ± 2.5	471.1 ± 6.2
U2	-220.5 ± 2.1	435.8 ± 4.9

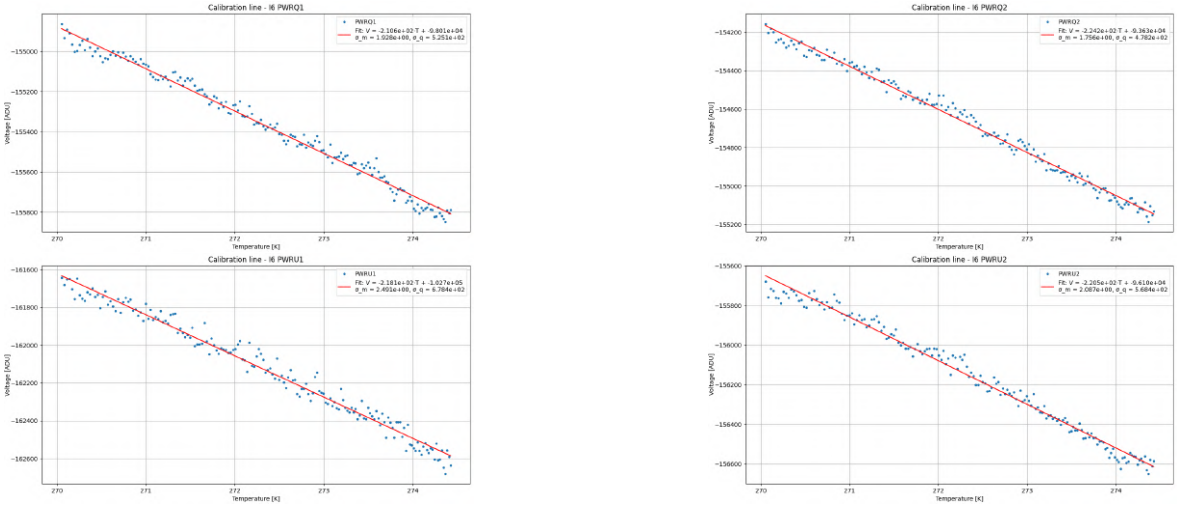

Board I, Polarimeter I6-Fit with 1 dataset: file 2		
Detector	**α [ADU/K]**	**T_n [K]**
Q1	-728.0 ± 4.1	8.3 ± 0.8
Q2	-735.7 ± 3.4	5.0 ± 0.7
U1	-757.5 ± 7.2	9.0 ± 1.3
U2	-736.1 ± 5.1	7.7 ± 1.0

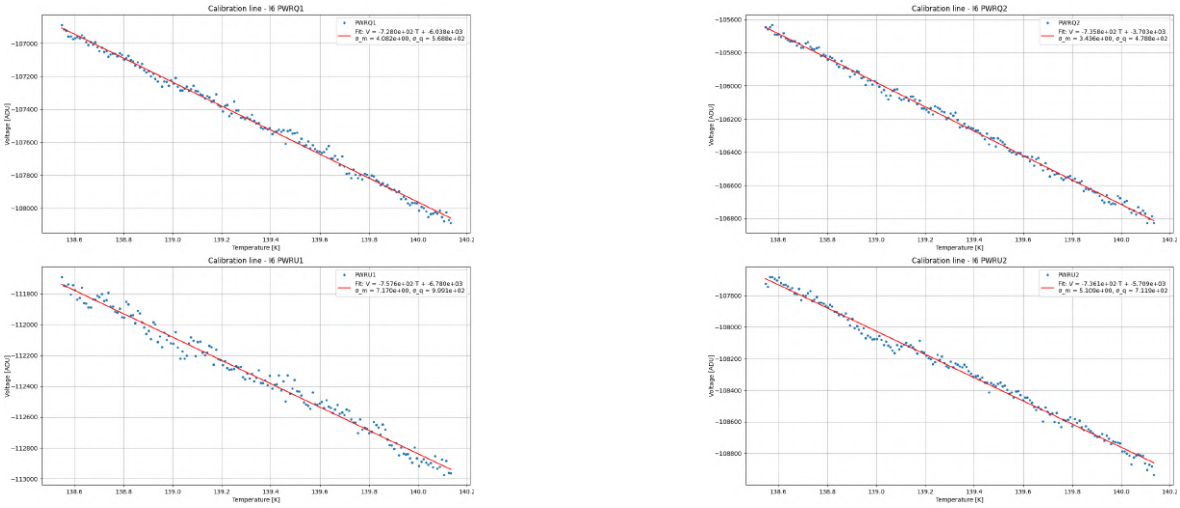

Board I, Polarimeter I6-Fit with 1 dataset: file 3		
Detector	**α [ADU/K]**	**T_n [K]**
Q1	-1234.1 ± 9.8	-41.2 ± 0.8
Q2	-1271.5 ± 9.5	-44.0 ± 0.8
U1	-1243.5 ± 16.4	-38.8 ± 0.8
U2	-1147.4 ± 9.5	-36.3 ± 0.9

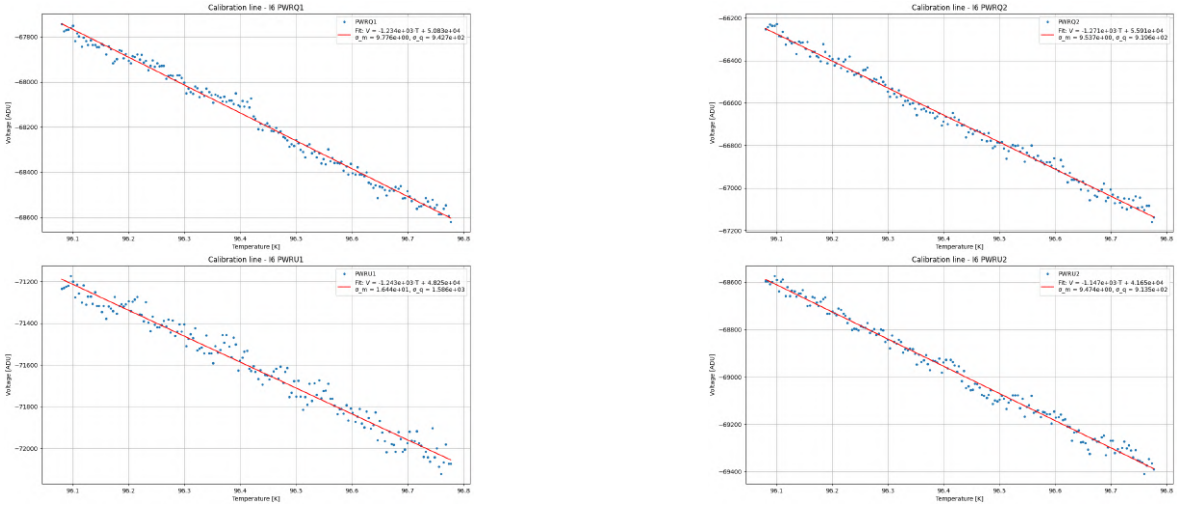

Board I, Polarimeter I6-Fit with 1 dataset: file 4		
Detector	**α [ADU/K]**	**T_n [K]**
Q1	-2920.6 ± 39.0	-62.0 ± 1.3
Q2	-2625.4 ± 37.8	-61.3 ± 1.4
U1	-2055.3 ± 80.9	-56.5 ± 3.6
U2	-2907.5 ± 36.8	-61.6 ± 1.2

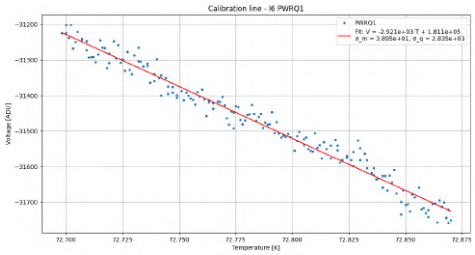

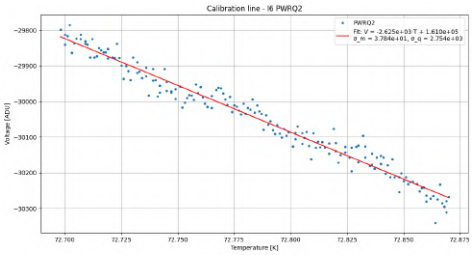

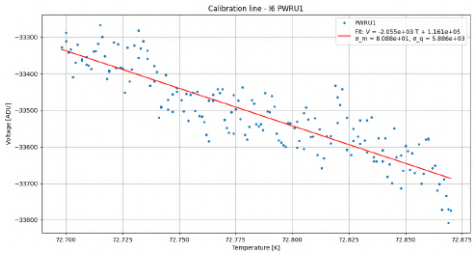

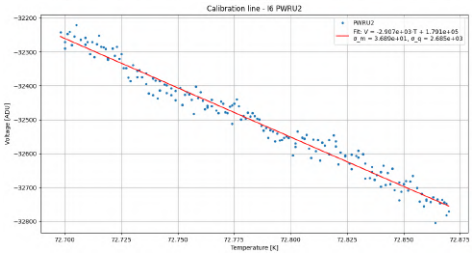

Board I, Polarimeter I6-Fit with 2 datasets: files 1,2		
Detector	**α [ADU/K]**	**T_n [K]**
Q1	-360.0 ± 0.1	159.2 ± 0.1
Q2	-364.2 ± 0.1	152.3 ± 0.1
U1	-374.3 ± 0.2	160.8 ± 0.1
U2	-359.9 ± 0.1	161.5 ± 0.1

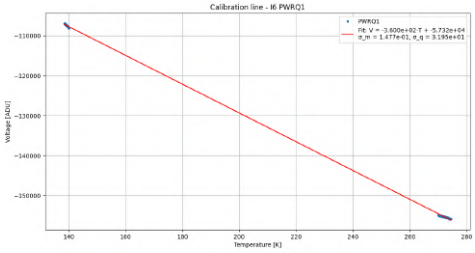

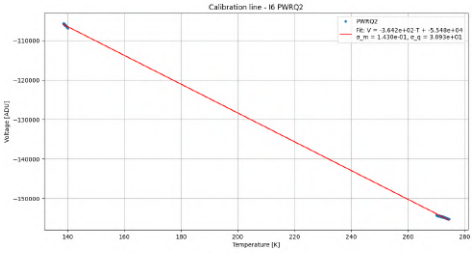

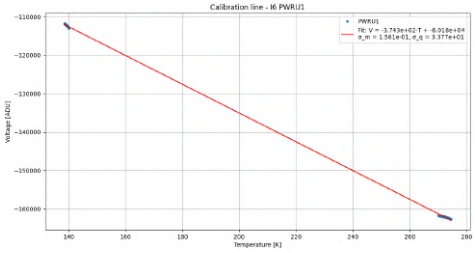

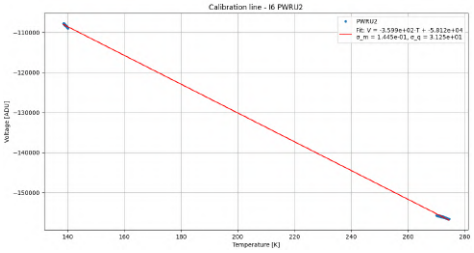

Board I, Polarimeter I6-Fit with 2 datasets: files 2,3		
Detector	**α [ADU/K]**	**T_n [K]**
Q1	-916.1 ± 0.2	-22.0 ± 0.1
Q2	-921.3 ± 0.2	-24.0 ± 0.1
U1	-948.8 ± 0.2	-20.9 ± 0.1
U2	-916.1 ± 0.2	-21.1 ± 0.1

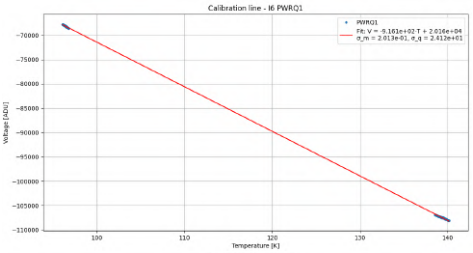

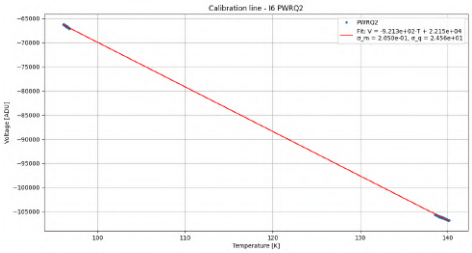

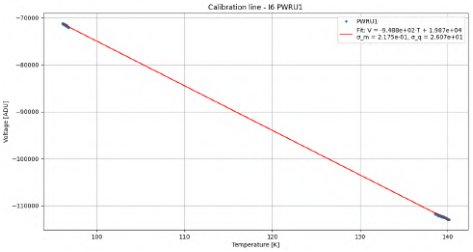

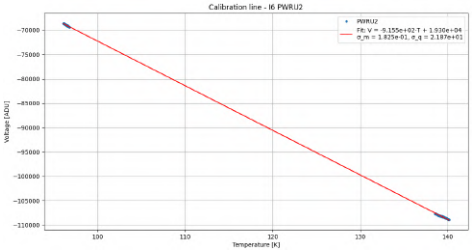

Board I, Polarimeter I6-Fit with 2 datasets: files 3,4		
Detector	**α [ADU/K]**	**T_n [K]**
Q1	-1552.1 ± 0.3	-52.5 ± 0.1
Q2	-1549.9 ± 0.3	-53.4 ± 0.1
U1	-1611.9 ± 0.3	-51.9 ± 0.1
U2	-1542.9 ± 0.4	-51.7 ± 0.1

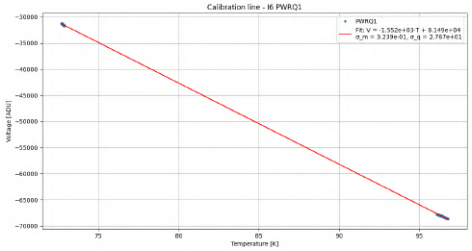

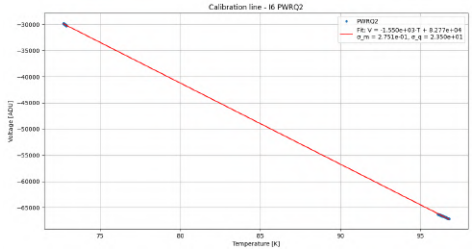

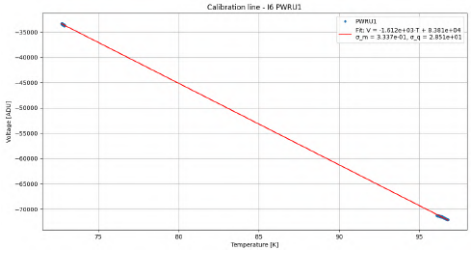

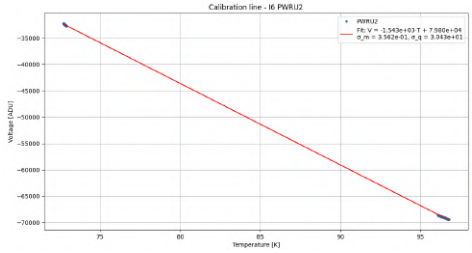

Board Y	
File ID	**T_{board} [K]**
1	-
2	-
3	-
4	-

Table B.16: Table reporting the average temperature of the board for different data files. The thermometer attached to board Y was later determined to be out of order. See board O temperature as reference.

Board Y, Polarimeter Y2		
Offset file name	**Time range (UTC)**	**Offset [ADU]**
`2025_10_09_13-44-12.h5`	14:03:00 - 14:13:00	**PWR Q1**= 239132.82
		PWR Q2= 253025.91
		PWR U1= 238017.51
		PWR U2= 249809.89

Table B.17: Table reporting the offset value considered for the detectors.

Board Y: Polarimeter Y2		
File ID	$\overline{\mathbf{T}}_{\mathbf{cal}}$ **[K]**	$\overline{\mathbf{V}}$ **[ADU]**
1	270.32	**PWR Q1**= −158813.29
		PWR Q2= −161955.47
		PWR U1= −157702.73
		PWR U2= −161250.48
2	151.40	**PWR Q1**= −109355.49
		PWR Q2= −111474.28
		PWR U1= −108446.20
		PWR U2= −112527.99
3	116.38	**PWR Q1**= −68410.06
		PWR Q2= −69706.61
		PWR U1= −68018.13
		PWR U2= −70745.76
4	96.11	**PWR Q1**= −30433.92
		PWR Q2= −30188.19
		PWR U1= −30342.35
		PWR U2= −32217.14

Table B.18: Table reporting the average temperatures of the observed calibrator subsystem and the related average values of the voltage output of the detectors, for the different data files.

Board Y, Polarimeter Y2-Fit with 4 datasets		
Detector	**α [ADU/K]**	**T_n [K]**
Q1	-668.3 ± 8.7	-21.2 ± 2.3
Q2	-684.7 ± 9.1	-22.2 ± 2.3
U1	-663.0 ± 8.6	-21.1 ± 2.3
U2	-670.6 ± 9.0	-18.0 ± 2.3

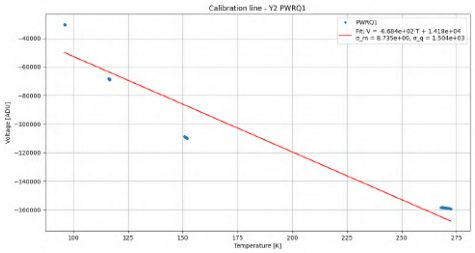

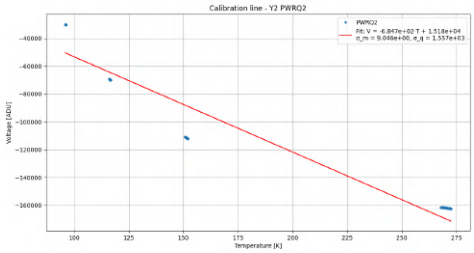

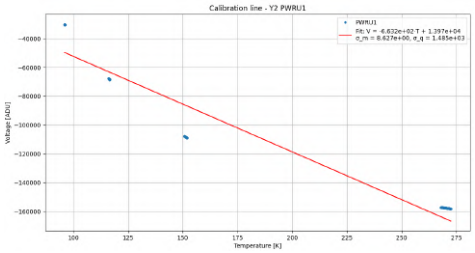

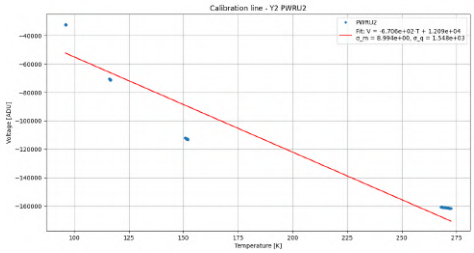

Board Y, Polarimeter Y2-Fit with 1 dataset: file 1		
Detector	**α [ADU/K]**	**T_n [K]**
Q1	-206.7 ± 1.5	498.0 ± 4.2
Q2	-205.9 ± 1.0	516.5 ± 2.7
U1	-205.0 ± 1.2	499.2 ± 3.3
U2	-225.8 ± 1.4	443.7 ± 3.2

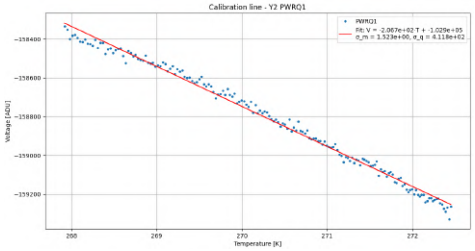

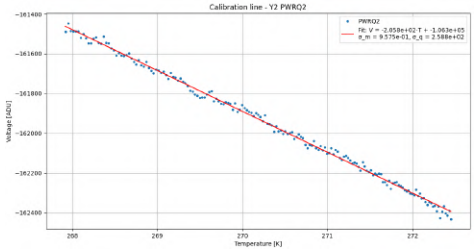

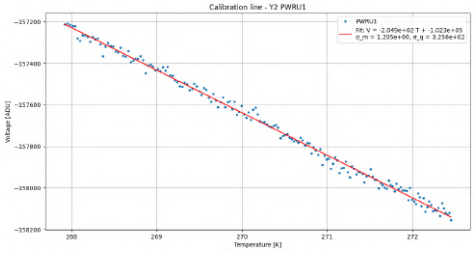

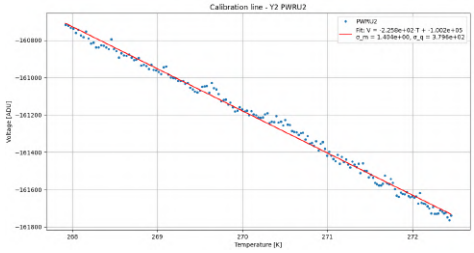

Board Y, Polarimeter Y2-Fit with 1 dataset: file 2		
Detector	**α [ADU/K]**	**T_n [K]**
Q1	-934.1 ± 4.0	-34.3 ± 0.7
Q2	-963.5 ± 4.5	-35.7 ± 0.7
U1	-929.2 ± 5.2	-34.7 ± 0.9
U2	-922.6 ± 7.6	-29.4 ± 1.3

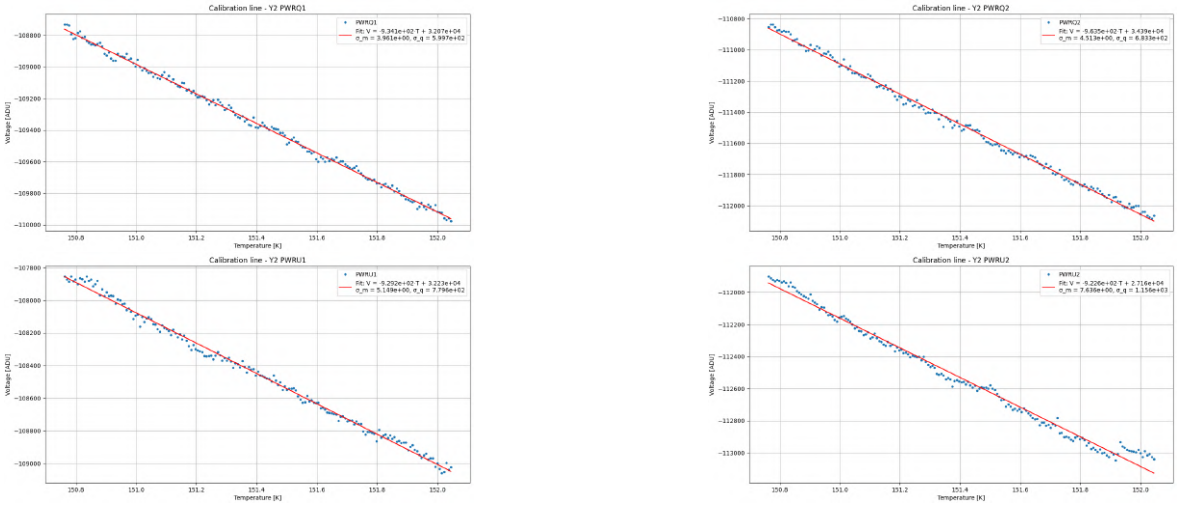

Board Y, Polarimeter Y2-Fit with 1 dataset: file 3		
Detector	**α [ADU/K]**	**T_n [K]**
Q1	-1519.0 ± 10.3	-71.4 ± 0.9
Q2	-1492.1 ± 6.8	-69.7 ± 0.6
U1	-1504.3 ± 10.1	-71.2 ± 0.9
U2	-1628.3 ± 9.8	-72.9 ± 0.8

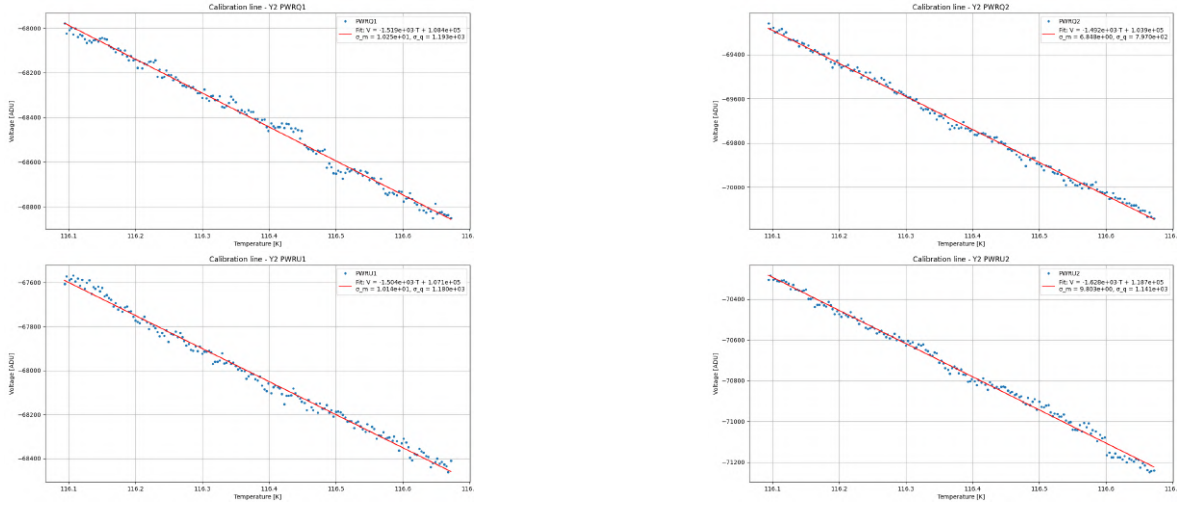

Board Y, Polarimeter Y2-Fit with 1 dataset: file 4		
Detector	**α [ADU/K]**	**T_n [K]**
Q1	-2667.3 ± 27.8	-84.7 ± 1.3
Q2	-2901.0 ± 25.9	-85.7 ± 1.2
U1	-3053.2 ± 34.3	-86.2 ± 1.5
U2	-2729.4 ± 24.0	-84.3 ± 1.1

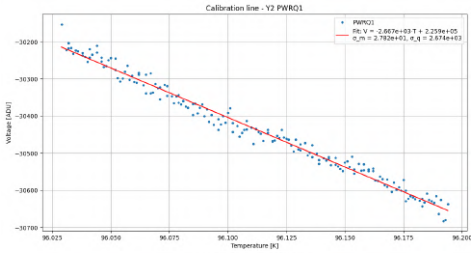

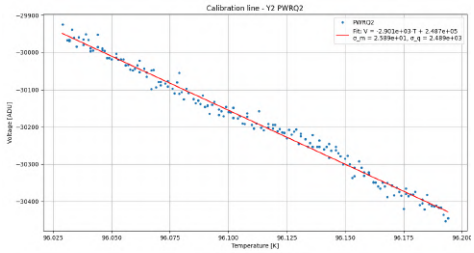

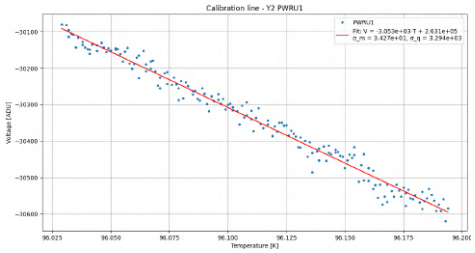

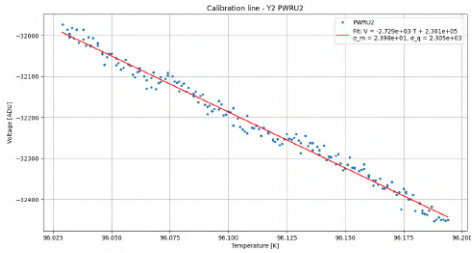

Board Y, Polarimeter Y2-Fit with 2 datasets: files 1,2		
Detector	**α [ADU/K]**	**T_n [K]**
Q1	-415.8 ± 0.2	111.6 ± 0.1
Q2	-424.4 ± 0.2	111.3 ± 0.1
U1	-414.1 ± 0.2	110.5 ± 0.1
U2	-409.7 ± 0.2	123.3 ± 0.1

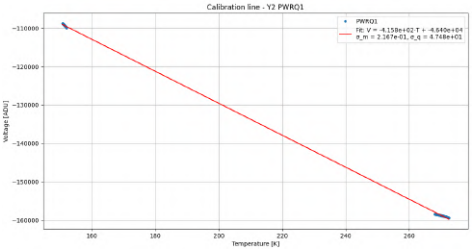

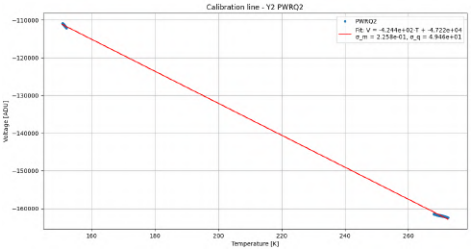

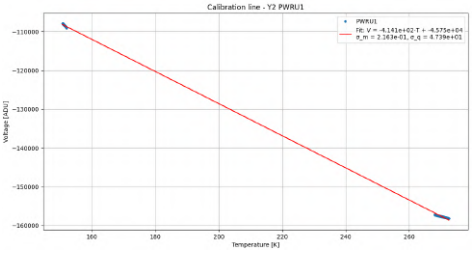

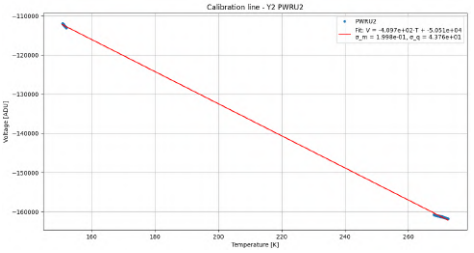

Board Y, Polarimeter Y2-Fit with 2 datasets: files 2,3		
Detector	**α [ADU/K]**	**T_n [K]**
Q1	-1169.0 ± 0.2	-57.9 ± 0.1
Q2	-1193.4 ± 0.2	-57.9 ± 0.1
U1	-1154.3 ± 0.2	-57.5 ± 0.1
U2	-1193.0 ± 0.3	-57.1 ± 0.1

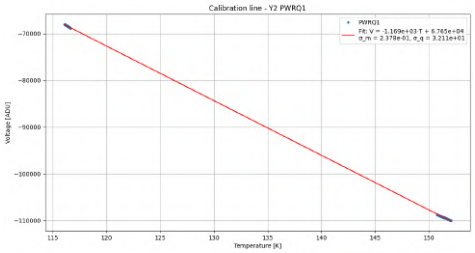

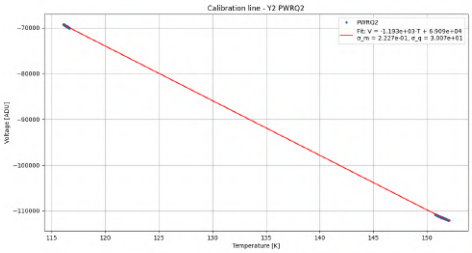

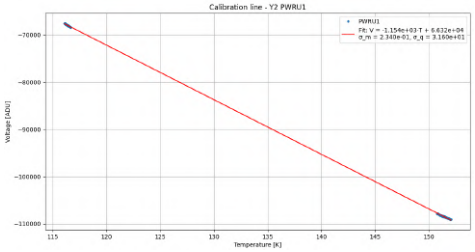

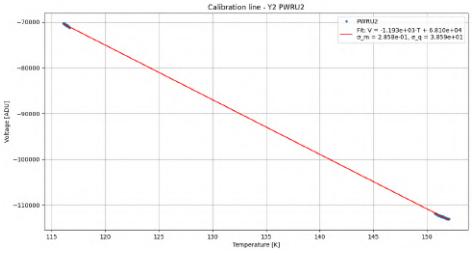

Board Y, Polarimeter Y2-Fit with 2 datasets: files 3,4		
Detector	**α [ADU/K]**	**T_n [K]**
Q1	-1874.2 ± 0.3	-79.9 ± 0.1
Q2	-1949.8 ± 0.3	-80.6 ± 0.1
U1	-1858.9 ± 0.3	-79.8 ± 0.1
U2	-1900.9 ± 0.3	-79.2 ± 0.1

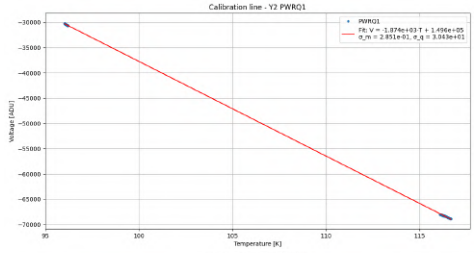

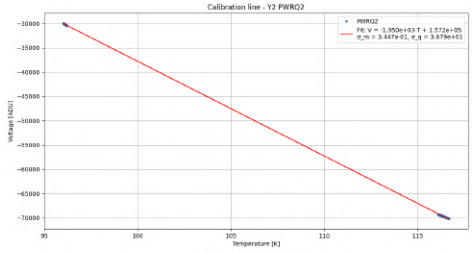

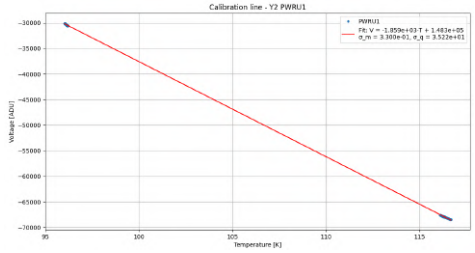

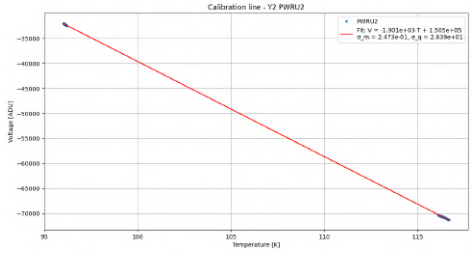

Board Y, Polarimeter Y3		
Offset file name	**Time range (UTC)**	**Offset [ADU]**
`2025_10_09_13-44-12.h5`	14:03:00 - 14:13:00	**PWR Q1**= 217538.57
		PWR Q2= 222769.48
		PWR U1= 203620.15
		PWR U2= 224210.70

Table B.19: Table reporting the offset value considered for the detectors.

Board Y: Polarimeter Y3		
File ID	$\overline{\mathbf{T}}_{\mathbf{cal}}$ **[K]**	$\overline{\mathbf{V}}$ **[ADU]**
1	263.93	**PWR Q1**= −157602.28
		PWR Q2= −157749.44
		PWR U1= −149238.10
		PWR U2= −151618.99
2	190.33	**PWR Q1**= −107689.28
		PWR Q2= −107736.23
		PWR U1= −102378.15
		PWR U2= −103255.95
3	175.56	**PWR Q1**= −66674.93
		PWR Q2= −66608.37
		PWR U1= −63672.01
		PWR U2= −63855.56
4	165.82	**PWR Q1**= −28560.70
		PWR Q2= −28049.26
		PWR U1= −27458.26
		PWR U2= −26756.38

Table B.20: Table reporting the average temperatures of the observed calibrator subsystem and the related average values of the voltage output of the detectors, for the different data files.

Board Y, Polarimeter Y3-Fit with 4 datasets		
Detector	**α [ADU/K]**	**T_n [K]**
Q1	-1147.9 ± 18.2	-120.4 ± 3.7
Q2	-1152.5 ± 18.4	-120.8 ± 3.8
U1	-1081.9 ± 17.3	-119.7 ± 3.8
U2	-1110.0 ± 17.6	-121.1 ± 3.7

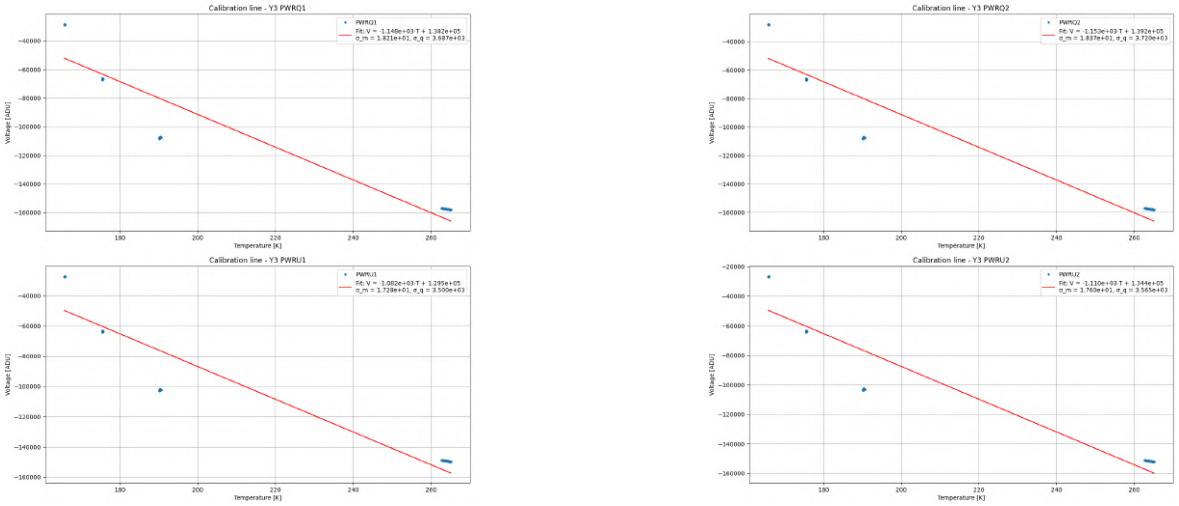

Board Y, Polarimeter Y3-Fit with 1 dataset: file 1		
Detector	**α [ADU/K]**	**T_n [K]**
Q1	-386.8 ± 2.2	143.5 ± 1.7
Q2	-386.2 ± 2.1	144.6 ± 1.6
U1	-384.1 ± 3.2	124.6 ± 2.4
U2	-377.9 ± 2.5	137.2 ± 2.0

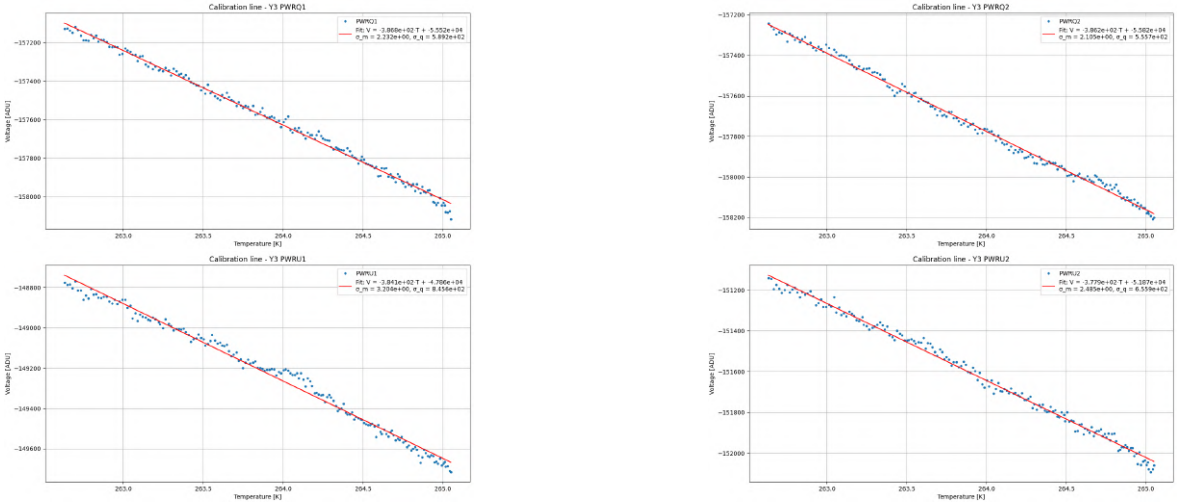

Board Y, Polarimeter Y3-Fit with 1 dataset: file 2		
Detector	**α [ADU/K]**	**T_n [K]**
Q1	1804.5 ± 148.5	-250.0 ± 25.9
Q2	1893.5 ± 153.0	-247.2 ± 25.3
U1	1544.5 ± 144.1	-256.6 ± 29.8
U2	1826.5 ± 155.9	-246.9 ± 26.6

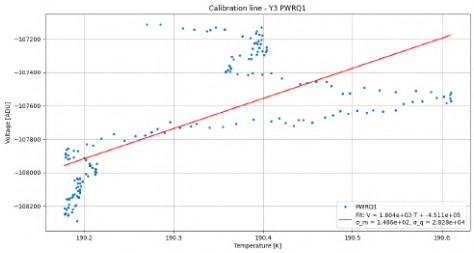

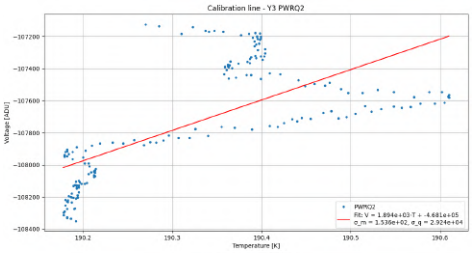

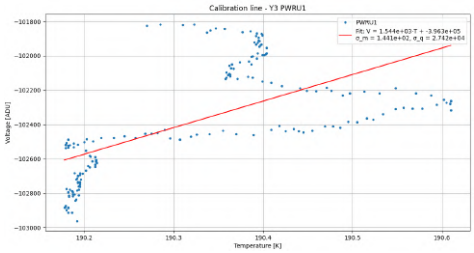

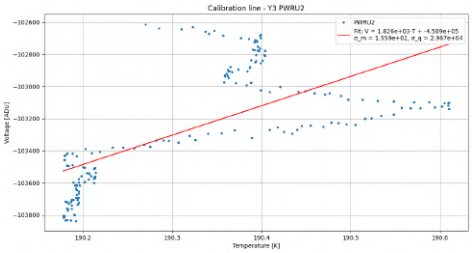

Board Y, Polarimeter Y3-Fit with 1 dataset: file 3		
Detector	**α [ADU/K]**	**T_n [K]**
Q1	-2186.0 ± 400.0	-145.1 ± 41.7
Q2	-2608.4 ± 395.1	-150.0 ± 35.1
U1	-2238.2 ± 400.0	-147.1 ± 40.9
U2	-2411.3 ± 393.5	-149.1 ± 37.6

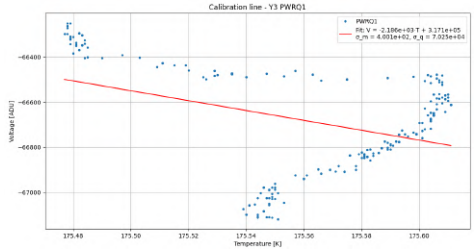

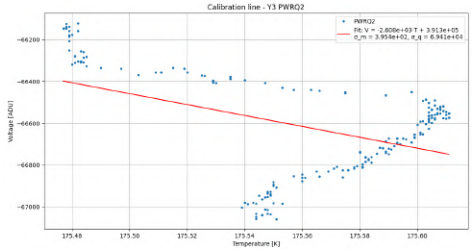

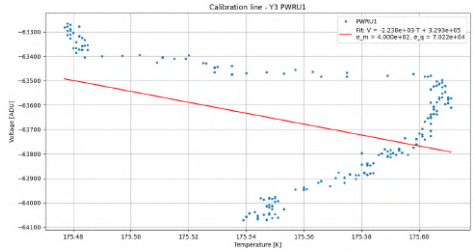

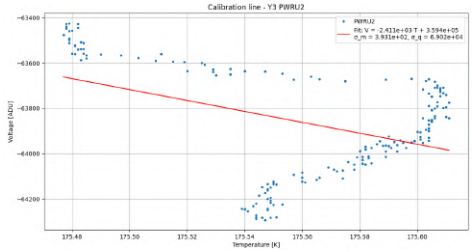

Board Y, Polarimeter Y3-Fit with 1 dataset: file 4		
Detector	**α [ADU/K]**	**T_n [K]**
Q1	-5716.1 ± 65.7	-160.8 ± 2.7
Q2	-5367.4 ± 70.1	-160.6 ± 3.0
U1	-5090.0 ± 57.7	-160.4 ± 2.6
U2	-5329.2 ± 55.6	-160.8 ± 2.4

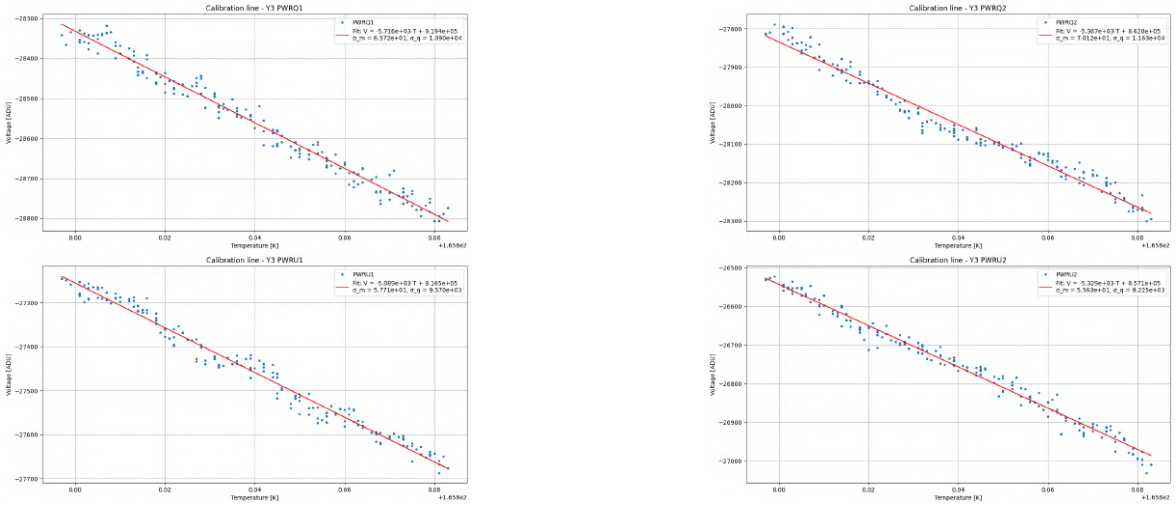

Board Y, Polarimeter Y3-Fit with 2 datasets: files 1,2		
Detector	**α [ADU/K]**	**T_n [K]**
Q1	-678.1 ± 0.5	-31.5 ± 0.2
Q2	-679.4 ± 0.5	-31.8 ± 0.2
U1	-636.6 ± 0.4	-29.5 ± 0.2
U2	-657.5 ± 0.5	-33.2 ± 0.2

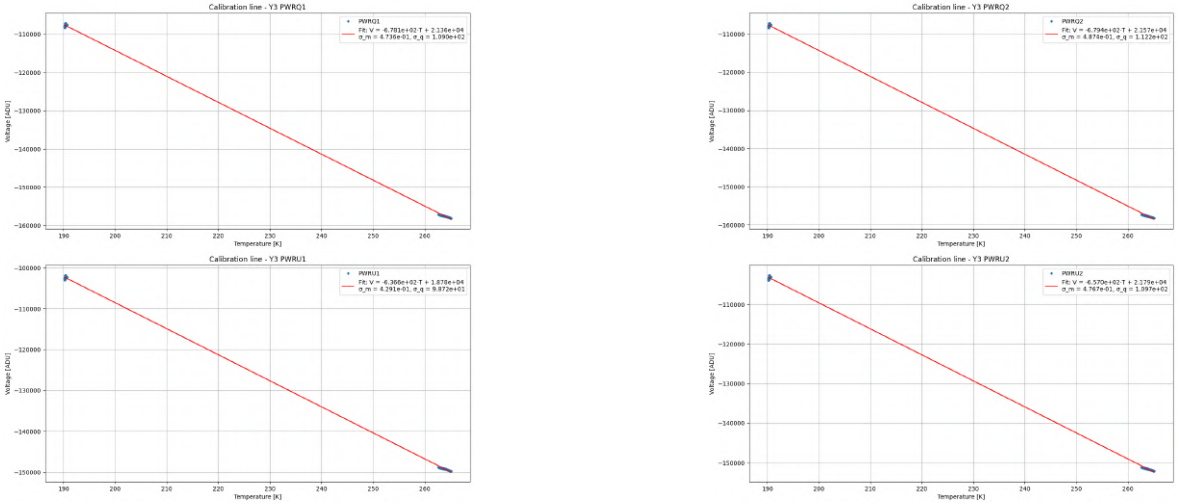

Board Y, Polarimeter Y3-Fit with 2 datasets: files 2,3		
Detector	**α [ADU/K]**	**T_n [K]**
Q1	-2776.4 ± 3.5	-151.5 ± 0.3
Q2	-2783.7 ± 3.6	-151.6 ± 0.3
U1	-2619.6 ± 3.3	-151.3 ± 0.3
U2	-2666.7 ± 3.5	-151.6 ± 0.3

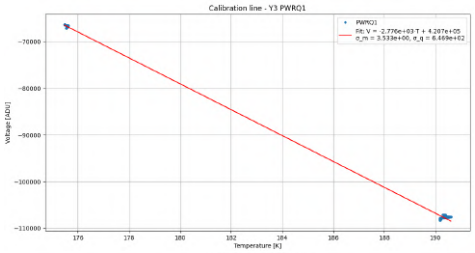

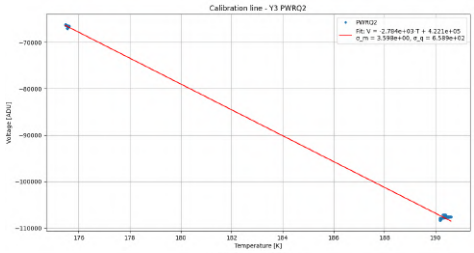

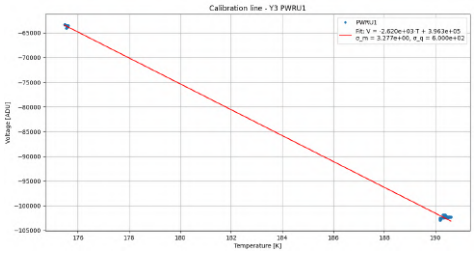

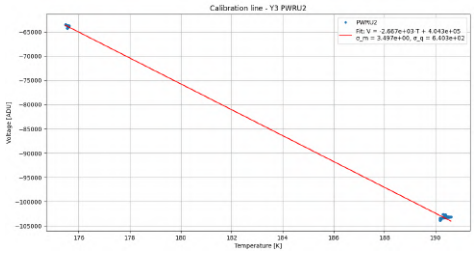

Board Y, Polarimeter Y3-Fit with 2 datasets: files 3,4		
Detector	**α [ADU/K]**	**T_n [K]**
Q1	-3921.9 ± 1.9	-158.6 ± 0.1
Q2	-3970.1 ± 1.8	-158.8 ± 0.1
U1	-3726.1 ± 1.9	-158.5 ± 0.1
U2	-3817.5 ± 1.8	-158.8 ± 0.1

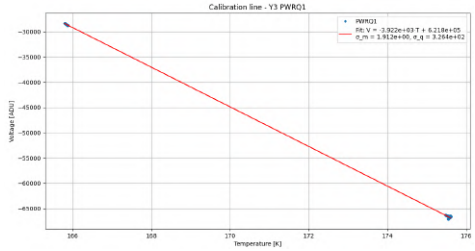

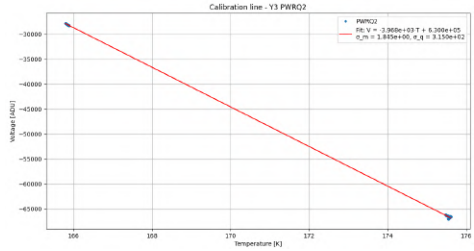

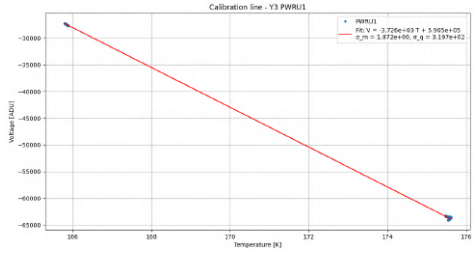

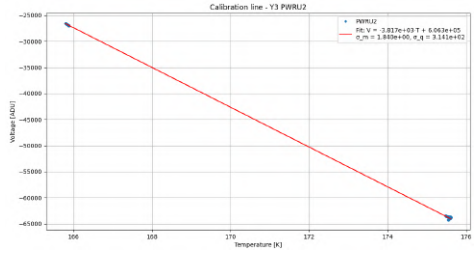

Appendix C

Plots and tables, calibrator warm up

Board O	
File ID	**T_{board} [K]**
1	156.48
2	156.47
3	156.40

Table C.1: Table reporting the average temperature of the board for different data files.

Board O, Polarimeter O4		
Offset file name	**Time range (UTC)**	**Offset [ADU]**
`2025_10_10_10-44-12.h5` [file 1]	10:55:00 - 11:00:00	**PWR Q1**= 350349.96
		PWR Q2= 329194.05
		PWR U1= 306365.39
		PWR U2= 331271.85
- [file 2]	-	**PWR Q1**= 350492.08
		PWR Q2= 329332.97
		PWR U1= 306538.10
		PWR U2= 331414.48
`2025_10_10_16-44-11.h5` [file 3]	17:08:00 - 17:13:00	**PWR Q1**= 350634.19
		PWR Q2= 329471.90
		PWR U1= 306710.82
		PWR U2= 331557.11

Table C.2: Table reporting the offset value considered for the detectors.

Board O: Polarimeter O4		
File ID	$\overline{\mathbf{T}}_{\mathbf{cal}}$ **[K]**	$\overline{\mathbf{V}}$ **[ADU]**
1	181.26	**PWR Q1**= −5650.68
		PWR Q2= −4730.70
		PWR U1= −8126.20
		PWR U2= −5366.04
2	184.11	**PWR Q1**= −5663.53
		PWR Q2= −4744.45
		PWR U1= −8176.37
		PWR U2= −5405.58
3	187.91	**PWR Q1**= −5700.98
		PWR Q2= −4778.89
		PWR U1= −8252.62
		PWR U2= −5436.59

Table C.3: Table reporting the average temperatures of the observed calibrator subsystem and the related average values of the voltage output of the detectors, for the different data files.

Board O, Polarimeter O4-Fit with 3 datasets		
Detector	α **[ADU/K]**	$\mathbf{T_n}$ **[K]**
PWR Q1	-7.5 ± 0.2	576.0 ± 14.2
PWR Q2	-6.9 ± 0.2	494.9 ± 14.3
PWR U1	-18.6 ± 0.3	254.5 ± 4.9
PWR U2	-10.0 ± 0.2	351.0 ± 7.4

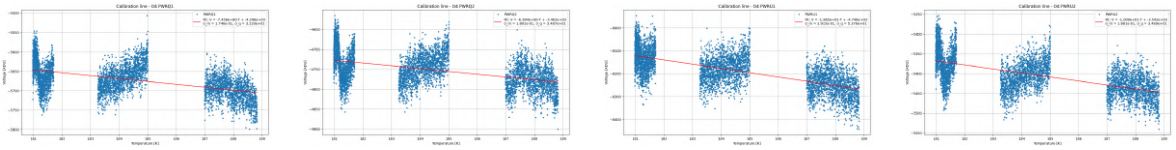

Board O, Polarimeter O4-Fit with 1 dataset: file 1		
Detector	α **[ADU/K]**	$\mathbf{T_n}$ **[K]**
PWR Q1	-72.0 ± 3.9	-102.8 ± 11.3
PWR Q2	-74.9 ± 4.5	-118.1 ± 13.0
PWR U1	-41.6 ± 6.5	13.9 ± 28.6
PWR U2	-50.8 ± 4.7	-75.7 ± 18.0

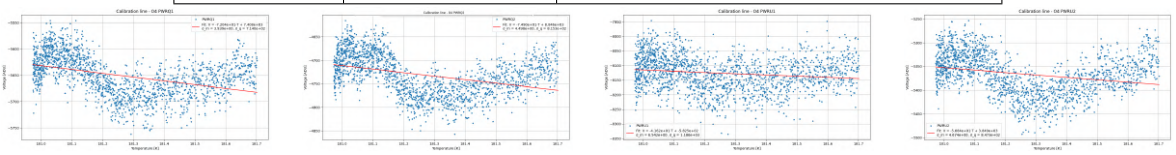

Board O, Polarimeter O4-Fit with 1 dataset: file 2		
Detector	**α [ADU/K]**	**T_n [K]**
PWR Q1	41.5 ± 1.2	-320.7 ± 10.8
PWR Q2	38.3 ± 1.4	-307.9 ± 12.6
PWR U1	37.5 ± 2.5	-402.1 ± 10.0
PWR U2	35.3 ± 1.4	-337.1 ± 15.1

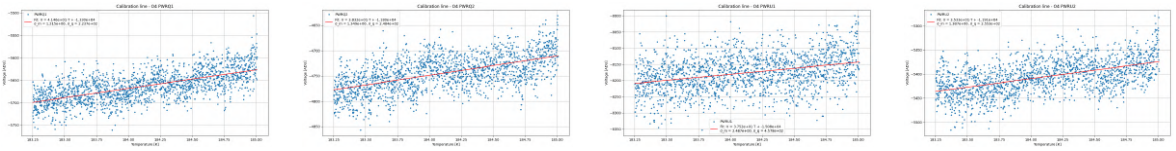

Board O, Polarimeter O4-Fit with 1 dataset: file 3		
Detector	**α [ADU/K]**	**T_n [K]**
PWR Q1	-23.4 ± 1.3	55.5 ± 10.6
PWR Q2	-9.6 ± 1.5	311.7 ± 55.5
PWR U1	-32.4 ± 2.5	67.1 ± 15.3
PWR U2	-14.3 ± 1.4	194.0 ± 26.1

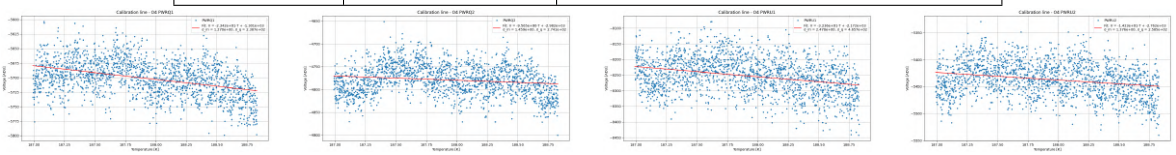

Board O, Polarimeter O4-Fit with 2 datasets: files 1,2		
Detector	**α [ADU/K]**	**T_n [K]**
PWR Q1	-2.4 ± 0.4	2164.5 ± 375.1
PWR Q2	-3.0 ± 0.5	1419.0 ± 219.2
PWR U1	-14.5 ± 0.7	377.9 ± 19.5
PWR U2	-11.3 ± 0.5	293.9 ± 14.2

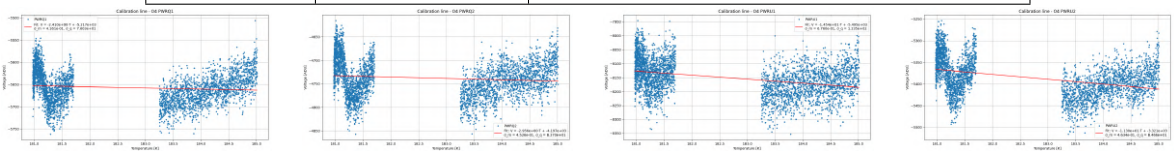

Board O, Polarimeter O4-Fit with 2 datasets: files 2,3		
Detector	**α [ADU/K]**	**T_n [K]**
PWR Q1	-8.7 ± 0.3	471.2 ± 16.7
PWR Q2	-7.5 ± 0.3	488.2 ± 19.4
PWR U1	-18.6 ± 0.5	255.4 ± 8.4
PWR U2	-6.9 ± 0.3	595.6 ± 26.2

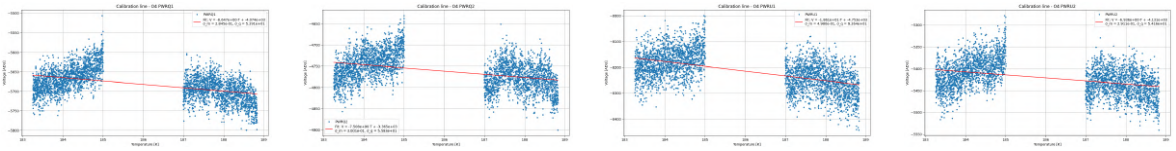

Board O, Polarimeter O5		
Offset file name	**Time range (UTC)**	**Offset [ADU]**
`2025_10_10_10-44-12.h5` [file 1]	10:55:00 - 11:00:00	**PWR Q1**= 213327.56
		PWR Q2= 206792.89
		PWR U1= 217041.63
		PWR U2= 204472.32
- [file 2]	-	**PWR Q1**= 213746.29
		PWR Q2= 207207.75
		PWR U1= 217467.72
		PWR U2= 204892.83
`2025_10_10_16-44-11.h5` [file 3]	17:08:00 - 17:13:00	**PWR Q1**= 214165.01
		PWR Q2= 207622.61
		PWR U1= 217893.82
		PWR U2= 205313.33

Table C.4: Table reporting the offset value considered for the detectors.

Board O: Polarimeter O5		
File ID	$\overline{\mathbf{T}}_{\mathbf{cal}}$ **[K]**	$\overline{\mathbf{V}}$ **[ADU]**
1	181.26	**PWR Q1**= −2190.95
		PWR Q2= −2095.59
		PWR U1= −2744.84
		PWR U2= −2705.65
2	184.11	**PWR Q1**= −2329.84
		PWR Q2= −2227.42
		PWR U1= −2848.28
		PWR U2= −2852.09
3	187.91	**PWR Q1**= −2521.01
		PWR Q2= −2416.55
		PWR U1= −3085.96
		PWR U2= −3043.46

Table C.5: Table reporting the average temperatures of the observed calibrator subsystem and the related average values of the voltage output of the detectors, for the different data files.

Board O, Polarimeter O5-Fit with 3 datasets		
Detector	α **[ADU/K]**	$\mathbf{T_n}$ **[K]**
PWR Q1	-46.7 ± 0.3	-134.2 ± 1.2
PWR Q2	-45.3 ± 0.4	-134.9 ± 2.0
PWR U1	-49.3 ± 0.3	-125.7 ± 1.3
PWR U2	-48.0 ± 0.3	-124.7 ± 1.3

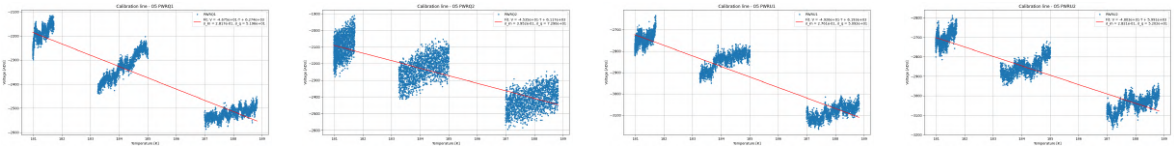

Board O, Polarimeter O5-Fit with 1 dataset: file 1		
Detector	α **[ADU/K]**	$\mathbf{T_n}$ **[K]**
PWR Q1	102.0 ± 2.6	-202.6 ± 6.8
PWR Q2	140.1 ± 6.7	-196.2 ± 12.8
PWR U1	70.3 ± 2.7	-220.3 ± 11.0
PWR U2	82.2 ± 3.4	-214.2 ± 11.7

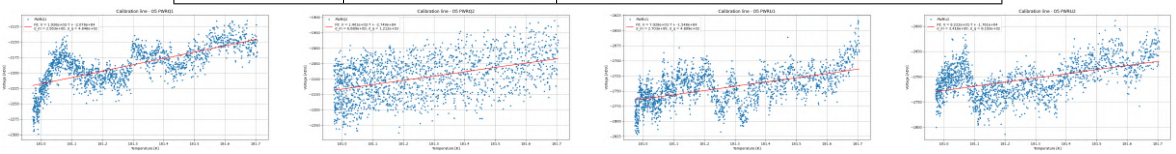

Board O, Polarimeter O5-Fit with 1 dataset: file 2		
Detector	**α [ADU/K]**	**T_n [K]**
PWR Q1	98.4 ± 0.8	-207.8 ± 9.2
PWR Q2	76.1 ± 2.8	-213.4 ± 10.2
PWR U1	61.2 ± 1.1	-230.6 ± 5.2
PWR U2	60.9 ± 1.3	-230.9 ± 6.5

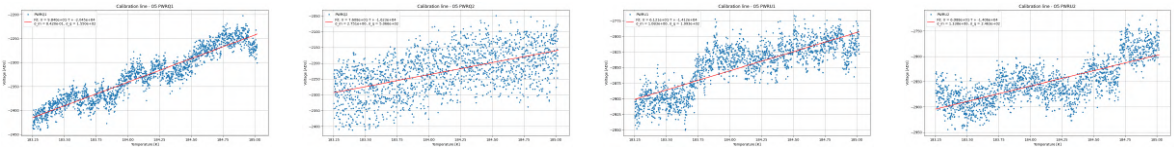

Board O, Polarimeter O5-Fit with 1 dataset: file 3		
Detector	**α [ADU/K]**	**T_n [K]**
PWR Q1	28.6 ± 0.7	-276.1 ± 8.4
PWR Q2	52.1 ± 2.6	-234.3 ± 14.7
PWR U1	40.0 ± 0.9	-264.9 ± 7.9
PWR U2	50.8 ± 1.4	-247.8 ± 8.5

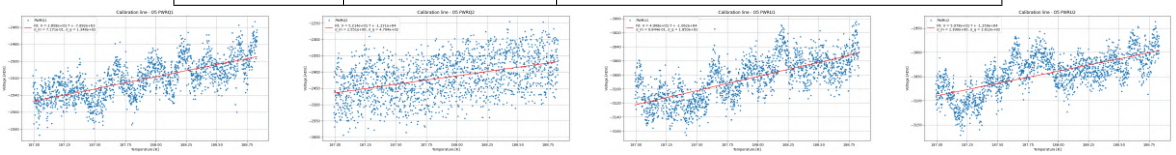

Board O, Polarimeter O5-Fit with 2 datasets: files 1,2		
Detector	**α [ADU/K]**	**T_n [K]**
PWR Q1	-38.3 ± 0.7	-123.6 ± 3.9
PWR Q2	-36.9 ± 0.9	-124.1 ± 5.4
PWR U1	-29.1 ± 0.5	-87.2 ± 3.5
PWR U2	-43.2 ± 0.6	-118.3 ± 3.0

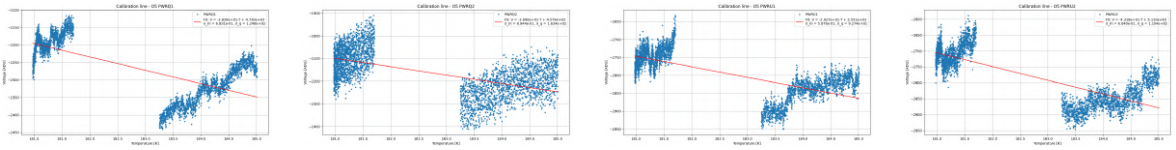

Board O, Polarimeter O5-Fit with 2 datasets: files 2,3		
Detector	**α [ADU/K]**	**T_n [K]**
PWR Q1	-42.4 ± 0.5	-128.8 ± 4.2
PWR Q2	-41.9 ± 0.7	-130.6 ± 3.8
PWR U1	-54.6 ± 0.5	-131.7 ± 2.2
PWR U2	-42.9 ± 0.5	-117.4 ± 2.7

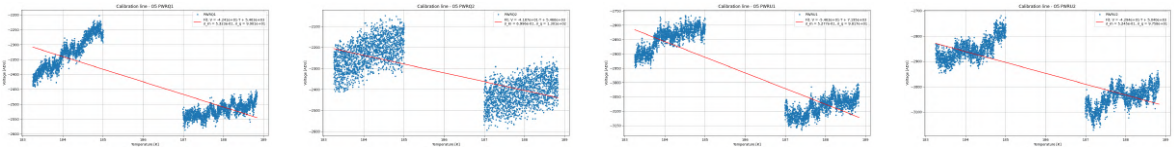

Board R	
File ID	**T_{board} [K]**
1	156.25
2	156.23
3	156.20

Table C.6: Table reporting the average temperature of the board for different data files.

Board R, Polarimeter R0		
Offset file name	**Time range (UTC)**	**Offset [ADU]**
`2025_10_10_10-44-12.h5` [file 1]	10:55:00 - 11:00:00	**PWR Q1**= 215161.24
		PWR Q2= 203983.66
		PWR U1= 147583.65
		PWR U2= 158761.83
- [file 2]	-	**PWR Q1**= 215589.06
		PWR Q2= 204377.67
		PWR U1= 147987.51
		PWR U2= 159171.47
`2025_10_10_16-44-11.h5` [file 3]	17:08:00 - 17:13:00	**PWR Q1**= 216016.87
		PWR Q2= 204771.68
		PWR U1= 148391.36
		PWR U2= 159581.11

Table C.7: Table reporting the offset value considered for the detectors.

Board R: Polarimeter R0		
File ID	$\overline{\mathbf{T}}_{\mathbf{cal}}$ **[K]**	$\overline{\mathbf{V}}$ **[ADU]**
1	181.26	**PWR Q1**= −3965.26
		PWR Q2= −2955.53
		PWR U1= −5041.92
		PWR U2= −5661.72
2	184.12	**PWR Q1**= −4183.51
		PWR Q2= −3123.10
		PWR U1= −5262.04
		PWR U2= −5911.28
3	187.91	**PWR Q1**= −4455.08
		PWR Q2= −3355.11
		PWR U1= −5557.53
		PWR U2= −6170.08

Table C.8: Table reporting the average temperatures of the observed calibrator subsystem and the related average values of the voltage output of the detectors, for the different data files.

Board R, Polarimeter R0-Fit with 3 datasets		
Detector	α **[ADU/K]**	$\mathbf{T}_{\mathbf{n}}$ **[K]**
PWR Q1	-70.5 ± 0.3	-124.8 ± 0.8
PWR Q2	-57.7 ± 0.3	-129.9 ± 1.0
PWR U1	-74.2 ± 0.3	-113.3 ± 0.7
PWR U2	-73.2 ± 0.3	-103.7 ± 0.8

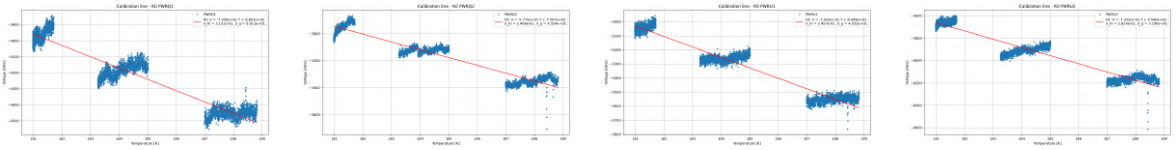

Board R, Polarimeter R0-Fit with 1 dataset: file 1		
Detector	α **[ADU/K]**	$\mathbf{T}_{\mathbf{n}}$ **[K]**
PWR Q1	143.6 ± 3.3	-208.9 ± 6.4
PWR Q2	169.2 ± 2.2	-198.7 ± 3.4
PWR U1	68.4 ± 2.3	-254.9 ± 10.5
PWR U2	54.2 ± 2.2	-285.7 ± 13.6

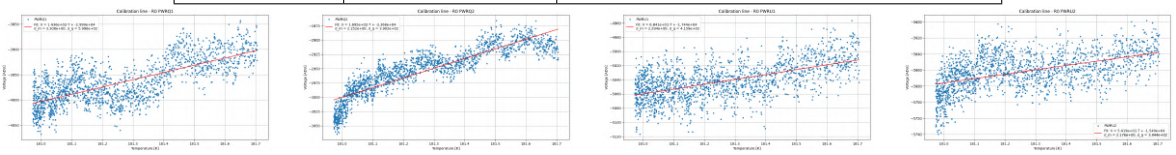

Board R, Polarimeter R0-Fit with 1 dataset: file 2		
Detector	**α [ADU/K]**	**T_n [K]**
PWR Q1	62.6 ± 1.4	-250.9 ± 6.9
PWR Q2	14.1 ± 0.8	-404.2 ± 25.6
PWR U1	21.6 ± 0.9	-428.2 ± 22.0
PWR U2	50.5 ± 0.9	-301.2 ± 6.1

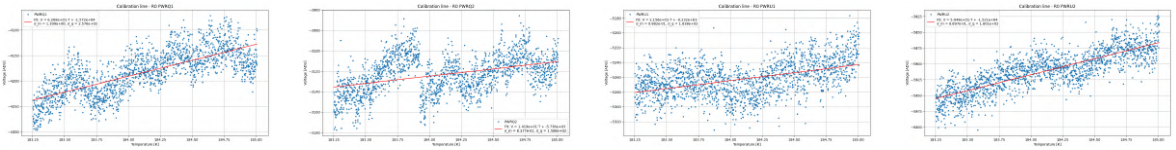

Board R, Polarimeter R0-Fit with 1 dataset: file 3		
Detector	**α [ADU/K]**	**T_n [K]**
PWR Q1	15.5 ± 1.4	-474.9 ± 46.3
PWR Q2	30.2 ± 1.0	-299.1 ± 11.9
PWR U1	16.4 ± 1.0	-525.9 ± 34.3
PWR U2	15.1 ± 1.4	-595.4 ± 56.2

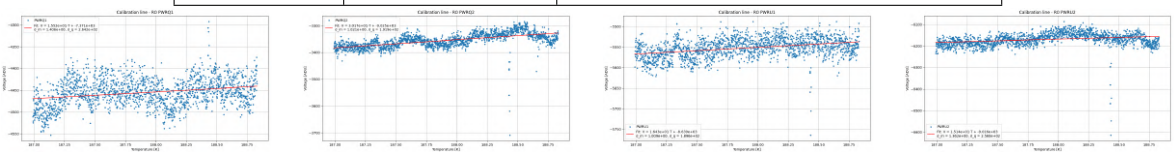

Board R, Polarimeter R0-Fit with 2 datasets: files 1,2		
Detector	**α [ADU/K]**	**T_n [K]**
PWR Q1	-66.1 ± 0.8	121.1 ± 2.5
PWR Q2	-52.1 ± 0.5	124.4 ± 2.3
PWR U1	-69.9 ± 0.5	-109.0 ± 1.6
PWR U2	-78.0 ± 0.6	108.5 ± 1.7

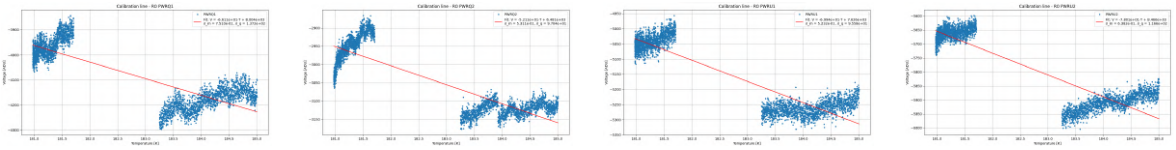

Board R, Polarimeter R0-Fit with 2 datasets: files 2,3		
Detector	**α [ADU/K]**	**T_n [K]**
PWR Q1	-63.8 ± 0.6	-118.3 ± 1.9
PWR Q2	-55.2 ± 0.4	-127.4 ± 1.6
PWR U1	-69.8 ± 0.5	108.5 ± 1.4
PWR U2	-61.1 ± 0.5	87.2 ± 21.7

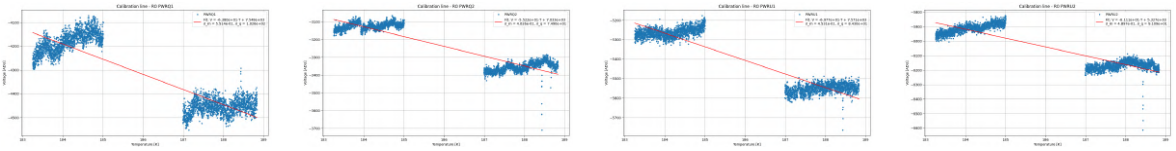

Board R, Polarimeter R6		
Offset file name	**Time range (UTC)**	**Offset [ADU]**
`2025_10_10_10-44-12.h5` [file 1]	10:55:00 - 11:00:00	**PWR Q1**= 2482.09
		PWR Q2= 237346.78
		PWR U1= 242833.90
		PWR U2= 239150.11
- [file 2]	-	**PWR Q1**= 248637.86
		PWR Q2= 237787.31
		PWR U1= 243225.61
		PWR U2= 239562.88
`2025_10_10_16-44-11.h5` [file 3]	17:08:00 - 17:13:00	**PWR Q1**= 249066.41
		PWR Q2= 238227.83
		PWR U1= 243617.32
		PWR U2= 239975.64

Table C.9: Table reporting the offset value considered for the detectors.

Board R: Polarimeter R6		
File ID	$\overline{\mathbf{T}}_{\mathbf{cal}}$ **[K]**	$\overline{\mathbf{V}}$ **[ADU]**
1	181.26	**PWR Q1**= −18585.30
		PWR Q2= −18480.81
		PWR U1= −29631.19
		PWR U2= −19944.72
2	184.11	**PWR Q1**= −18950.04
		PWR Q2= −18882.27
		PWR U1= −30102.57
		PWR U2= −20309.52
3	187.91	**PWR Q1**= −19377.64
		PWR Q2= −19307.15
		PWR U1= −30666.80
		PWR U2= −20733.78

Table C.10: Table reporting the average temperatures of the observed calibrator subsystem and the related average values of the voltage output of the detectors, for the different data files.

Board R, Polarimeter R6-Fit with 3 datasets		
Detector	α **[ADU/K]**	$\mathbf{T_n}$ **[K]**
PWR Q1	-116.2 ± 0.3	-21.2 ± 0.5
PWR Q2	-120.2 ± 0.3	-27.2 ± 0.5
PWR U1	-152.4 ± 0.3	13.3 ± 0.4
PWR U2	-115.6 ± 0.3	-8.3 ± 0.4

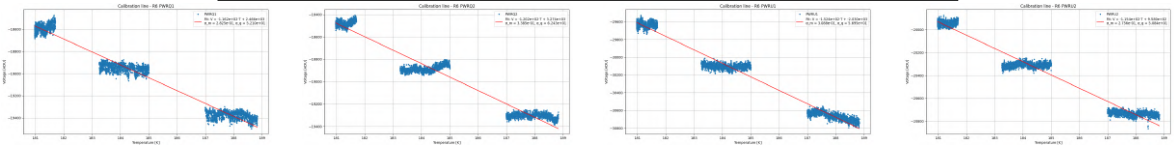

Board R, Polarimeter R6-Fit with 1 dataset: file 1		
Detector	α **[ADU/K]**	$\mathbf{T_n}$ **[K]**
PWR Q1	50.0 ± 3.5	-552.6 ± 40.7
PWR Q2	38.4 ± 2.4	-662.0 ± 43.1
PWR U1	-3.8 ± 1.4	7653.5 ± 682.1
PWR U2	7.9 ± 2.1	-2682.2 ± 714.8

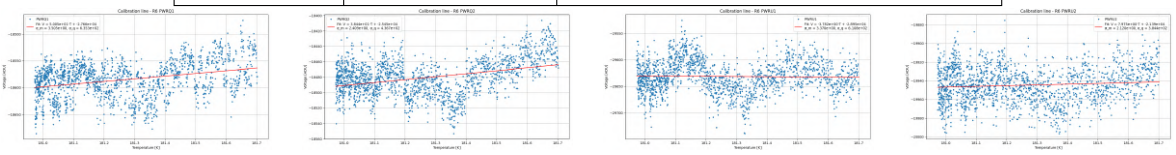

Board R, Polarimeter R6-Fit with 1 dataset: file 2		
Detector	**α [ADU/K]**	**T_n [K]**
PWR Q1	-22.6 ± 1.5	654.7 ± 43.8
PWR Q2	32.4 ± 1.0	-776.9 ± 24.8
PWR U1	-10.0 ± 1.2	2814.3 ± 337.4
PWR U2	4.8 ± 0.9	-4458.14 ± 864.1

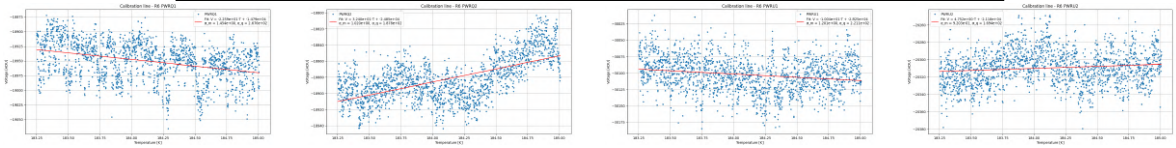

Board R, Polarimeter R6-Fit with 1 dataset: file 3		
Detector	**α [ADU/K]**	**T_n [K]**
PWR Q1	-22.5 ± 1.4	672.5 ± 30.4
PWR Q2	-11.8 ± 0.9	1450.2 ± 117.2
PWR U1	-67.2 ± 1.3	267.9 ± 6.1
PWR U2	-15.7 ± 0.9	1132.64 ± 64.9

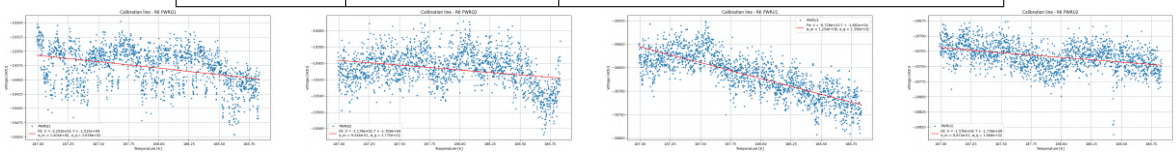

Board R, Polarimeter R6-Fit with 2 datasets: files 1,2		
Detector	**α [ADU/K]**	**T_n [K]**
PWR Q1	-259.7 ± 1.1	-109.6 ± 1.0
PWR Q2	-272.1 ± 1.4	-113.3 ± 1.1
PWR U1	-282.0 ± 1.3	-76.21 ± 0.9
PWR U2	-253.4 ± 1.22	-102.5 ± 1.0

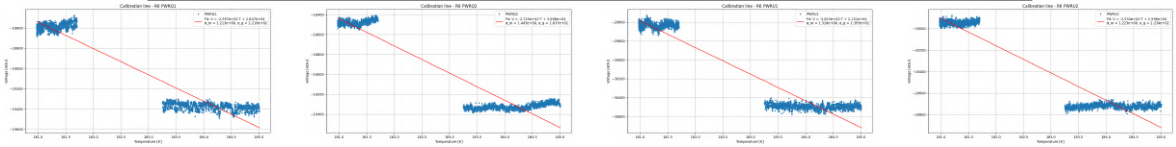

Board R, Polarimeter R6-Fit with 2 datasets: files 2,3		
Detector	**α [ADU/K]**	**T_n [K]**
PWR Q1	-106.4 ± 0.5	-5.8 ± 0.8
PWR Q2	-103.4 ± 0.6	-1.4 ± 1.0
PWR U1	-141.2 ± 0.5	29.4 ± 0.7
PWR U2	-104.5 ± 0.5	10.6 ± 0.9

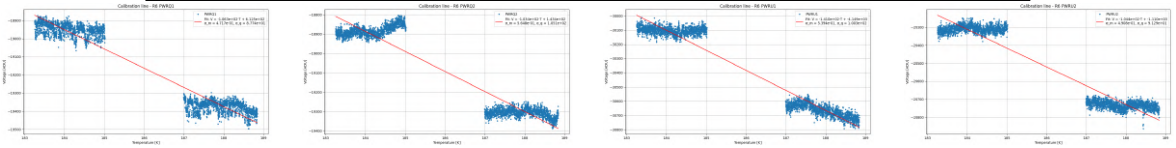

Board I	
File ID	**T_{board} [K]**
1	156.65
2	156.62
3	156.60

Table C.11: Table reporting the average temperature of the board for different data files.

Board I, Polarimeter I1		
Offset file name	**Time range (UTC)**	**Offset [ADU]**
`2025_10_10_10-44-12.h5` [file 1]	10:55:00 - 11:00:00	**PWR Q1**= 214435.31
		PWR Q2= 216050.62
		PWR U1= 239499.10
		PWR U2= 215362.08
- [file 2]	-	**PWR Q1**= 214866.56
		PWR Q2= 216501.19
		PWR U1= 239902.91
		PWR U2= 215746.52
`2025_10_10_16-44-11.h5` [file 3]	17:08:00 - 17:13:00	**PWR Q1**= 215297.80
		PWR Q2= 216951.76
		PWR U1= 240306.70
		PWR U2= 216130.96

Table C.12: Table reporting the offset value considered for the detectors.

Board I: Polarimeter I1		
File ID	$\overline{\mathbf{T}}_{\mathbf{cal}}$ **[K]**	$\overline{\mathbf{V}}$ **[ADU]**
1	164.15	**PWR Q1**= −6256.15
		PWR Q2= −4939.23
		PWR U1= −7167.75
		PWR U2= −6792.38
2	168.55	**PWR Q1**= −6503.81
		PWR Q2= −5172.06
		PWR U1= −7427.95
		PWR U2= −7007.95
3	172.61	**PWR Q1**= −6744.88
		PWR Q2= −5384.20
		PWR U1= −7603.01
		PWR U2= −7189.08

Table C.13: Table reporting the average temperatures of the observed calibrator subsystem and the related average values of the voltage output of the detectors, for the different data files.

Board I, Polarimeter I1-Fit with 3 datasets		
Detector	α **[ADU/K]**	$\mathbf{T_n}$ **[K]**
PWR Q1	-55.5 ± 0.2	-51.4 ± 0.7
PWR Q2	-50.2 ± 0.3	-65.5 ± 0.9
PWR U1	-49.2 ± 0.3	-18.2 ± 0.9
PWR U2	-44.9 ± 0.2	-12.9 ± 0.8

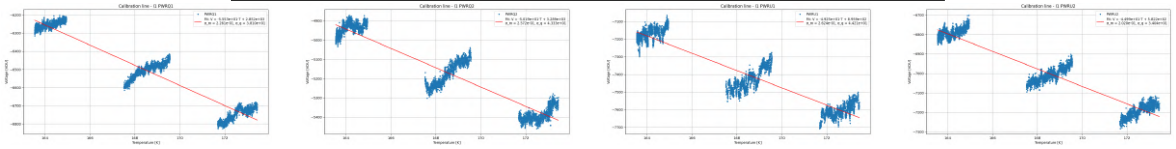

Board I, Polarimeter I1-Fit with 1 dataset: file 1		
Detector	α **[ADU/K]**	$\mathbf{T_n}$ **[K]**
PWR Q1	35.4 ± 0.8	-340.9 ± 10.2
PWR Q2	43.4 ± 1.4	-278.0 ± 10.6
PWR U1	46.3 ± 1.6	-318.8 ± 12.5
PWR U2	35.3 ± 1.1	-356.7 ± 12.7

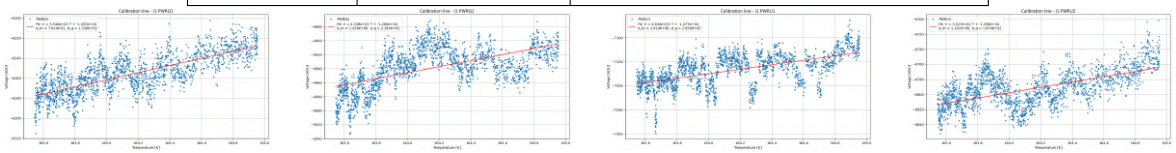

Board I, Polarimeter I1-Fit with 1 dataset: file 2		
Detector	**α [ADU/K]**	**T_n [K]**
PWR Q1	62.2 ± 0.7	-273.1 ± 3.7
PWR Q2	95.9 ± 0.9	-222.5 ± 2.6
PWR U1	85.4 ± 1.4	-255.5 ± 5.0
PWR U2	54.1 ± 0.7	-298.0 ± 4.6

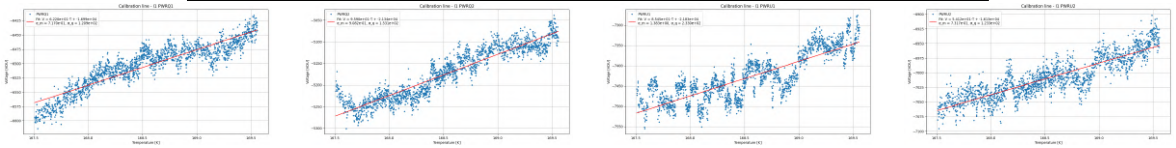

Board I, Polarimeter I1-Fit with 1 dataset: file 3		
Detector	**α [ADU/K]**	**T_n [K]**
PWR Q1	56.7 ± 0.9	-291.6 ± 5.3
PWR Q2	51.5 ± 1.3	-277.1 ± 8.1
PWR U1	50.2 ± 1.3	-324.1 ± 9.6
PWR U2	56.1 ± 0.9	-300.8 ± 5.3

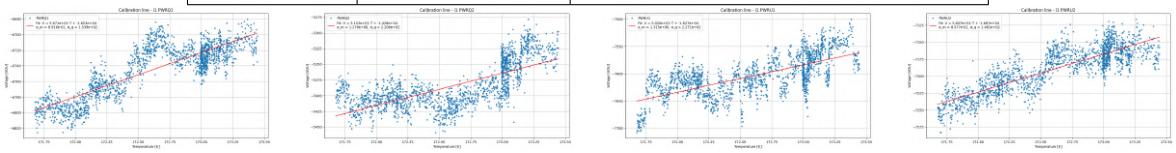

Board I, Polarimeter I1-Fit with 2 datasets: files 1,2		
Detector	**α [ADU/K]**	**T_n [K]**
PWR Q1	-51.1 ± 0.4	-41.6 ± 1.4
PWR Q2	-46.7 ± 0.5	-58.2 ± 1.9
PWR U1	-52.9 ± 0.5	-28.5 ± 1.7
PWR U2	-44.4 ± 0.4	-11.1 ± 1.4

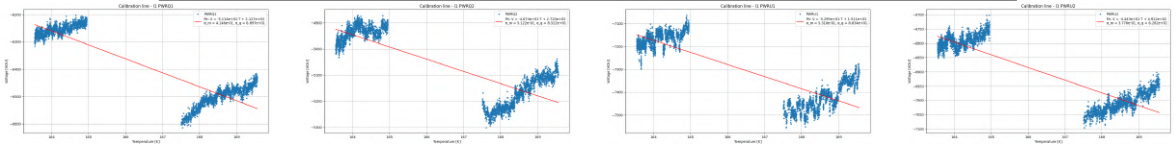

Board I, Polarimeter I1-Fit with 2 datasets: files 2,3		
Detector	**α [ADU/K]**	**T_n [K]**
PWR Q1	-51.9 ± 0.5	-42.9 ± 1.7
PWR Q2	-44.1 ± 0.6	-50.9 ± 2.3
PWR U1	-36.0 ± 0.5	38.0 ± 2.6
PWR U2	-38.4 ± 0.4	14.4 ± 1.9

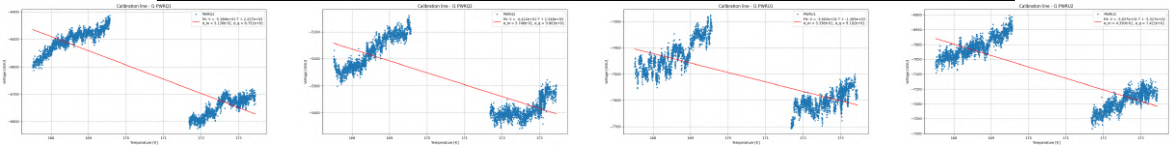

Board I, Polarimeter I6		
Offset file name	**Time range (UTC)**	**Offset [ADU]**
`2025_10_10_10-44-12.h5` [file 1]	10:55:00 - 11:00:00	**PWR Q1**= 218103.26
		PWR Q2= 216397.23
		PWR U1= 221929.00
		PWR U2= 223565.52
- [file 2]	-	**PWR Q1**= 218535.26
		PWR Q2= 216837.20
		PWR U1= 222383.42
		PWR U2= 223992.99
`2025_10_10_16-44-11.h5` [file 3]	17:08:00 - 17:13:00	**PWR Q1**= 218967.26
		PWR Q2= 217277.16
		PWR U1= 222837.84
		PWR U2= 224420.46

Table C.14: Table reporting the offset value considered for the detectors.

Board I: Polarimeter I6		
File ID	$\overline{\mathbf{T}}_{\mathbf{cal}}$ **[K]**	$\overline{\mathbf{V}}$ **[ADU]**
1	73.96	**PWR Q1**= −7565.34
		PWR Q2= −6137.00
		PWR U1= −8736.55
		PWR U2= −8628.65
2	89.41	**PWR Q1**= −7891.36
		PWR Q2= −6448.80
		PWR U1= −9058.51
		PWR U2= −8998.40
3	101.87	**PWR Q1**= −8118.82
		PWR Q2= −6687.44
		PWR U1= −9328.85
		PWR U2= −9274.63

Table C.15: Table reporting the average temperatures of the observed calibrator subsystem and the related average values of the voltage output of the detectors, for the different data files.

Board I, Polarimeter I6-Fit with 3 datasets		
Detector	α **[ADU/K]**	$\mathbf{T_n}$ **[K]**
PWR Q1	-18.9 ± 0.9	327.6 ± 1.5
PWR Q2	-18.6 ± 0.9	256.3 ± 1.3
PWR U1	-20.2 ± 1.0	358.8 ± 1.8
PWR U2	-22.2 ± 0.9	316.1 ± 1.3

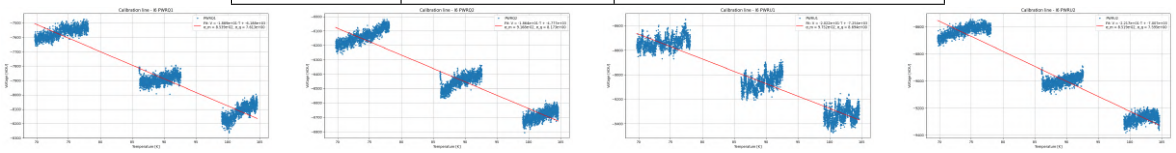

Board I, Polarimeter I6-Fit with 1 dataset: file 1		
Detector	α **[ADU/K]**	$\mathbf{T_n}$ **[K]**
PWR Q1	10.9 ± 0.2	-763.1 ± 16.6
PWR Q2	16.4 ± 0.2	-447.2 ± 6.3
PWR U1	8.0 ± 0.4	-1126.8 ± 63.7
PWR U2	10.8 ± 0.2	-868.6 ± 19.8

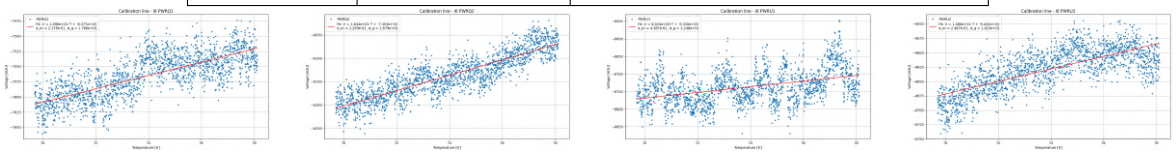

Board I, Polarimeter I6-Fit with 1 dataset: file 2		
Detector	**α [ADU/K]**	**T_n [K]**
PWR Q1	7.6 ± 0.3	-1128.4 ± 50.1
PWR Q2	18.4 ± 0.4	-440.6 ± 8.8
PWR U1	18.6 ± 0.6	-577.2 ± 19.6
PWR U2	9.3 ± 0.3	-1053.2 ± 37.8

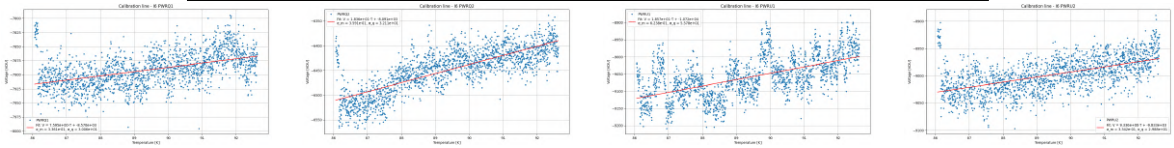

Board I, Polarimeter I6-Fit with 1 dataset: file 3		
Detector	**α [ADU/K]**	**T_n [K]**
PWR Q1	24.3 ± 0.4	-435.9 ± 7.6
PWR Q2	15.2 ± 0.4	-542.8 ± 13.3
PWR U1	9.1 ± 0.8	-1128.1 ± 97.2
PWR U2	9.5 ± 0.4	-1080.8 ± 47.1

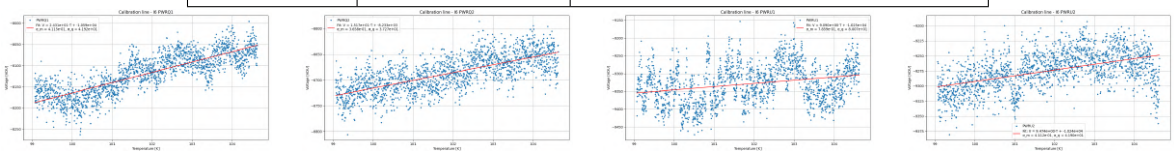

Board I, Polarimeter I6-Fit with 2 datasets: files 1,2		
Detector	**α [ADU/K]**	**T_n [K]**
PWR Q1	-18.8 ± 0.2	328.9 ± 2.7
PWR Q2	-17.4 ± 0.2	279.6 ± 2.9
PWR U1	-18.4 ± 0.2	401.2 ± 4.0
PWR U2	-21.4 ± 0.2	330.1 ± 2.6

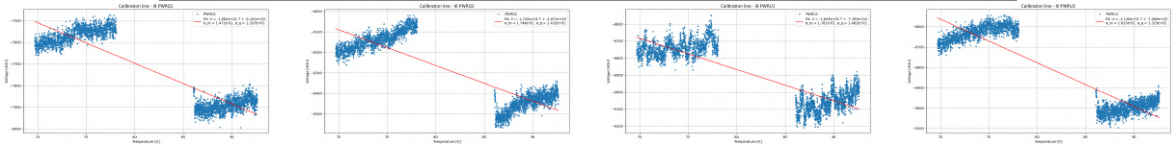

Board I, Polarimeter I6-Fit with 2 datasets: files 2,3		
Detector	**α [ADU/K]**	**T_n [K]**
PWR Q1	-15.8 ± 0.2	410.3 ± 4.4
PWR Q2	-16.5 ± 0.2	303.3 ± 3.4
PWR U1	-18.9 ± 0.2	388.5 ± 4.4
PWR U2	-19.8 ± 0.2	365.4 ± 2.9

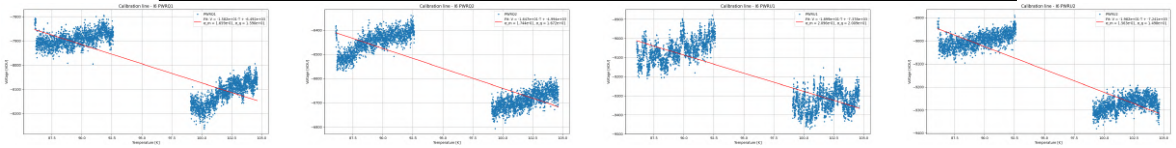

Board Y	
File ID	**T_{board} [K]**
1	-
2	-
3	-

Table C.16: Table reporting the average temperature of the board for different data files. The thermometer attached to board Y was later determined to be out of order. See board O temperature as reference.

Board Y, Polarimeter Y2		
Offset file name	**Time range (UTC)**	**Offset [ADU]**
`2025_10_10_10-44-12.h5` [file 1]	10:55:00 - 11:00:00	**PWR Q1**= 242566.62
		PWR Q2= 256799.67
		PWR U1= 241396.53
		PWR U2= 253178.07
- [file 2]	-	**PWR Q1**= 242986.46
		PWR Q2= 257258.37
		PWR U1= 211799.54
		PWR U2= 253623.69
`2025_10_10_16-44-11.h5` [file 3]	17:08:00 - 17:13:00	**PWR Q1**= 243406.31
		PWR Q2= 257717.07
		PWR U1= 242252.55
		PWR U2= 254069.32

Table C.17: Table reporting the offset value considered for the detectors.

Board Y: Polarimeter Y2		
File ID	$\overline{\mathbf{T}}_{\mathbf{cal}}$ **[K]**	$\overline{\mathbf{V}}$ **[ADU]**
1	93.82	**PWR Q1**= −5293.67
		PWR Q2= −2935.85
		PWR U1= −5297.76
		PWR U2= −6828.74
2	103.90	**PWR Q1**= −5468.05
		PWR Q2= −3176.40
		PWR U1= −5493.14
		PWR U2= −7053.33
3	113.70	**PWR Q1**= −5682.50
		PWR Q2= −3464.57
		PWR U1= −5706.45
		PWR U2= −7277.99

Table C.18: Table reporting the average temperatures of the observed calibrator subsystem and the related average values of the voltage output of the detectors, for the different data files.

Board Y, Polarimeter Y2-Fit with 3 datasets		
Detector	α **[ADU/K]**	$\mathbf{T_n}$ **[K]**
PWR Q1	-18.6 ± 0.1	191.7 ± 1.1
PWR Q2	-25.4 ± 0.1	220.2 ± 0.5
PWR U1	-19.4 ± 0.1	179.5 ± 1.1
PWR U2	-21.5 ± 0.1	224.0 ± 1.0

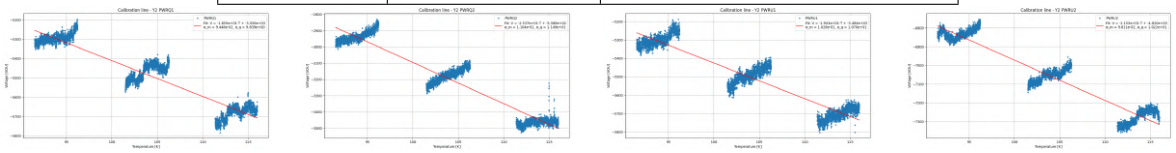

Board Y, Polarimeter Y2-Fit with 1 dataset: file 1		
Detector	α **[ADU/K]**	$\mathbf{T_n}$ **[K]**
PWR Q1	12.9 ± 0.3	-503.8 ± 12.9
PWR Q2	21.1 ± 0.3	-232.7 ± 3.4
PWR U1	19.6 ± 0.4	-364.5 ± 7.3
PWR U2	8.4 ± 0.4	-305.2 ± 43.2

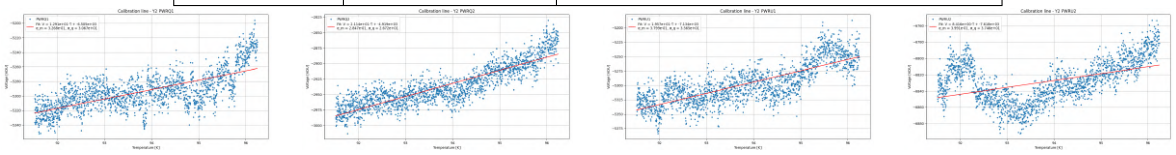

Board Y, Polarimeter Y2-Fit with 1 dataset: file 2		
Detector	**α [ADU/K]**	**T_n [K]**
PWR Q1	21.3 ± 0.5	-361.0 ± 7.9
PWR Q2	27.1 ± 0.3	-221.0 ± 2.4
PWR U1	25.7 ± 0.4	-317.7 ± 4.7
PWR U2	20.8 ± 0.3	-443.7 ± 6.0

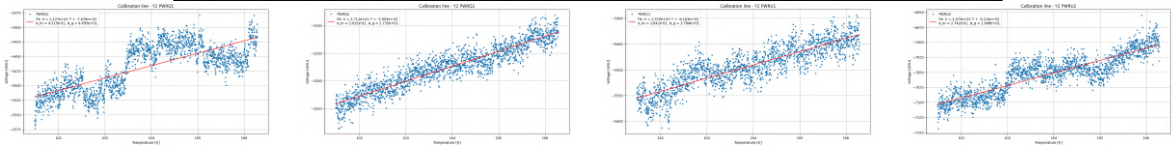

Board Y, Polarimeter Y2-Fit with 1 dataset: file 3		
Detector	**α [ADU/K]**	**T_n [K]**
PWR Q1	18.2 ± 0.4	-429.3 ± 10.6
PWR Q2	6.5 ± 0.4	-646.7 ± 36.4
PWR U1	19.7 ± 0.4	-403.5 ± 7.6
PWR U2	23.7 ± 0.4	-420.6 ± 6.5

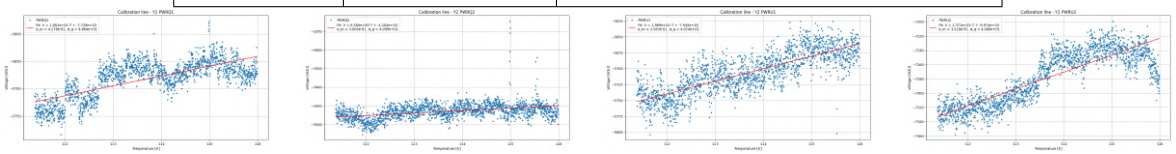

Board Y, Polarimeter Y2-Fit with 2 datasets: files 1,2		
Detector	**α [ADU/K]**	**T_n [K]**
PWR Q1	-14.9 ± 0.2	261.2 ± 3.1
PWR Q2	-20.6 ± 0.2	49.7 ± 1.2
PWR U1	-16.5 ± 0.2	228.2 ± 2.9
PWR U2	-19.8 ± 0.2	252.4 ± 2.4

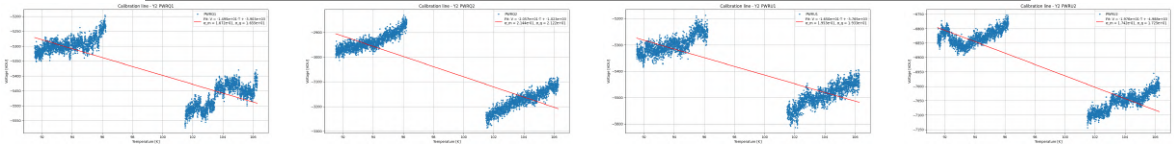

Board Y, Polarimeter Y2-Fit with 2 datasets: files 2,3		
Detector	**α [ADU/K]**	**T_n [K]**
PWR Q1	-18.9 ± 0.2	185.9 ± 2.3
PWR Q2	-26.1 ± 0.2	18.5 ± 0.9
PWR U1	-18.6 ± 0.2	192.3 ± 2.5
PWR U2	-19.7 ± 0.2	254.9 ± 2.9

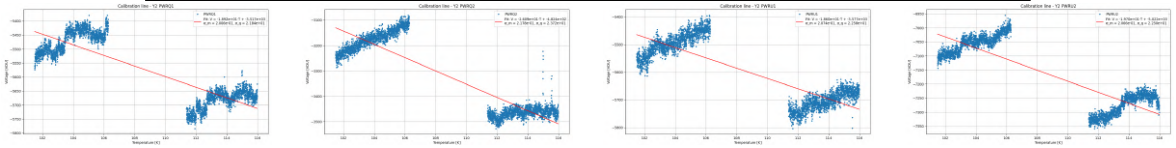

Board Y, Polarimeter Y3		
Offset file name	**Time range (UTC)**	**Offset [ADU]**
`2025_10_10_10-44-12.h5` [file 1]	10:55:00 - 11:00:00	**PWR Q1**= 220996.28
		PWR Q2= 226258.09
		PWR U1= 206908.71
		PWR U2= 227119.32
- [file 2]	-	**PWR Q1**= 221419.46
		PWR Q2= 226683.91
		PWR U1= 207332.28
		PWR U2= 227576.37
`2025_10_10_16-44-11.h5` [file 3]	17:08:00 - 17:13:00	**PWR Q1**= 221842.65
		PWR Q2= 227109.74
		PWR U1= 207755.85
		PWR U2= 228033.43

Table C.19: Table reporting the offset value considered for the detectors.

Board Y: Polarimeter Y3		
File ID	$\overline{\mathbf{T}}_{\mathbf{cal}}$ **[K]**	$\overline{\mathbf{V}}$ **[ADU]**
1	164.15	**PWR Q1**= −3473.51
		PWR Q2= −2974.30
		PWR U1= −3628.04
		PWR U2= −2392.63
2	168.55	**PWR Q1**= −3644.62
		PWR Q2= −3136.49
		PWR U1= −3843.23
		PWR U2= −2571.63
3	172.61	**PWR Q1**= −3846.88
		PWR Q2= −3376.43
		PWR U1= −4049.76
		PWR U2= −2782.01

Table C.20: Table reporting the average temperatures of the observed calibrator subsystem and the related average values of the voltage output of the detectors, for the different data files.

Board Y, Polarimeter Y3-Fit with 3 datasets		
Detector	α **[ADU/K]**	$\mathbf{T_n}$ **[K]**
PWR Q1	-42.2 ± 0.2	-81.8 ± 0.9
PWR Q2	-45.2 ± 0.2	-98.5 ± 1.0
PWR U1	-47.9 ± 0.2	-88.3 ± 0.8
PWR U2	-43.5 ± 0.3	-109.1 ± 1.2

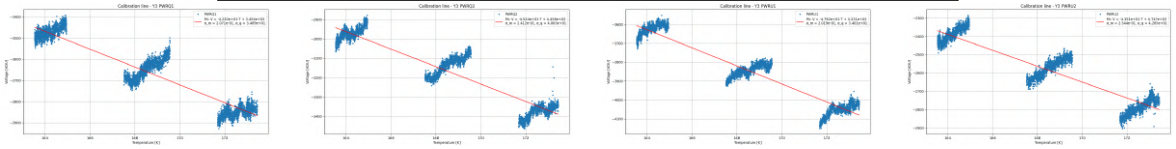

Board Y, Polarimeter Y3-Fit with 1 dataset: file 1		
Detector	α **[ADU/K]**	$\mathbf{T_n}$ **[K]**
PWR Q1	45.9 ± 1.2	-239.7 ± 7.1
PWR Q2	59.8 ± 1.2	-213.9 ± 5.3
PWR U1	56.8 ± 1.1	-227.9 ± 5.5
PWR U2	82.4 ± 1.1	-193.2 ± 3.3

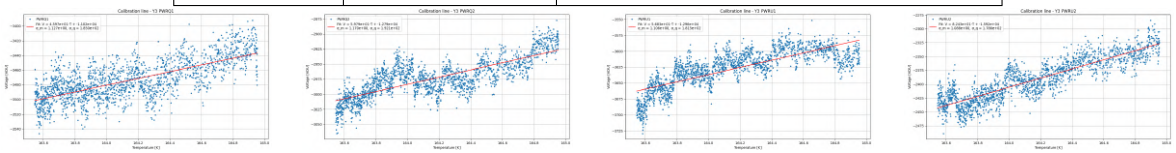

Board Y, Polarimeter Y3-Fit with 1 dataset: file 2		
Detector	**α [ADU/K]**	**T_n [K]**
PWR Q1	70.5 ± 0.9	-220.3 ± 3.5
PWR Q2	72.8 ± 0.8	-211.6 ± 2.9
PWR U1	41.3 ± 0.7	-261.6 ± 5.5
PWR U2	76.4 ± 0.8	-202.2 ± 2.8

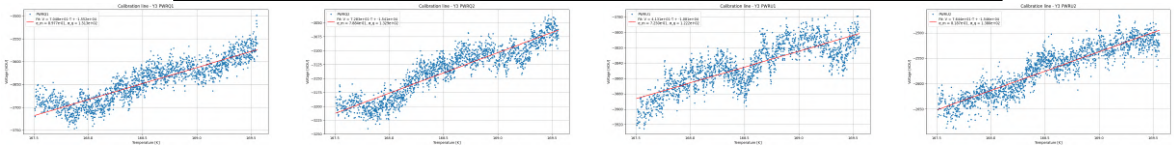

Board Y, Polarimeter Y3-Fit with 1 dataset: file 3		
Detector	**α [ADU/K]**	**T_n [K]**
PWR Q1	26.2 ± 1.1	-319.4 ± 14.6
PWR Q2	47.1 ± 1.0	-244.4 ± 6.5
PWR U1	49.8 ± 0.9	-253.9 ± 5.9
PWR U2	76.6 ± 1.0	-208.9 ± 3.6

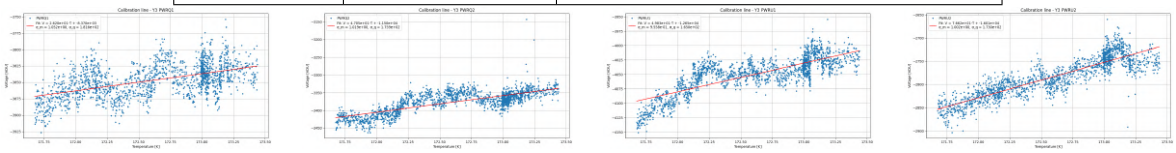

Board Y, Polarimeter Y3-Fit with 2 datasets: files 1,2		
Detector	**α [ADU/K]**	**T_n [K]**
PWR Q1	-34.1 ± 0.4	-61.9 ± 2.1
PWR Q2	-31.8 ± 0.4	-70.3 ± 2.3
PWR U1	-44.3 ± 0.4	-62.1 ± 1.6
PWR U2	-34.9 ± 0.5	-95.4 ± 2.5

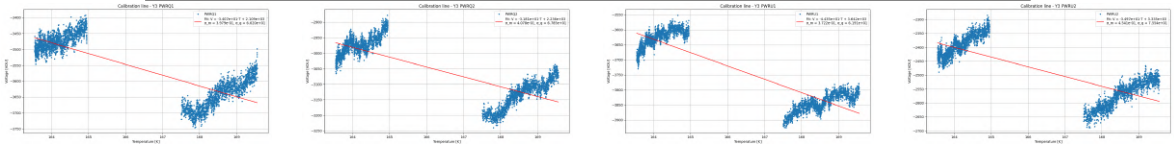

Board Y, Polarimeter Y3-Fit with 2 datasets: files 2,3		
Detector	α **[ADU/K]**	$\mathbf{T_n}$ **[K]**
PWR Q1	-43.4 ± 0.5	-84.3 ± 2.0
PWR Q2	-51.5 ± 0.5	-107.3 ± 2.1
PWR U1	-44.8 ± 0.4	-82.5 ± 1.8
PWR U2	-43.7 ± 0.6	-109.4 ± 2.6

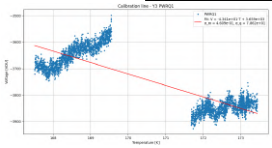
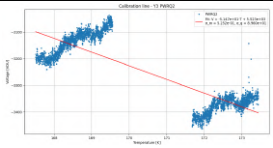
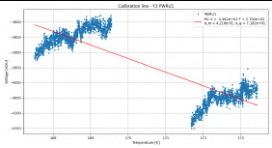
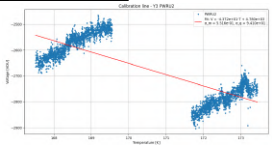

Bibliography

[1] The LSPE collaboration et al. 'The large scale polarization explorer (LSPE) for CMB measurements: performance forecast'. In: *Journal of Cosmology and Astroparticle Physics* 2021.08 (2021), p. 008. DOI: 10.1088/1475-7516/2021/08/008.

[2] Victor S. Alpher. *Ralph A. Alpher, George Antonovich Gamow, and the Prediction of the Cosmic Microwave Background Radiation*. arXiv:1411.0172 [physics.hist-ph]. Nov. 2014. DOI: 10.48550/arXiv.1411.0172. arXiv: 1411.0172 [physics.hist-ph].

[3] Daniel Baumann. *TASI Lectures on Inflation*. arXiv preprint arXiv:0907.5424. Available at https://arxiv.org/abs/0907.5424. 2009. arXiv: 0907.5424 [hep-th].

[4] Herbert B. Callen. *Thermodynamics and an Introduction to Thermostatistics*. 2nd ed. Wiley, 1985. ISBN: 978-0471862567.

[5] Peter Coles and Francesco Lucchin. *Cosmology: The Origin and Evolution of Cosmic Structure*. 2nd. ISBN: 978-0-471-48909-3. Chichester, UK: John Wiley & Sons, 2002.

[6] Robert E. Collin. *Foundations for Microwave Engineering*. 2nd. IEEE Press, 2001.

[7] James J. Condon and Scott M. Ransom. *Essential Radio Astronomy*. Princeton, NJ: Princeton University Press, 2016. URL: https://press.princeton.edu/books/hardcover/9780691151687/essential-radio-astronomy.

[8] F. Cuttaia et al. 'Planck-LFI radiometers tuning'. In: *Journal of Instrumentation* 4.12 (2009), T12013. DOI: 10.1088/1748-0221/4/12/T12013.

[9] Clive Dickinson. 'CMB foregrounds: a brief review'. English. In: *Proceedings of the 51st Rencontres de Moriond, Cosmology Session*. ARISF, 2016, pp. 53–62. ISBN: 979-10-968-7901-4.

[10] Bruce T. Draine. *Physics of the Interstellar and Intergalactic Medium*. Princeton, NJ: Princeton University Press, 2011. ISBN: 9780691122144.

[11] Engineering Toolbox. *Emissivity Coefficients of Common Materials*. 2024.

[12] *ESATAN-TMS Thermal Engineering Manual*. ITP Engines UK Ltd. Whetstone, Leicester, UK, 2010.

[13] W. L. Freedman et al. 'The Carnegie-Chicago Hubble Program. VIII. An Independent Determination of the Hubble Constant Based on the Tip of the Red Giant Branch'. In: *The Astrophysical Journal* 882.1 (Aug. 2019), p. 34. DOI: 10.3847/1538-4357/ab2f73.

[14] R.T. Génova-Santos et al. 'The LSPE/Strip instrument description and testing: LSPE-STRIP on-sky calibration strategy using bright celestial sources'. In: *arXiv preprint* (2024). arXiv: 2401.03802 [astro-ph.CO]. URL: https://arxiv.org/abs/2401.03802.

[15] Federico Incardona. 'Observing the Polarized Cosmic Microwave Background from the Earth: Scanning Strategy and Polarimeters Test for the LSPE/STRIP Instrument'. English. PhD thesis. Università degli Studi di Milano, 2020. DOI: 10.13130/INCARDONA-FEDERICO_PHD2020-01-17. URL: http://air.unimi.it/handle/2434/701276.

[16] Frank P. Incropera et al. *Fundamentals of Heat and Mass Transfer*. 7th. Hoboken, NJ: John Wiley & Sons, 2011.

[17] Koji Ishidoshiro et al. 'Readout system with on-board demodulation for CMB polarization experiments using coherent polarimeter arrays'. In: *IEEE Transactions on Nuclear Science* 59.3 (2012), pp. 647–655. DOI: 10.1109/TNS.2012.2195029. arXiv: 1112.0644 [astro-ph.IM]. URL: https://doi.org/10.48550/arXiv.1112.0644.

[18] National Institute of Standards and Technology. *Cryogenic Material Properties – Teflon*. 2025. URL: https://trc.nist.gov/cryogenics/materials/Teflon/Teflon_rev.htm.

[19] P. J. E. Peebles. 'Recombination of the Primeval Plasma'. In: *The Astrophysical Journal* 153 (July 1968), p. 1. DOI: 10.1086/149628.

[20] A. A. Penzias and R. W. Wilson. 'A Measurement of Excess Antenna Temperature at 4080 Mc/s.' In: *The Astrophysical Journal* 142 (July 1965), pp. 419–421. DOI: 10.1086/148307.

[21] Donald R. Pitts and Leighton E. Sissom. *Schaum's Outline of Theory and Problems of Heat Transfer*. 2nd ed. Schaum's Outlines. Reprint: 2011, ISBN: 978-0-07-176429-2. McGraw-Hill, 1998. ISBN: 978-0-07-050207-9.

[22] Planck Collaboration. 'Planck 2015 results. I. Overview of products and scientific results'. In: *Astronomy & Astrophysics* 594 (2016), A1. DOI: 10.1051/0004-6361/201527101.

[23] Planck Collaboration et al. 'Planck 2015 results. I. Overview of products and scientific results'. In: *arXiv e-prints* (2015). arXiv: 1502.01588 [astro-ph.CO].

[24] Arne Schröder et al. 'Brightness Temperature Computation of Microwave Calibration Targets'. In: *IEEE Transactions on Geoscience and Remote Sensing* 55.12 (Dec. 2017). DOI: 10.1109/TGRS.2017.2720160.

[25] Robert Siegel and John R. Howell. *Thermal Radiation Heat Transfer*. 4th. New York: Taylor & Francis, 2002.

[26] G. F. et al. Smoot. 'Structure in the COBE Differential Microwave Radiometer First-Year Maps'. In: *The Astrophysical Journal Letters* 396 (Sept. 1992), pp. L1–L5. DOI: 10.1086/186504.

[27] D. A. Varshalovich, A. N. Moskalev, and V. K. Khersonskii. *Quantum Theory of Angular Momentum*. World Scientific, 1988. DOI: 10.1142/0270.

[28] Robert M. Wald. *General Relativity*. ISBN: 978-0-226-87033-5. Chicago, IL: University of Chicago Press, 1984.

[29] Matias Zaldarriaga. 'Fluctuations in the Cosmic Microwave Background'. Ph.D. thesis. Massachusetts Institute of Technology, May 1998.